

1989

A search for the rare decay kaon(L) going to muon/electron

John Fred Ginkel
College of William & Mary - Arts & Sciences

Follow this and additional works at: <https://scholarworks.wm.edu/etd>



Part of the [Physics Commons](#)

Recommended Citation

Ginkel, John Fred, "A search for the rare decay kaon(L) going to muon/electron" (1989). *Dissertations, Theses, and Masters Projects*. William & Mary. Paper 1539623782.
<https://dx.doi.org/doi:10.21220/s2-tzke-ej63>

This Dissertation is brought to you for free and open access by the Theses, Dissertations, & Master Projects at W&M ScholarWorks. It has been accepted for inclusion in Dissertations, Theses, and Masters Projects by an authorized administrator of W&M ScholarWorks. For more information, please contact scholarworks@wm.edu.

INFORMATION TO USERS

The most advanced technology has been used to photograph and reproduce this manuscript from the microfilm master. UMI films the text directly from the original or copy submitted. Thus, some thesis and dissertation copies are in typewriter face, while others may be from any type of computer printer.

The quality of this reproduction is dependent upon the quality of the copy submitted. Broken or indistinct print, colored or poor quality illustrations and photographs, print bleedthrough, substandard margins, and improper alignment can adversely affect reproduction.

In the unlikely event that the author did not send UMI a complete manuscript and there are missing pages, these will be noted. Also, if unauthorized copyright material had to be removed, a note will indicate the deletion.

Oversize materials (e.g., maps, drawings, charts) are reproduced by sectioning the original, beginning at the upper left-hand corner and continuing from left to right in equal sections with small overlaps. Each original is also photographed in one exposure and is included in reduced form at the back of the book. These are also available as one exposure on a standard 35mm slide or as a 17" x 23" black and white photographic print for an additional charge.

Photographs included in the original manuscript have been reproduced xerographically in this copy. Higher quality 6" x 9" black and white photographic prints are available for any photographs or illustrations appearing in this copy for an additional charge. Contact UMI directly to order.

U·M·I

University Microfilms International
A Bell & Howell Information Company
300 North Zeeb Road, Ann Arbor, MI 48106-1346 USA
313/761-4700 800/521-0600

Order Number 9008528

A search for the rare decay $K_L \rightarrow \mu e$

Ginkel, John Fred, Ph.D.

The College of William and Mary, 1989

U·M·I
300 N. Zeeb Rd.
Ann Arbor, MI 48106

A SEARCH FOR THE RARE DECAY $K_L \rightarrow \mu e$

A Dissertation

Presented to

The Faculty of the Department of Physics
The College of William and Mary in Virginia

In Partial Fulfillment

Of the Requirements for the Degree of
Doctor of Philosophy

by

John F. Ginkel

1989

APPROVAL SHEET

This dissertation is submitted in partial fulfillment of
the requirements for the degree of
Doctor of Philosophy

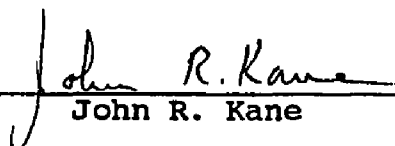


John F. Ginkel

Approved, August 1989



Morton Eckhauser



John R. Kane




Robert E. Welsh



Rolf G. Winter



Carl E. Carlson



Robert A. Orwoll
Department of Chemistry

A SEARCH FOR THE RARE DECAY $K_L \rightarrow \mu e$

John Fred Ginkel

August 1989

WMHEG-89-3

Supported in part by the
National Science Foundation

Grant PHY-8517485

TABLE OF CONTENTS

ACKNOWLEDGMENTS	v
LIST OF TABLES	vii
ABSTRACT	viii

<u>Chapter</u>		<u>Page</u>
I.	INTRODUCTION	1
	PURPOSE OF THE EXPERIMENT	1
	THE STANDARD MODEL	3
II.	THEORY	7
	INTRODUCTION	7
	MINIMAL EXTENSIONS OF THE STANDARD MODEL	9
	HORIZONTAL SYMMETRY	11
	TECHNICOLOR	14
	LEFT-RIGHT SYMMETRY	18
	COMPOSITENESS	20
	SUPERSYMMETRY	23
III.	EXPERIMENTAL METHOD	25
	INTRODUCTION	25
	MONTE-CARLO STUDIES	28
	K_L BACKGROUNDS	32
	BEAM LINE	36
	SPECTROMETER AND TRIGGER COUNTERS	40
	ANALYZING MAGNETS	40
	DRIFT CHAMBERS	42
	TRIGGER COUNTERS	44
	ELECTRON IDENTIFICATION	46
	CERENKOV COUNTER	46
	LEAD GLASS	48
	MUON IDENTIFICATION	50
	MUON HODOSCOPE	50
	MUON RANGEFINDER	51
	DATA ACQUISITION	54
	FRONT END ELECTRONICS	55
	READOUT SUPERVISOR AND CRATE SCANNERS	56
	3081/E PROCESSORS	58
	ONLINE ACQUISITION SYSTEM	59
	TRIGGERING	61
	LEVEL 1 TRIGGER	61
	LEVEL 3 TRIGGER	64

IV.	DATA ANALYSIS	67
	INTRODUCTION	67
	PATTERN RECOGNITION	68
	TRACK FITTING	72
	PRODUCTION ANALYSIS	75
	PARTICLE IDENTIFICATION	78
	TRACK QUALITY REQUIREMENTS	85
	CORRECTIONS REQUIRED	88
V.	CONCLUSION	
	FINAL SENSITIVITY	92
	FUTURE	95
APPENDIX A	PERFORMANCE OF THE MUON RANGEFINDER	96
REFERENCES		100
FIGURE CAPTIONS		103
FIGURES		106

ACKNOWLEDGMENTS

I would like to thank my collaborators on BNL experiment E791: K. Arisaka, L.B. Auerbach, S. Axelrod, K.A. Biery, G. Bonneaud, P. Buchholz, M.D. Chapman, R.D. Cousins, G. Daniel, M. Eckhause, J.S. Frank, P.P. Guss, G.W. Hart, V.L. Highland, M. Ierano, G.M. Irwin, D. Joyce, J.R. Kane, C.J. Kenney, W.W. Kinnison, P. Knibbe, J. Konigsberg, J. Kubic, K. Lang, D.M. Lee, J. Margulies, C.J. Martoff, C. Mathiazhagan, W.K. McFarlane, P. Melese, E.C. Milner, W.R. Molzon, D.A. Ouimette, J.L. Ritchie, P. Rubin, G.H. Sanders, M.B. Sivertz, W.E. Slater, Q.H. Trang, J. Urheim, W.F. Vulcan, D. Wagner, W.D. Wales, R.E. Welsh, R.J. Whyley, R.G. Winter, S.G. Wojcicki, and H.J. Ziock. I also thank the staff of the Brookhaven National Laboratory AGS department.

I would like to thank the many people at the College of William and Mary who have made this work possible:

Dr. Morton Eckhause, my advisor, for his guidance and encouragement during the last six years.

Dr. John R. Kane, Dr. Robert E. Welsh and Dr. Rolf G. Winter for their helpful comments and support during the experiment, and for reading the manuscript.

Dr. Robert J. Whyley for his invaluable assistance with the computer analysis performed.

Fellow graduate students Chris Kenney and Michael Chapman for all of their help during the experimental runs and the data analysis.

Mr. William Vulcan for his help during the experimental runs and his useful advice and support.

Dr. Carl E. Carlson and Dr. Robert A. Orwoll for reading the manuscript.

Dr. Paul P. Guss, Dr. Donald Joyce, Dr. Dayle Hancock and Dr. Yunan Kuang for their help during the experimental runs.

Ms. Dianne Fannin, Ms. Paula Spratley, and Ms. Sylvia Stout for all of their help.

I would also like to thank Ms. Tamera Mams for her help with the drawings in this manuscript, and for her valuable advice and support.

Finally I would like to thank my family for all of their encouragement and moral support during the last six years.

This work is supported in part by the National Science Foundation.

LIST OF TABLES

<u>Table</u>		<u>Page</u>
III.1	Dimensions (in meters) of Spectrometer Elements	26
III.2	Level 1 Trigger Requirements	63
III.3	Level 1 Trigger Rates (for 10^{13} protons per pulse)	64
IV.1	Efficiency of Track χ^2 Cuts	87
IV.2	Thickness of Detector Elements	90
A.1	Efficiencies for Rangefinder Modules in %	98
A.2	Muon Identification Efficiency of Rangefinder in %	99

ABSTRACT

A sensitive search has been carried out for the rare decay $K_L \rightarrow \mu e$. This decay violates conservation of separate lepton-number and thus is forbidden in the Standard Model of electro-weak interactions. Many new models have been proposed which could permit this process.

The data were collected in the B5 beamline of the Alternating Gradient Synchrotron facility at the Brookhaven National Laboratory during the Spring, 1988 slow-extracted beam running period. The experiment was sensitive to approximately fifty million $K_L \rightarrow \pi\pi$ decays. No $K_L \rightarrow \mu e$ candidate events were detected. The 90% confidence level upper limit for the branching ratio is $B(K_L \rightarrow \mu e) < 2.2 \times 10^{-10}$. This limit places a constraint on the mass of exotic particles proposed in many new theories.

A SEARCH FOR THE RARE DECAY $K_L \rightarrow \mu e$

Chapter I

Introduction

I.1 Purpose of the Experiment

New discoveries in particle physics have required larger accelerators in order to probe higher mass ranges. An alternative to this approach is to carry out a sensitive search for a process which is considered to be rare or forbidden. For example, in the Standard Model separate lepton number (or lepton flavor) is always conserved. Thus any observation of the decay $K_L \rightarrow \mu e$, which violates lepton flavor, would indicate new physics beyond the Standard Model.

Given the lack of any direct experimental evidence, the result of any new theory would be likely to manifest itself at a much higher energy than is currently accessible. Thus a search for a process like $K_L \rightarrow \mu e$ which, as will be shown later, is sensitive to mass scales in the tens to hundreds of TeV, can provide guidance in constructing new theories.

Until 1971 the experimental upper limit¹ for $B(K_L \rightarrow \mu e)$ was 6×10^{-6} (90% C.L.). Clark *et al.* measured² an upper limit of 1.57×10^{-9} ; however they also reported

$B(K_L \rightarrow \mu\mu) < 1.82 \times 10^{-9}$ (90% C.L.) which has since been observed at a rate four to five times higher; thus the Clark experiment's limit for $B(K_L \rightarrow \mu e)$ is certainly no lower than the rate for $K_L \rightarrow \mu\mu$.

Preliminary data for the experiment on which this paper is based were taken during 1987 (while construction of the experiment was continuing) and a limit $B(K_L \rightarrow \mu e) < 1.1 \times 10^{-8}$ (90% C.L.) has been reported³. Two other groups have recently been involved in a search for $K_L \rightarrow \mu e$. Brookhaven experiment E780 has reported⁴ a limit of 6.7×10^{-9} based on the 1987 running period, while their limit⁵ based on the combined data from 1987 and 1988 is 1.9×10^{-9} . In addition, KEK experiment E137 has reported⁶ a preliminary limit of 7.3×10^{-10} .

I.2 The Standard Model

The Standard Model is compatible with all known experimental results. It assumes that fundamental fermions, quarks and leptons, are organized in doublets to form three generations or families. Three interactions are accounted for in the Standard Model, which are mediated by exchanges of gauge bosons. The strong nuclear force is mediated by gluons in the range $\approx 1/m_\pi \approx 1/140$ MeV with a coupling strength ≈ 1 . The strong nuclear force is described by Quantum Chromodynamics (QCD) in which quarks interact by exchange of color charge; QCD is non-abelian, so that the field quanta (gluons) also have color charge and thus can interact directly. The quarks bind to form two kinds of color-singlet particles: baryons, which contain three quarks of different colors, and mesons which contain only quark-antiquark pairs. QCD is described by the $SU(3)_C$ gauge group with quarks represented by color triplets.

In the electromagnetic force, photons are exchanged over an infinite range with a coupling strength $\approx 10^{-2}$. In the weak nuclear force, W and Z bosons are exchanged in the range $\approx 1/m_W \approx 1/80$ GeV with coupling strength $\approx 10^{-6}$. Glashow, Weinberg, and Salam⁷⁻⁹ provided a model which unified the weak and electromagnetic interaction in the

$SU(2)_L \times U(1)_Y$ gauge group, and which operates on the "flavor" of quarks and leptons.

The symmetry group $U(1)_Y$ is the generator of the hypercharge, which is broken down to $U(1)_{em}$ by introducing a new scalar field. Adding a scalar potential to the electro-weak Lagrangian maintains its gauge invariance while the scalar potential ground state (or vacuum expectation value) spontaneously breaks the $SU(2)_L \times U(1)_Y$ symmetry. In addition, by choosing the appropriate vacuum expectation value for the scalar potential, the gauge bosons of the electro-weak theory, which are all massless in the unbroken $SU(2)_L \times U(1)_Y$ gauge, will acquire their correct masses. In the Standard Model, a scalar doublet field is assumed, which leads to four scalar particles. Three of the particles are "eaten" by the weak gauge bosons in order that they acquire their mass, leaving one physical scalar particle, the Higgs. The scale of symmetry breaking is given by the vacuum expectation value (≈ 250 GeV) of the Higgs.

The kaon is made up of a d and s quark: $K^0 = d\bar{s}$ and $\bar{K}^0 = \bar{d}s$. The neutral kaons can be combined to form CP eigenstates $|K_1\rangle$ and $|K_2\rangle$ which are CP even and CP odd respectively. The physically observed states are characterized by their decay modes: $K_S \rightarrow 2\pi$ with a relatively short lifetime (0.9×10^{-10} sec) and $K_L \rightarrow 3\pi$ with a longer lifetime (0.5×10^{-7} sec), where the 2π

final state is CP even and the 3π state is odd. The CP violating decay $K_L \rightarrow 2\pi$ has been observed¹ at the rate $B(K_L \rightarrow 2\pi) \approx 2 \times 10^{-3}$ which implies that the physical states are mixtures of the CP even and odd states.

The diagram responsible for $K^0 - \bar{K}^0$ mixing is shown in Fig 1. In the Standard Model, the small mass difference between K_L and K_S (3.5×10^{-12} MeV) results from the GIM mechanism in which the contributions to flavor-changing neutral interactions are suppressed by cancellations between diagrams with c and t quark transitions.

While the Standard Model is compatible with experimental results, it leaves a large number of questions unanswered. For example, CP violation arises from the quark mixing angles which are arbitrary parameters. And the scalar Higgs field, which leads to diagrams with quadratically diverging mass terms, requires that parameters be tuned to an unnatural precision. Furthermore, the physical Higgs particle has yet to be observed. And why are there so many particles and parameters in a "fundamental" theory? What is the origin of the fermion mass spectrum and why are the fermion masses so much less than the symmetry breaking scale (≈ 250 GeV)? Why do fermions appear to be organized in families? These questions have motivated a wide variety of new theories. Some consist of simple extensions to the

Standard Model while others introduce new fundamental particles and new gauge symmetries.

The details of specific models will be given in Chapter II, and the implications of $K_L \rightarrow \mu e$ and other flavor violating processes will be discussed. Chapter III describes the design considerations of the experiment and the details of the apparatus. The results of the 1988 data reduction and analysis are presented in Chapter IV and conclusions in Chapter V.

Chapter II

Theory

II.1 Introduction

While the Standard Model is compatible with experimental observations, it also includes many mysteries such as the large number of fundamental particles and arbitrary parameters, the apparent "family" structure, and the fermion mass spectrum. In order to answer these and other questions, a large number of extensions and replacements for the Standard Model have been proposed which include new fundamental particles and interactions, and many of these theories allow for lepton-flavor violation.

The contributions expected for different flavor-violating processes are extremely model dependent. For example, the decay $K^+ \rightarrow \pi^+ \mu e$ is similar to $K_L \rightarrow \mu e$ and in a naive comparison $K^+ \rightarrow \pi^+ \mu e$ appears less sensitive to high mass scales due to the shorter K^+ lifetime (a factor of four) and the reduced phase space of the three body final state (a factor of eight). However, in models without leptoquarks, $K^+ \rightarrow \pi^+ \mu e$ would be mediated by a vector interaction while $K_L \rightarrow \mu e$ would be an axial-vector

interaction. A comparison between these two processes in a horizontal symmetry model is given in section II.3.

The decay $\mu \rightarrow e\gamma$ (and other purely leptonic decays) is not allowed in models where lepton-flavor violation arises from leptoquarks. The upper limit on $B(\mu \rightarrow e\gamma)$ provides a stringent limit on theories with massive neutral leptons (see section II.2). The implications for horizontal theories are less significant due to the existence of (undetermined) mixing angles.

The decay $\mu \rightarrow 3e$ also has troublesome mixing angles, but can be used to constrain the mass splittings in horizontal models with degenerate masses (see section II.3). The upper limit for μ -e conversion on nuclei ($\mu N \rightarrow eN$) provides possibly the strongest mass limit on the proposed horizontal bosons.

The remainder of this chapter gives more details of these new theories and will concentrate on models which predict, or are constrained by, the process $K_L \rightarrow \mu e$.

II.2 Minimal Extensions

A simple extension of the Standard Model which allows for lepton-flavor violation is to assume that the lepton sector mixes analogously to the quark sector. In the Standard Model, lepton mixing is prohibited because the neutrinos are massless. Assuming a ν_τ mass of 200 MeV, the upper bound¹⁰ for $B(K_L \rightarrow \mu e)$ is $\approx 10^{-17}$.

However, the bound for lepton flavor violation could be significantly higher if there exists a new heavy neutral lepton, L_0 (see Fig 2). The upper limit¹¹ of $B(\mu \rightarrow e \gamma) < 4.9 \times 10^{-11}$ (90% C.L.) implies a lower mass limit¹² of approximately 10 GeV for a new neutral lepton. Thus, the rate for $B(K_L \rightarrow \mu e)$ could be in the range^{10,12} of 10^{-15} to 10^{-13} .

The Standard Model contains one Higgs doublet field which corresponds to a single physical neutral Higgs particle. However, the Higgs is difficult to observe: it is flavor-conserving and neutral, and its mass region is not known. Many new models and extensions to the Standard Model contain a more complex Higgs sector, and it is possible for these new Higgs particles to mediate observable processes. The Standard Model predicts, and experiment has confirmed, that the parameter ρ , defined as $M_W^2 / (M_Z^2 \cos^2 \theta_W)$, is approximately 1, which places a

constraint on theories with new Higgs fields.

The simplest extension is to assume two Higgs doublets, one of which is CP even and the other CP odd.^{13,14} (This model has the attractive feature of providing spontaneous violation of CP symmetry). Two Higgs doublets lead to five Higgs bosons, three of which are neutral and can couple to flavor-changing neutral currents. Based on the constraints from the K_L - K_S mass difference, the upper bound for $B(K_L \rightarrow \mu e)$ is in the range 10^{-10} to 10^{-13} .

II.3 Horizontal Symmetry

One unresolved mystery of the Standard Model is the observation of quark and lepton generations. To explain this phenomenon, a new "horizontal" gauge interaction has been proposed which connects the fermions from different generations. First, it is useful to categorize generation-changing processes in two ways (as first proposed by Cahn and Harari¹⁵): each quark and lepton doublet can be assigned a "Generation" number, G , from one to three. Hence, generation-changing processes can be described by their generation change, ΔG . In addition, processes are designated "diagonal" (if fermions of the same type are coupled, so that leptons couple to leptons and like-charge quarks couple together) or "non-diagonal". For example, $K^0-\bar{K}^0$ mixing (Fig. 3) is diagonal with $\Delta G=2$ while $K_L \rightarrow \mu e$ (Fig. 4) is non-diagonal, $\Delta G=0$. In the limit that generation mixing angles go to zero, only $\Delta G=0$ processes are allowed; for small mixing angles, $|\Delta G|=1$ processes are prohibited to first order and $|\Delta G|=2$ processes are prohibited to second order.

The Standard Model is extended to be $SU(2) \times U(1) \times SU(2)_H$ where $SU(2)_H$ is a new "horizontal" gauge group which contains three horizontal bosons. For specific models it is possible for the three masses to all be

different, or to be two or three-fold degenerate. For the case in which the masses are three-fold degenerate, there is no horizontal contribution to diagonal processes such as the $K^0-\bar{K}^0$ mixing and $\mu \rightarrow 3e$. If the masses are two-fold or non-degenerate, the rate of diagonal processes (which now receive a horizontal contribution) provides limits on the mass differences of the horizontal bosons. The upper limit¹⁶ of $B(\mu \rightarrow 3e) < 1 \times 10^{-12}$ constrains the mass splitting of the horizontal bosons to be¹⁵ $\Delta m < 85 \text{ TeV} |g_H/g|$ although this limit could be much smaller due to (undetermined) mixing angles.

The mass limit of the horizontal bosons imposed by $K_L \rightarrow \mu e$ can be estimated¹⁵ by comparing this rare process to the common decay $K^+ \rightarrow \mu^+ \nu$. Assuming that the generation mixing angle is approximately zero, the two processes are related by the ratio of their couplings and boson masses:

$$\frac{\Gamma(K_L \rightarrow \mu e)}{\Gamma(K^+ \rightarrow \mu^+ \nu)} = \frac{(g_H/2M_H)^2}{\sin^2 \theta_C (g^2/2M_W^2)^2} \quad (2.1)$$

or

$$M_H = 60 \text{ TeV} \frac{g_H}{g} \left[\frac{1 \times 10^{-10}}{B(K_L \rightarrow \mu e)} \right]^{1/4} \quad (2.2)$$

where M_H and g_H are respectively the horizontal boson mass and coupling constant.

By comparison, the upper limit¹⁷ of $B(K^+ \rightarrow \pi^+ \mu e) < 1 \times 10^{-9}$ (90% C.L.) constrains the boson mass to be $M_H > 26 \text{ TeV } |g_H/g|$. However, the most stringent limit may come from $\mu N \rightarrow e N$ in which the upper limit¹⁸ of 4.6×10^{-12} gives a mass constraint¹⁹ of $M_H > 220 \text{ TeV } |g_H/g|$.

II.4 Technicolor

If, as it is widely believed, the Standard Model is not the complete description of nature, it is likely that there exists a larger symmetry group, and that the observation of $SU(3) \times SU(2) \times U(1)$ is due to the spontaneous breakdown of the larger symmetry. The masses of observed particles are then the result of the characteristic scale at which the symmetry breakdown occurs. For example, in $SU(2) \times U(1)$ the symmetry breaking scale is given by the vacuum expectation value of the Higgs field (on the order of 250 GeV).

As described earlier, the fermion and boson masses in the Standard Model are generated by adding a scalar potential term to the Lagrangian. However, the scalar fields include diagrams with quadratic mass divergences which lead to an unnatural tuning of parameters. In Technicolor theories²⁰ this problem is resolved by assuming that scalars are not fundamental particles but rather are comprised of new massless fermions (techniquarks) bound by a new gauge interaction (technicolor) which is analogous to QCD and becomes strong at a scale of 1 TeV.

The techniquarks come in doublets which have $SU(2)_L \times SU(2)_R$ flavor symmetry. The spontaneous breaking of

chiral symmetry due to technicolor results in pseudoscalar bound states (technipions) analagous to pions in QCD theory. Some of these technipions are "eaten" by the intermediate vector bosons in order that they acquire their mass. Hence, technipions replace the Higgs particles of the Standard Model, and the vacuum expectation value of the scalar field is replaced by the technicolor analogue of the pion decay constant, F_π (which is still on the order of 250 GeV). The remaining technipions are referred to as pseudo-Goldstone bosons.

In order to provide masses for the fermions, another gauge group, extended technicolor (ETC), has been proposed.²¹ The ETC interaction becomes strong around 100 TeV. In a simple model of ETC, every lepton and like-charge quark has an associated technifermion with a family structure similar to that of the Standard Model. As the SU(3) ETC group breaks down to ordinary SU(2) TC, ETC bosons receive masses which are given to ordinary fermions.

ETC theories have several possible sources of flavor violation. The ETC bosons can mediate $K_L \rightarrow \mu e$ (as shown in Fig. 5). G_H is estimated²² to be

$$G_H \approx \frac{m_d}{\langle T \rangle} \approx \frac{1 - 10 \text{ MeV}}{10^8 \text{ GeV}^3} \quad (2.3)$$

where m_d is the d quark mass and $\langle T \rangle$ is the scale of the

TC condensates. Then

$$\frac{\Gamma(K_L \rightarrow \mu e)}{\Gamma(K^+ \rightarrow \mu \nu)} = \frac{G_H^2}{G_F^2 \sin^2 \theta} \quad (2.4)$$

or

$$B(K_L \rightarrow \mu e) \approx 6 \times (10^{-9} - 10^{-11}). \quad (2.5)$$

The pseudo-Goldstone bosons (PGB) which result from ETC theories include colored states (expected to be of order 300 GeV) as well as lower mass color singlet states. PGB interactions, particularly the light color singlets, can provide large contributions to flavor violating processes (Fig. 6 shows the diagram which could mediate $K_L \rightarrow \mu e$); hence various suppression mechanisms have been proposed. For example, it has been shown²³ that fermions of a given charge will receive their masses from a single techniquark-antitechniquark pair ("monophagy"). In addition there have been attempts to construct "GIM-like" mechanisms to suppress flavor-changing neutral currents in ETC theories.²⁴ The mass limit on pseudo-Goldstone bosons (without any new suppression mechanism) from $K_L \rightarrow \mu e$ is²⁵

$$M_B \approx 15 \text{ GeV} \left[\frac{1 \times 10^{-10}}{B(K_L \rightarrow \mu e)} \right]^{1/4} \quad (2.7)$$

In addition to neutral scalar particles, technicolor theory predicts the existence of colored (pseudo-scalar)

leptoquarks which change quarks directly into leptons (see Fig. 7). Because leptoquarks do not contribute to $K^0-\bar{K}^0$ mixing there is no suppression mechanism needed, and thus the contribution to kaon decays may be relatively large. The mass limit of leptoquarks from $K_L \rightarrow \mu e$ is estimated to be²⁶

$$M_p \approx 1.2 \text{ TeV} \left[\frac{1 \times 10^{-10}}{B(K_L \rightarrow \mu e)} \right]^{1/4} \quad (2.7)$$

II.5 Left-Right Symmetry

One of the many unanswered questions of the Standard Model is the origin of parity violations. In left-right symmetric models it is assumed that left and right helicities are symmetric and that the observed parity violations are the result of the right-handed gauge bosons (W_R) being much more massive than the left-handed bosons. Even the most simple left-right symmetric model, $SU(2)_L \times SU(2)_R \times U(1)$, has several appealing aspects. For example, the $U(1)$ generator, which does not represent a physical quantity in the Standard Model, is associated with the quantum number $B-L$ in left-right symmetric models.²⁷ In addition, CP violation arises from spontaneous symmetry breaking, and the amount of CP violation is given by the ratio of the left and right-handed gauge boson masses.²⁸

The diagram for $K_L \rightarrow \mu e$ via W_R in a left-right symmetric model is shown in Fig. 8. Assuming a W_R mass of 1 TeV (this bound comes from the K_L-K_S mass difference²⁹), $B(K_L \rightarrow \mu e)$ is estimated¹⁰ to be in the range $10^{-15} - 10^{-11}$. The W_R mass could be lower if there were cancellations between the gauge and Higgs contributions to the K_L-K_S mass difference, which would push up the rate for $K_L \rightarrow \mu e$.

In a slightly different model, the symmetry group $SU_L^W(2) \times SU_R^H(2) \times U(1)$ is proposed³⁰, in which $SU_R^H(2)$ represents a right-handed horizontal gauge group which mediates interactions between families. $SU_R^H(2)$ symmetry is broken at a large mass scale by a horizontal Higgs doublet which produces three right-handed horizontal gauge bosons with degenerate masses. The K_L-K_S mass difference provides a bound for the horizontal boson masses:

$$5 \text{ TeV} < M_H \frac{g_L}{g_R} < 66 \text{ TeV} \quad \text{which implies} \quad B(K_L \rightarrow \mu e) \quad \text{between} \\ 10^{-6} \text{ and } 10^{-10}.$$

Pati and Salam proposed a theory^{31,32} which unites quarks and leptons in the gauge group $SU_L(2) \times SU_R(2) \times SU_C(4)$. The $SU_C(4)$ group represents fermions with four possible colors: three colors which correspond to the usual quark color charge and lepton number as the fourth color. At some mass scale M_C , the $SU_L(2) \times SU_R(2) \times SU_C(4)$ group breaks down to $SU_L(2) \times SU_R(2) \times U_{B-L}(1) \times SU_C(3)$, and, finally, at the mass scale of W_R , the standard $SU_L(2) \times U_Y(1) \times SU_C(3)$ group appears. The $SU_C(4)$ group includes massive gauge bosons (which contain baryon and lepton number) which could mediate $K_L \rightarrow \mu e$ (see Fig. 9). The mass limit for the $SU_C(4)$ boson^{33,34} is in the range

$$M_B \approx 650 - 740 \text{ TeV} \left[\frac{1 \times 10^{-10}}{B(K_L \rightarrow \mu e)} \right]^{1/4} \quad (2.8)$$

II.6 Compositeness

In composite theories, quarks and leptons are assumed to be comprised of new fundamental fermions, called preons, bound by a new strong interaction similar to QCD. Composite theories are motivated by the large number of "fundamental" particles in the Standard Model. In addition, compositeness offers an explanation of the fermion mass spectrum and the observation of families. CP violation can arise from spontaneous symmetry breaking of the chiral symmetry of the ordinary fermions. The scale at which compositeness becomes strong, Λ_H , can be estimated by its contribution to $(g-2)$ of the muon:^{35,36}

$$(g-2)_{\text{exp}} - (g-2)_{\text{theor}} < 1.5 \times 10^{-8} \text{ which implies } (m_\mu/\Lambda_H)^2 < 10^{-8} \text{ or } \Lambda_H > 1 \text{ TeV.}$$

A minimal composite model³⁷ assumes two types of preons: those carrying only flavor (flavons) and those carrying only color (chromons). Preons are bound by a new strong force (with mass scale Λ_H) to form quarks and leptons, in which the quarks and leptons within a family are assumed to have the same flavons but different chromons. Flavon and chromon transitions, via the strong preonic force, can mediate $K_L \rightarrow \mu e$ (see Fig. 10). For this minimal model, in which the electron and muon family members are assumed to have the same inverse size, the

composite mass scale has been estimated to be³⁸

$$\Lambda_H > 470 \text{ TeV} \left[\frac{1 \times 10^{-10}}{B(K_L \rightarrow \mu e)} \right]^{1/4} \quad (2.9)$$

Using a similar model, Greenberg et al.³⁹ proposed possible scenarios in which the contributions to $K_L \rightarrow \mu e$ would be suppressed, thus reducing this limit.

Another composite model has been proposed^{40,41} which includes two new gauge forces. Four families are assumed: e , μ , τ , and a new fourth family τ' . Two new gauge forces are also assumed: "hypercolor" which becomes strong at a mass scale $\Lambda_H \approx 1 \text{ TeV}$, and a superheavy "metacolor" which becomes strong on the order of 10^{11} TeV . Preons are bound by the metacolor force to form "bare" electron and muon families, e^0 and μ^0 , as well as "hyperfermions" and "hyperbosons".

The hypercolor force binds the hyperfermions and hyperbosons to form the bare τ^0 and τ'^0 families (the τ^0 and τ'^0 families are replications of the e^0 and μ^0 families). The hypercolor force forms hyperfermion condensates (hyperfermion-antihyperfermion pairs) which break $SU(2)_L \times U(1)$ symmetry and generate the ordinary fermion masses. Mass mixing between the four families will thus allow for $K_L \rightarrow \mu e$. Comparing this to the common decay $K^+ \rightarrow \mu^+ \nu$ gives

$$\frac{\Gamma(K_L \rightarrow \mu e)}{\Gamma(K^+ \rightarrow \mu^+ \nu)} = \frac{1}{2} \left[\frac{g_{HC}^2 \sin^4 \alpha}{G_F \Lambda_0^2 \sin \theta_C} \right]^2 \left[\frac{m_K^2}{m_\mu (m_d + m_s)} \right]^2 \quad (2.10)$$

where g_{HC} is the hypercolor coupling (expected to be between 1 and 10) and Λ_0 is the mass of the hyperfermion condensates (expected to be 1-2 TeV). $\sin \alpha$ is the family mixing parameter which is constrained by known masses to be $0.04 < \sin \alpha < 0.10$. Hence, putting in the most conservative numbers gives a lower bound of $B(K_L \rightarrow \mu e) > 3 \times 10^{-11}$.

II.7 Supersymmetry

Supersymmetric theories (SUSY) propose that there is a new symmetry which relates fermions and bosons. SUSY theories are motivated by the fact that scalar fields produce quadratically diverging mass terms which require an unnatural tuning of parameters. Since fermions and bosons are related in SUSY models, there is a mechanism for cancelling these divergences. In addition, it is possible for SUSY models to explain mass scales, including gravity, without introducing a large number of new parameters.

In a SUSY extension of the Standard Model, a supersymmetric fermion (boson) partner exists for each known boson (fermion). In the Standard Model, neutral flavor-changing processes are suppressed by the GIM mechanism. The new super-partners proposed in SUSY suggest that there should be a new "super-GIM" mechanism operating in order that the theory match experimental observations. Thus, neutral flavor-changing interactions can be used to place limits on the mass splittings of the spin-zero super-partners (squarks and sleptons).

The main SUSY contribution to the K_L - K_S mass difference is from a box diagram in which SUSY-gauge bosons and squarks are exchanged. Assuming a SUSY-W boson

mass ≈ 100 GeV, the bound⁴² on the squark mass splitting is $\Delta m_{sq}^2 / m_{sq}^2 < O(10^{-3})$.

The decay $K_L \rightarrow \mu e$ can proceed via a box diagram (see Fig. 11) in which either SUSY-neutrinos or a squark and slepton are exchanged. In the case of SUSY-neutrino exchange, the rate $B(K_L \rightarrow \mu e)$ is estimated⁴³ to be two orders of magnitude lower than the Standard Model limit (for degenerate neutrino mass) of $B(K_L \rightarrow \mu e) < 10^{-17}$. In the case of squark and slepton exchange, there will be a second-order super-GIM cancellation (due to the squark and slepton exchange), hence $K_L \rightarrow \mu e$ does not provide a constraint on either Δm_{sq} or Δm_{sl} .

Superstring theories have become extremely popular because they could provide a unified theory which includes gravity. In particular, the E_6 gauge group of such models can be broken into a realistic low-energy gauge group.⁴⁴ Cambell et al.⁴⁵ have calculated the bounds on new Yukawa couplings expected in an E_6 model based on various flavor-changing neutral interactions. The decay $K_L \rightarrow \mu e$ can proceed via a new neutral SUSY-Higgs boson, but a tighter constraint on the mass and Yukawa coupling comes from the $K_L - K_S$ mass difference.

Chapter III

Experimental Method

III.1 Introduction

The experimental apparatus is located in the B5 line of the Brookhaven Alternating Gradient Synchrotron (see Fig. 12). The beamline was designed to allow up to 10^{13} protons on target per pulse; the beam pulses during the 1988 running period were approximately 1.4 seconds in length with a repetition rate of 3.2 seconds. The beam is focussed at the target position by two pairs of quadrupole magnets. A series of vertical pitching magnets allows the targetting angle to be varied. Charged particles are swept out of the beam by two dipole magnets, and a precise collimator system defines a $60 \mu\text{sr}$ neutral beam.

Two analyzing magnets allow a redundant momentum measurement which reduces backgrounds due to pion decay and mismeasurements. Ten modules of precision drift chambers are used for tracking (the drift chamber cell geometry is shown in Fig. 13). The upstream drift chambers and several planes of scintillator counters provide a fast low level trigger. Fast electron

identification is performed by a gas Cerenkov counter, and a lead glass calorimeter provides additional electron identification in the offline analysis. Helium bags are located between the drift chamber modules and inside both analyzing magnets in order to reduce the effects of multiple scattering. In addition, helium bags are located in the neutral beam between the Cerenkov counters and also in the middle of the muon rangefinder in order to reduce the effects of neutron interactions. Table III.1 gives the dimensions of the spectrometer elements.

Table III.1

Dimensions (in meters) of Spectrometer Elements

<u>Element</u>	<u>Z Pos</u>	<u>Inner X</u>	<u>Outer X</u>	<u>Half Y</u>
Vac Window	0.0	0.095		0.34
Drift Chm 1	17.9	0.095	0.465	0.345
Drift Chm 2	19.4	0.104	0.587	0.404
48D48	20.4	0.115	0.610	0.45
Drift Chm 3	22.4	0.120	0.968	0.505
96D40	23.5	0.130	1.220	0.559
Drift Chm 4	25.3	0.134	1.359	0.607
Drift Chm 5	26.8	0.142	1.519	0.709
Trig Cntr 1	27.0	0.143	1.343	0.90
Cerenkov	27.2	0.159	1.520	0.90
Trig Cntr 2	30.3	0.24	1.440	0.90
Pb Glass	30.5	0.168	1.520	0.90
Steel Filter	32.4			
Muon Hodo	33.3	0.24	2.100	1.31
Muon Range	34.4	0.24	2.490	1.50

A 91.0 cm steel wall located downstream of the lead glass serves as a hadron filter and is followed by a scintillator hodoscope (the muon hodoscope) which provides

a fast muon signal. A muon rangefinder, consisting of marble and aluminum degrader interspersed with proportional wire chambers, is also utilized in the offline analysis.

The high kaon flux requires a fast data acquisition system and multi-stage trigger (a block diagram of the online data acquisition system is shown in Fig. 14. and a schematic of the Level 1 trigger is shown in Fig. 15). A custom-designed highly parallel data readout system has been constructed, and a large online processor performs event reconstruction and selection.

III.2 Monte-Carlo Studies

A Monte-Carlo program was used to calculate the geometrical acceptance of the various kaon decay channels and to simulate detector responses in order to check the consistency of the data. The Monte-Carlo program has three stages: the generation of the kaon and daughter particles, swimming the daughter particles through the detector, and simulating detector hits based on the projected tracks. Following stage three the Monte-Carlo generated data are packed into a common block in a way identical to that of real data.

In the first stage of the Monte-Carlo, a kaon is generated and a decay branch is selected. An interaction point in the target is chosen and a second point ten meters downstream is chosen with a random X and Y position; these two points determine the kaon direction. The kaon momentum and lifetime are chosen by sampling the appropriate distributions (the kaon momentum distribution is determined by scaling the kaon production data^{46,47} from higher energy protons to the AGS proton energy of 24 GeV).

Next the kaon and all unstable daughter particles are allowed to decay. A decay branch is chosen among the possible decay branches with the relative weighting of

each having been set by the user. For two-body decays, the opening angles of one of the daughter particles is chosen randomly and the other parameters are fixed by four-momentum conservation. For three-body decays, the parameters are chosen by sampling the appropriate Dalitz plot. Unstable daughter particles decay with a lifetime taken from a random distribution about the mean lifetime.

A pre-cut is placed on all the tracks in order to save CPU time: it is required that all charged daughter particles project onto the first drift chamber module. The daughter particles are then Lorentz-boosted into the lab frame.

In stage two all particles are projected through the detector. The swimming routine does a straight-line projection of the tracks in regions of no magnetic field, and uses a fourth-order Runge-Kutta integration to project the tracks inside a region with magnetic field. The user can select one of three magnetic field calculations: a perfect magnetic field in which each magnet provides a 300 MeV/c kick for all track positions; a routine which actually integrates the equations of motion for an arbitrary track given its initial position, trajectory, momentum and step size, or a routine which has the magnetic field stored as an array so that the integrated field experienced by a particle is determined from a look-up table instead of a calculation.

The track projection is performed sequentially from one detector aperture to the next. At the beginning of each aperture the X and Y position and trajectory are modified to account for the multiple scattering which occurs between the two apertures. Within the aperture only the trajectory is changed due to the multiple scattering. The change in the track trajectory due to scattering is simulated by a Molière distribution scaled to the Gaussian width¹:

$$\sigma_{\text{ms}} = \frac{0.014}{p \text{ (Gev/c)}} \sqrt{N_L} \quad (3.1)$$

where N_L is the number of radiation lengths in the material and p is the track momentum. The X and Y positions, projected from the smeared trajectory onto the next aperture, are smeared using a Molière distribution scaled to the width $\sigma_{\text{ms}} / \sqrt{3}$. A cut is made to require the track to lie within the dimensions of each aperture.

For electrons the energy loss due to bremsstrahlung is calculated by sampling the probability distribution

$$P(x) = N_L x^{4/3} \quad (3.2)$$

where x is the fraction of energy loss.⁴⁸

In the third stage of the Monte-Carlo, track information is used to simulate detector responses. The wire inefficiencies of the drift chambers are simulated

and the distance of closest approach (DOCA) is smeared out by a Gaussian distribution. The hit time is calculated by summing the time of flight for a particle to reach the aperture plus the drift time corresponding to the corrected DOCA. The earliest time is selected and the hit time converted into TDC counts in 2.5 ns bins. Finally extra wire hits due to electronic noise are added. The noise due to accidental hits is simulated by allowing extra K_L decays which produce extra tracks.

The TDC information for the other detectors is simulated without corrections for inefficiencies, position errors or electronic noise. For the Cerenkov counter and lead glass array the ADC information is obtained by assuming that all charged particles are minimum ionizing so that the number of ADC counts is a function only of the track length in the counter.

III.3 Background from Kaon Decay

The largest source of background to the $K_L \rightarrow \mu e$ signal comes from $K_L \rightarrow \pi e \nu$ decay (designated K_{e3}) in which the pion decays or is misidentified as a muon. The branching ratio of K_{e3} is 0.387 and the probability that the pion will decay upstream of the muon filter is 0.10, so that approximately 4% of the K_L decays will produce an electron and a muon plus neutrinos. The worst background comes from the corner of the Dalitz plot where the sum of the energies of the pion and electron is a maximum and the energy of the neutrino is near zero; the density of the Dalitz plot goes quickly to zero in this region.

The K_{e3} decays can be divided into three categories: those in which the pion decays before the first drift chamber or after the last drift chamber, those in which the pion decays between the first and last drift chamber, and those in which the pion does not decay but is misidentified as a muon. Monte-Carlo studies were done to check the background level for K_{e3} decays and to investigate which kinematic and track quality cuts would be useful in suppressing backgrounds. The most important cuts for suppressing K_{e3} backgrounds are the invariant mass calculation of the K_L and the collinearity of the reconstructed kaon direction with respect to the momentum

sum direction of the observed daughter particles (which suppress three body decays for which the neutrino carries off some of the transverse momentum). Events in which the pion decays in the spectrometer can be identified by a kink in the Y view of the track.

The invariant mass calculation is the most powerful cut for suppressing K_{e3} decays. The kinematic limit of the invariant mass, assuming a muon and electron in the final state, can be expressed in terms of the πe invariant mass, $M_{\pi e}^2$:

$$M_{\mu e}^2 = M_{\pi e}^2 - m_{\pi}^2 + m_{\mu}^2 - 2P_e \cdot (P_{\pi} - P_{\mu}) \quad (3.3)$$

where P represents the respective 4-momenta. If there are no errors in the measurement of the 3-momenta and the muon is the result of pion decay, $M_{\mu e}$ is a maximum when $M_{\pi e}$ is its maximal value of m_K and the last term is zero:

$$M_{\mu e}^2 = m_K^2 - m_{\pi}^2 + m_{\mu}^2 \quad (3.4)$$

or

$$M_{\mu e} = m_K - 8.4 \text{ MeV}. \quad (3.5)$$

This corresponds to a mismeasurement of the mass by more than four standard deviations. However, if the pion does not decay but is misidentified as a muon, the last term is not Lorentz-invariant but depends on the angle, θ , between the kaon direction in the lab frame and the pion direction in the kaon rest frame. The mass limit for this

case approaches 8.4 MeV as the angle θ goes to zero (that is, the pion is as forward as possible). Hence, this background can be suppressed by cutting on the momentum balance of the two tracks. (However, this cut was not implemented in the final analysis). The track kinematics are shown in Fig. 16-18. If there are errors in the 3-momenta due to pion decays in the spectrometer, the value of $M_{\pi e}$ could be greater than m_K so that the 8.4 MeV bound would not hold. However, this type of background event should be suppressed by track quality cuts.

Another potential source of background is due to the double misidentification of the charged daughter particles from K_{e3} events. If the electron and muon from K_{e3} decay are misidentified as a muon and electron respectively, there is no kinematic upper bound on the reconstructed μe mass. This background is most serious when the pion is as forward as the acceptance allows. Hence, it also can be suppressed by cutting on the momentum balance of the two tracks.

$K_{\mu 3}$ events can enter as a background if the pion is misidentified as an electron. However the kinematic upper bound of the reconstructed μe mass is 21 MeV below the kaon mass. Hence, for this to enter as a possible background event would require a large error in the momentum measurement which can be suppressed by track quality cuts.

Finally it is possible for two K_L decays to overlap such that an electron from one decay and a muon from another decay satisfy the mass and collinearity requirements. Such accidental backgrounds can be minimized by means of tight timing requirements in the Level 1 trigger.

III.4 Beamline

The beamline was designed in order to maximize K_L production and geometric acceptance while minimizing background. The production target is supported on a table which permits the targetting angle to be varied between 0 and 4.5° . The neutron flux falls more rapidly than the K_L flux with increasing production angle. Thus the ratio of neutrons to kaons can be minimized. By placing the target upstream of the focal point of the collimator system, no particle should strike the face of the collimator, and thus this source of background is reduced. However, moving the target upstream also reduces acceptance; thus the target table was designed to be adjustable in the Z direction so the background rate and acceptance could be optimized.

The choice of target material is influenced by considerations of kaon production and length. A light target produces a higher kaon flux per incident proton but requires a longer target. The offline analysis requires good resolution of the projected kaon vertex to the target. Increasing the production angle increases the apparent transverse size of the target and thus degrades the resolution of the kaon direction. Extensive beam studies were carried out during test runs in 1986 and 1987

in which many targetting parameters were studied, including target material, target size, Z position, and production angle. For the 1988 run, a 0.3 x 0.3 x 19.0 cm³ copper target was utilized with a targetting angle of 2.75°.

Following the target there are two sweeping magnets which dump the charged beam and a high-precision collimator system which defines a neutral beam of 4.1 mrad (horizontally) by 15.0 mrad (vertically). For a targetting angle of 2.75° the proton beam strikes the beam dump approximately 3 meters downstream of the target and 20 cm below the entrance of the neutral beam. A brass collimator begins inside the first sweeping magnet, 106 cm downstream of the front pole face. A lead converter is located inside the magnet upstream of the collimator to remove photons from the beam; it consists of 17 foils, each 0.224 cm thick and spaced 5 cm apart. A thin foil was chosen so that the electron-positron pairs do not re-radiate new photons while the 5 cm spacing allows the electrons and positrons to be swept away from the beam line. There is a vacuum window located in the second collimator, with the vacuum maintained through the decay region. The third collimator element, located inside the second sweeping magnet, is connected by a bellows to the second collimator upstream and the decay region downstream.

All of the collimator elements downstream of the first sweeping magnet are mounted on a steel platform so that individual elements can be taken out and reinserted in a reproducible way. The platform assembly is supported by three jacks which can be accessed remotely in order to adjust the alignment of the entire collimator system.

Neutron backgrounds pose a serious threat to the experiment; neutron sources include high energy neutrons from the neutral beam halo and low energy neutrons from the proton dump which leak into the collimator system or penetrate through the main shielding. Several steps were taken in order to moderate and absorb neutrons between the proton dump and the decay region. The nominal length of the proton steel dump is six meters; however there is some space between the collimator elements and the steel as well as large gaps in the steel to accommodate the support structures. Hence lead bricks were used to fill as much of this space as possible. Borated concrete blocks approximately 60 cm thick were placed in the transition region between the downstream end of the second sweeping magnet and the start of the decay region. Finally, polyethelene bricks and containers of a Boraxo-water slurry were stacked around the beamline in the transition region.

The decay region is an 8.3-meter long tapered pipe which, according to a Monte-Carlo calculation, allows 3.1%

of the produced kaons to decay. Lengthening the decay region increases the number of kaons which will decay but reduces the acceptance of the experiment. The downstream end of the decay region has three Mylar windows, each 0.0508 cm thick: one on either side of the neutral beam which are $68.6 \times 35.1 \text{ cm}^2$ and the neutral beam window which is $45.7 \times 13.7 \text{ cm}^2$.

III.5 Spectrometer and Trigger Counters

The spectrometer consists of drift chambers placed in between two large-aperture analyzing magnets with opposite polarity, each of which provides a transverse momentum kick of 0.30 GeV/c and $\int B \cdot dl$ of 10.0 kg·m so that the original track angle is restored after the second magnet. The use of two analyzing magnets allows two separate momentum measurements which helps to suppress backgrounds due to pions which decay in the spectrometer. The drift chambers, together with the trigger scintillators located farther downstream, provide the fast signal for the Level 1 trigger.

III.5.1 Analyzing Magnets

The first magnet, a 48D48, has a gap which measures 48 inches in the Z direction (along the beamline) by 48 inches in X by 37 inches in Y. It requires approximately 2000 A in order to maintain a field of 6.3 kG at the center of the magnet (Z = 21 m). The gap of the second magnet, a 96D40, measures 40 inches in Z by 96 inches in X by 44 inches in Y. The 96D40 requires 2500 A to maintain a field of 6.4 kG at the center of the magnet (Z = 24 m). The 96D40 also has a set of booster coils which

improves the field homogeneity by reducing the air space between the coils, and which also reduces the operating cost of the magnet since less total current is required. Both magnets have iron mirror plates on the upstream and downstream ends in order to diminish the field strength in regions outside of the magnets. The dimensions of the mirror plates were chosen to accommodate the maximum magnetic flux without reducing the geometrical acceptance of the spectrometer.

The total momentum resolution of the spectrometer is dependent on the uncertainties in multiple scattering, in the intrinsic drift chamber resolution, and in the magnetic field. Thus the optimal momentum resolution requires a carefully measured magnetic field map. BNL provided the magnet mapping apparatus. Two Hall probes were positioned in a non-magnetic cart in order to measure B_x and B_y . The cart rested in an aluminum channel along the Z (beam) direction and was moved by means of a plastic chain driven by a stepping motor. The channel was supported by an aluminum frame, mounted inside the magnet, which could be adjusted (by hand) in the X and Y direction in two inch steps. An IBM PC was used to request the appropriate Z position, typically in two inch steps, and also to read out the digital Teslameter values for both Hall probes at each Z position. In addition, meters for the pitch about the Z axis and the roll with respect to

the Z axis were read out. During the magnet mapping, and also during the physics data taking, a reference Hall probe, located on the bottom pole face of each magnet, was monitored. The data were written by the IBM PC to floppy disk and transferred to the BNL IBM 3090 for further analysis.

In a perfect magnet, the B_x component should be zero; in the 96D40, B_x was typically 1% of B_y while in the 48D48 B_x could be as large as 10% of B_y . The measured B_x field is extremely sensitive to the roll about the Z axis; however the roll meter was found to be unreliable. Hence a Poisson type of simulation was used to obtain the B_x component as well as B_z (which was not measured), and to obtain B_y in regions which could not be measured by the mapping apparatus. The two-dimensional Poisson calculation determines B_x and B_y in the x-y plane, and B_z and B_y in the y-z plane. For an arbitrary point (x,y,z) , B_x , B_y , and B_z are found by scaling the two dimensional Poisson value from one plane by the rate of change of B_y in the other plane. The result of this calculation is a three dimensional map of B_x , B_y , and B_z in a 2 x 2 x 2 inch³ grid.

III.5.2 Drift Chambers

The drift chambers are used to measure the angle of

deflection resulting from the analyzing magnets in order to determine the daughter particles' momenta and (assuming the particle type) to reconstruct the invariant mass of the kaon. Good mass resolution is needed in order to suppress backgrounds. Thus good position resolution is required. The chambers need to be as close to the neutral beam as possible in order to maximize acceptance. The mass of the chambers must be minimized in order to reduce multiple scattering which will degrade the resolution of the spectrometer.

Each drift chamber module consists of two X measuring and two Y measuring planes of sense wires attached to a G-10 plate which is supported by an aluminum frame and covered with aluminized Mylar. The sense wires are 0.001-inch gold plated tungsten spaced 0.4 inches apart, and the two planes which measure the same coordinate are offset by one-half a cell so that the cell structure is hexagonal. This configuration reduces the total number of wires needed and also allows the resolution of left-right ambiguity of tracks. The field wires are 0.0043-inch copper-beryllium and are nominally maintained at 2500 volts. Each module is approximately 0.0015 radiation lengths thick. The gas flow was a mixture of 49% argon, 49% ethane and 2% ethanol, and provided a complete gas exchange every six hours.

The sense wires are capacitively coupled to

preamplifier and discriminator cards which are attached directly to the aluminum frames of the drift chambers, after which the signal is carried to the input of the amplifier-meantimer-discriminator (AMD) boards. The output of the AMD boards is carried to TDC's, and is also used in the Level 1 trigger decision. Each drift chamber plane operated at approximately 99% efficiency during the run. The intrinsic resolution for each drift chamber plane is given by

$$\sigma_{\text{DOCA}} / \sqrt{2} \approx 120\mu\text{m} \quad (3.6)$$

where σ_{DOCA} is the resolution of the sum of the DOCA for two adjacent wires.

III.5.3 Trigger Scintillator Counters

X and Y measuring planes of trigger scintillator counters are located just upstream and downstream of the Cerenkov counter. Each plane contains 60 X measuring slats which are $2.0 \times 180.0 \text{ cm}^2$, and 63 Y measuring slats which are $2.8 \times 128.0 \text{ cm}^2$. The upstream slats are 0.5 cm thick and the downstream slats are 1.0 cm thick. The X measuring plane has phototubes at both the top and bottom which are attached to two adjacent slats. A single phototube is attached to the outside end of the Y measuring slats.

The trigger scintillator counters are glued directly to 1-inch Hamamatsu R1398 phototubes. The phototube signal is carried to discriminators via coaxial RG-8 cable, and the dual output is sent to the Level 1 trigger and TDC modules. The average efficiency for each plane is greater than 99%.

III.6 Electron Identification

The electron identification is performed by a threshold Cerenkov counter and a lead glass calorimeter. The atmospheric-pressure Cerenkov counters are used to provide a fast electron signal for the Level 1 decision and to identify electrons in the offline analysis. The design goal of the Cerenkov counter is to maximize the detection efficiency of electrons from $K_L \rightarrow \mu e$ and to have a high momentum threshold for pions and muons. It is also desirable to minimize knock-on electron production and photon conversion in the counter. The lead glass array collects Cerenkov light of particles passing through, so that the amount of energy deposited can be converted into the energy loss of the charged particle.

III.6.1 Cerenkov Counter

Each Cerenkov counter box consists of a welded aluminum frame 3 meters long by 1.6 meters wide. The upstream and downstream windows are made of 1/32 inch aluminum and the ribbed supports are on the outside in order to reduce the amount of material in the particles' path. A continuous flow of 40% nitrogen and 60% helium was maintained during the run, which provides a pion

threshold of approximately 8.2 GeV/c and a muon threshold of 6.2 GeV/c. The index of refraction of the gas was measured with a two-arm Mach-Zehnder interferometer illuminated with a helium-neon laser. Two gas cells are evacuated and one cell is filled with gas from the Cerenkov counter. The fringes from the interference pattern are counted by a phototransistor; 33 fringes correspond to $(n-1)$ of 1.4×10^{-4} .

Each box contains eight spherical mirrors, four in the X direction and two rows in the Y direction, which are supported by a 0.020-inch aluminum frame. Each mirror is made of 0.25-inch Lucite with a thin aluminum coating. The center of the mirrors is 2.55 meters from the upstream window or 29.86 meters from the production target. Each mirror measures 35 cm in X by 89 cm in Y with a radius of curvature of 2.2 meters. The focal point of each mirror is a 6.5 inch quartz window. Aluminized Mylar light funnels bring the light to five-inch RCA 8854 Quanticon phototubes. Three layers of magnetic shielding protect the phototubes from the fringe fields of the analyzing magnets. Dry nitrogen is flowed through the tubes to prevent damage from helium contamination. A thin layer of p-terphenyl, which acts as a wavelength shifter, was applied to the phototubes in order to increase the sensitivity to the shorter wavelengths. The average electron track produces approximately five photoelectrons.

The signals from the Cerenkov counters are carried to the electronics area via coaxial RG-8 cables and split asymmetrically. Twenty percent of the signal is sent to a discriminator with a threshold of 20 mV, which corresponds to approximately a single photoelectron. The discriminator has parallel outputs: one is used by the Level 1 trigger logic, and the other is sent to TDC's. The remaining 80% of the signal is digitized in custom-built ADC's.

III.6.2 Lead Glass

Additional separation of electrons from muons and pions is provided by a lead glass array. The array consists of two layers: an upstream active converter layer of 3.3 radiation lengths and a downstream absorber layer of 10.5 radiation lengths. The entire array is supported by an aluminum frame and housed inside a light proof wooden hut.

The converter layer contains 13 blocks in the X direction and 2 blocks in the Y direction on either side of the neutral beam. Each block measures 10.9 x 90 x 10 cm³ so that the total span of the converter layer is approximately 1.42 meters in X by 1.80 meters in Y. The blocks lying nearest the neutral beam are attached to fast Amperex XP3642 phototubes while the outer blocks have

slower EMI 9531R phototubes.

The absorber layer contains 9 blocks in the X direction and 12 blocks in the Y direction. Each block measures 15.3 x 15.3 x 32.2 cm³ for a total area of 1.38 meters in X by 1.84 meters in Y. The inner blocks are attached to fast Amperex 58AVP and 58DVP phototubes while the outer blocks are attached to slower EMI 9618R phototubes.

The signals from each block are carried to a patch panel on the light-tight hut via coaxial RG-58 cable, and from there to the electronics area via coaxial RG-8 cable. The signal is split asymmetrically: 20% goes to amplifiers and discriminators and then is sent to the Level 1 trigger logic and also to TDC's. The remaining 80% of the signal is sent to ADC's.

III.7 Muon Identification

Following the lead glass array is a steel wall 91.0 cm thick, or approximately six nuclear interaction lengths, which serves as a hadron filter. Behind the steel is a scintillator hodoscope which provides good time and space resolution of muon tracks. Following the muon hodoscope there is a muon rangefinder made of proportional wire chambers placed in between marble and aluminum degrader.

III.7.1 Muon Hodoscope

The muon scintillator hodoscope begins approximately 5 cm downstream of the hadron filter steel, or 33.68 meters downstream of the production target. The Y measuring plane is the more upstream, followed by a 12.5 cm wide aluminum frame, and finally the X measuring plane. The Y measuring plane consists of 14 horizontal slats, each measuring 2.54 x 18.7 x 228.6 cm³, while the X measuring plane contains 11 vertical slats, each measuring 2.54 x 18.7 x 269.2 cm³. Each slat is made of Bicron BC408 scintillator and is wrapped in aluminized Mylar and photo-grade polyethylene. The last 15 cm of the phototube end of each slat is tapered from 18.7 to 5.1 cm and

attached to two-inch Amperex XP2230 phototubes (the X measuring slats have phototubes on both ends while the Y measuring slats have phototubes on the outside: the beam side end is blackened in order to reduce reflections). The phototube efficiency during the run was greater than 99%.

The signals from the muon hodoscope are carried by coaxial RG-8 cable to discriminators, with thresholds of 30 mV, located in the electronics area. The dual parallel output of the discriminator carried one output to TDC's, while the other signal was used in the Level 1 trigger decision.

III.7.2 Muon Rangefinder

The muon rangefinder was designed to record and stop muons in the momentum range from 1.5 GeV/c to 6 GeV/c. Thirteen pairs of proportional wire chambers on either side of the beam are placed between marble and aluminum degrader. There are 150 slabs of marble and 50 slabs of aluminum, each 7.62 cm thick (the marble slabs consist of four smaller pieces which are glued together). The degrader is spaced in order to give an average $\frac{\Delta p}{p}$ of 10% at each gap. The chambers and degrader are supported by two large aluminum frames on either side of the neutral beam, and a helium bag is placed in the beam to reduce

nuclear interactions. The structure is approximately 12.5 meters long and begins 34.4 meters downstream of the production target.

The proportional wire chambers are formed by gluing together 19 cm wide extruded aluminum panels. Each panel contains eight cells measuring 1.2 by 2.1 cm, strung with two parallel wires spaced 1.06 cm apart. The cell wall is at an angle 30° to the normal so that the cell geometry is a parallelogram; this increases the probability that a track is likely to pass through gas and thus increases the chamber efficiency.

The 0.003-inch gold plated tungsten wires were strung with 500 grams of tension and attached by being crimped to a stainless steel tube held in place by a molded plastic end cap. The tension of each wire was tested by measuring the resonant frequency of the wire with an oscillating voltage applied in a static magnetic field.⁴⁹

The chamber planes were formed by gluing the strung panels together at the edge. Aluminum skins were glued across the plane to give better structural support and also to provide an RF shield for the electronics. The X measuring planes contain 12 panels, each 3.01 meters long, while the Y measuring planes have 16 panels that are 2.25 meters long so that the span of both the X and Y planes is $2.25 \times 3.01 \text{ m}^2$. During the run the nominal voltage on

each wire was 2650 V and a gas flow of approximately 49% argon, 49 % ethane and 2% ethanol was maintained.

The wires are capacitively coupled to a pre-amplifier card attached to the aluminum skins. The signals next go to an amplifier-discriminator card also attached to the chambers, and are then carried to latch modules in the electronics area via flat Ansley cables. Performance criteria for the muon rangefinder are given in Appendix A.

III.8 Data Acquisition

A specially designed data acquisition system was developed in order to accommodate the high data-taking rate required for the experiment. Fast ADC and TDC modules, together with a highly parallel three-stage buffered pipeline, allow readout with almost no dead time.⁵⁰ The custom-designed digitizing components can digitize times and charges in less than 200 ns and have a two-stage latch buffer so that one event can be stored while another is read out. Approximately 230 boards, or 5000 channels, reside in 24 crates. A crate controller module performs a sparse data scan on the modules in each crate and can send the data to any one of eight 3081/E processors. The data are written directly to the 3081/E memory, where a dual port interface with 16-bit register reduces the dead time introduced from writing to and uploading the memory boards. The readout supervisor, which consists of custom-designed CAMAC modules, communicates with the various components of the acquisition and controls the flow of data. The online acquisition program, operating from a DEC Micro-Vax, uploads data from the 3081/E processors and writes it to magnetic tape. The data are also monitored online in order to verify that the detectors and acquisition system

are functioning correctly.

III.8.1 Front-End Electronics

The front-end electronics includes TDC's, ADC's, and latches. The UCLA-designed TDC's are used to digitize the hit times in the drift chambers, trigger counters, Cerenkov counters, and muon hodoscope. Each module consists of a 32-channel, 6-bit TDC with 2.5 ns least count and 160 ns range, with less than 0.8 ns r.m.s. error per channel. The stopped time is digitized relative to the start signal from the Level 1 trigger. Each channel contains a 6-bit set of flip-flops (this is the first stage latch) and the first "stop" for each channel clocks the state of these 6 bits. A 100 MHz oscillator located in the crate scanner drives all the clocks in one crate.

The Stanford-designed ADC's⁵¹ are used to digitize the charge in the phototube signals from the lead glass and Cerenkov counters. Each module consists of a 12-channel 8-bit bilinear ADC. The bilinear circuit provides a wide dynamic range (100 pC) while maintaining sensitivity to small signals: each ADC count (above the pedestal) corresponds to 150 fC for small pulses and 470 fC for large pulses. Tests indicated that the r.m.s. noise is about 210 fC and the integral non-linearity is less than one count. The Level 1 trigger signal starts

the gate (which ranges from 20ns to 150 ns) for all 12 channels in a module. Each channel is digitized with a SONY CMX20052A chip, and the 8-bit output serves as the stage 1 latch. Each hit channel also sets a flip-flop which provides a flag for the sparse data scan.

The Los Alamos-designed latch modules are used to digitize hit information from the muon rangefinder as well as trigger diagnostics and other trigger information from the readout supervisor. Each module consists of 3 sets of 32 channels which share a common clock. For the muon rangefinder, a Level 1 signal starts a 160 ns gate while the trigger information is read out without a latching clock. There is no sparse data scan for the latch modules; every channel is read out.

III.8.2 Crate Scanner and Readout Supervisor

The crate controller collects data from the modules in each crate and sends it to the 3081/E processors. Control signals from the readout supervisor cause the data in the stage 2 latches of each module to be strobed into the 12-bit "1st pipeline register". The 2nd pipeline register is a 16-bit register on the crate scanner, where each word contains a 4-bit station address. A "master" crate scanner sends the data in the 2nd pipeline register directly to the memory port of the 3081/E processors (the

3rd pipeline register) while a "slave" crate scanner is read out through a neighboring master (this configuration reduces the number of ports needed on each memory board). Each crate scanner has a counter to count the number of clock pulses it has received from the readout supervisor. When this counter reaches its preset limit, corresponding to a full 3081/E memory port, the readout supervisor sends the next event to the next available 3081/E.

The front-end modules of each crate are divided into between one and four "regions". During readout, when a region boundary is crossed, a 16-bit "region word" is inserted into the 2nd pipeline register, which contains a master/slave bit, a fine event number (for diagnostics), and the region word and word count for that region. When all the data from a crate have been read into the 2nd pipeline register, a "crate word" is generated by the crate scanner which contains the crate identification number and the total word count.

The front-end modules have a two-stage latch; no data can be taken when the first stage latch has an event, and thus the readout supervisor will either shift the event into the second stage latch or else clear it as quickly as possible. From the second stage latch the event is either strobed into the 1st pipeline register or over-written by the next event. In addition to controlling the flow of data, the readout supervisor

provides information about each event such as the spill number (which is reset at the beginning of each data run), the number of Level 1 triggers per spill, and the time of the event within the spill.

The readout supervisor consists of several custom-designed CAMAC modules using ECL and F TTL logic. The main readout supervisor module controls the movement of data and generates strobes based on the state of various parts of the readout system (such as what data are in the front-end modules, the state of each 3081/E, and the Level 1 trigger decision). Two trigger latch modules are used to receive the Level 1 trigger word for each event and send it to the front-end latches. A crate scanner output module provides the signals (a total of 16 signals which are fanned out to each crate scanner) which control the flow of data through the front-end electronics and onto the data pipeline. Four crate scanner I/O modules provide communication between the readout supervisor and individual crate scanners. A counter module contains the spill, time, and event counters and sends the output to a latch module. The 3081/E selector and 3081/E driver modules control the flow of data to an available 3081/E.

III.8.3 3081/E Processors

The 3081/E processors are a Stanford design⁵² with

modifications to the memory boards and interface. The memory boards were modified by adding external ports: each "turbo" board has four (17-pair) connectors corresponding to four columns of memory. Hence, each processor requires three turbo boards (each with 1 Mbyte of static memory) in order to read out all 24 crates in the system. The processors communicate with the host Micro-Vax via a DR11W interface in the Micro-Vax and a custom processor interface in the 3081/E.

The readout supervisor sends the strobe to the memory boards which clocks the data from the crate scanners into the memory (the processor is off while the memory is loaded). A re-start signal from the readout supervisor is sent to the controller of each processor in order to start the processor at the end of the proton spill or when its memory board is full.

III.8.4 Online Acquisition Program

The online data acquisition program consists of several parallel processes running under VMS. In addition to providing control of the data taking and uploading of raw data from the 3081/E processors, the acquisition program allows users to monitor the data being taken in order to verify the operation of the detector.

The user interacts with the acquisition program

through the main acquisition process which allows control of the system via interactive menus. The data handler process performs the initialization and communication with the CAMAC and 3081/E systems, and writes the data into the main buffer. The tape handler communicates with the tape drives and writes the main buffer to tape. The analyzer allows simple analysis of the incoming data; user specified histograms are filled and portions of the raw event buffer can be examined (the histogram buffer is controlled by the arbitrator). The events used by the analyzer are siphoned off from the main buffer by the cache control. The event cache can also be sent over the local DECNET network so that further online analysis, such as event display programs, can be performed on remote computers.

III.9 Triggering

A multi-stage trigger was developed in order to accommodate the large kaon flux. The Level 1 trigger uses the trigger counters (with resolving time of ± 7 ns) and upstream drift chambers (with resolving time of ± 27 ns) to select events with two charged tracks, and identifies electrons and muons with the Cerenkov counter and muon hodoscope respectively. Fast ECL modules under CAMAC control provide a Level 1 trigger decision in less than 300 ns. The Level 2 trigger uses the hit information of the trigger counters in order to perform a crude estimate of the invariant mass (using a hardware memory look-up). The Level 2 trigger was available during the 1988 data taking but was not used as a filter. The Level 3 trigger performs online track reconstruction and calculates the invariant mass based on the event type as given by the Level 1 trigger.

III.9.1 Level 1 Trigger

All signals from the trigger counters are discriminated with LeCroy LRS4416 modules at a threshold of 30 mV. The X measuring signals are then sent to Los Alamos-designed meantimers. The "OR" of each plane is

formed with LeCroy LRS5464 modules, and a Level 1 trigger requires hits in all eight planes of counters. The X and downstream Y trigger counters were used as a strobe for Level 1 as well as providing TDC starts, ADC gates and latch strobes. The "OR" of all top and bottom tubes were meantimed, and then the front and back modules on either side were meantimed again. Finally, the left and right side times were meantimed to give the strobe signal. In order to insure that there is an upstream track associated with the trigger event, the Level 1 logic requires that there be hits in three of the first four drift chamber planes (the first two drift chamber modules) in which each plane is the (meantimed) "OR" of each hit wire pair.

The Level 1 particle identification is performed by the Cerenkov counter and the muon hodoscope. For the Cerenkov counter, the output of the discriminator is used to form an "OR" for the left and right side. For the muon hodoscope, the X measuring signals are meantimed and an "OR" of the X and Y measuring planes is formed. A muon signal requires a hit in the X and Y plane.

Table III.2 gives the requirements for various trigger assignments. In the Table, D is the drift chamber signal, T is the trigger counter signal, LC and RC are the left and right Cerenkov counters, and LM and RM are the left and right hodoscopes. \bar{C} and \bar{M} are Cerenkov and muon hodoscope vetoes. The dilepton trigger bits are not

exclusive, so that if both sides of the Cerenkov and muon hodoscope fire, the $e_L\mu_R$ and $e_R\mu_L$ trigger bits will both be set. During the first part of the run the $\pi\pi$ trigger was prescaled by a factor of 500 while the minimum bias trigger was prescaled by a factor of 1000; the prescale factors were later changed to 100 and 2000 respectively. The trigger bits are sent to the trigger latch module of the readout supervisor and eventually written to tape.

Table III.2
Level 1 Trigger Requirements

<u>Trigger</u>	<u>Requirement</u>
$e_L\mu_R$	$D \cdot T \cdot LC \cdot RM$
$e_R\mu_L$	$D \cdot T \cdot RC \cdot LM$
$\pi \pi$	$D \cdot T \cdot \bar{C} \cdot \bar{M}$
Min Bias	$D \cdot T$

Table III.3 gives typical detector singles rates and Level 1 rates for 1×10^{13} protons per pulse.

Table III.3

Level 1 Trigger Rates (for 10^{13} protons per pulse)

Trigger Counter, Front X Plane	1.2×10^7
Drift Chamber Module 1	6.0×10^6
Cerenkov Counter	4.5×10^6
8-Fold Trigger Counter Coincidence	1.8×10^6
Level 1 Minimum Bias	1.3×10^5
Level 1 Dilepton	4.0×10^4

III.9.2 Level 3 Trigger

In the first stage of the Level 3 program, good pairs of hit wires are searched for in the first five drift chamber planes (the first three X and first two Y measuring planes). The time sum (corrected by "time zero") for each pair of adjacent wire hits is compared with the expected time sum for the given plane and wire configuration. Up to four good time sums are allowed in each plane, and if no good time sums are found, one bad time sum is allowed. The event is rejected if even a bad time sum cannot be found.

In the second stage of the Level 3, a series of optimization criteria is applied to select the best hits.

The best two hit pairs for each plane (based on their time sums) are tried first. A look-up table is used to check whether the hit pairs in the first two modules have a high probability of being correlated. Next, tracks made from the two best hit pairs in the two upstream Y measuring planes are required to project on to the fifth drift chamber module. The tracks from the two upstream X measuring planes are required to be diverging from the beam. Also, the Z position of the reconstructed vertex for the X and Y view is compared. Next, the hit position of the X view in the third drift chamber module is compared to the projected position from the first two modules. Finally, the charge of the two tracks is compared. Different hit pairs are tried in order to better satisfy each criterion (although not all possibilities are tried).

The third stage of the Level 3 calculates the invariant mass using tracks from the best hit pairs. The track momentum is calculated from the angle of deflection resulting from the first analyzing magnet. The collinearity angle, defined as the angle between the momentum sum of the two tracks and the kaon direction (the vector from the production target to the reconstructed vertex position), is also calculated. Events with collinearity greater than 20 mrad are cut. The invariant mass is calculated for each Level 1 trigger type and is

required to be between 460 and 550 MeV.

Chapter IV

Data Analysis

IV.1 Introduction

The goal of the offline data analysis was to search for $K_L \rightarrow \mu e$ candidates in the μe trigger data and to identify good $K_L \rightarrow \pi\pi$ events in the minimum bias data in order to normalize the sensitivity of the experiment. The data sample was first reduced in two stages of production analysis which selected events with one clean track on each side of the spectrometer. The performance of each detector was studied carefully in order to determine the particle identification criteria for electrons and muons. Cuts on track qualities were chosen to maximize the background suppression and minimize the inefficiency introduced. All the analysis described here was performed on the Brookhaven IBM 3090 computer.

IV.2 Pattern Recognition

The first stage of the offline analysis is a pattern recognition package which attempts to construct good tracks from drift chamber wire hits. There are three steps to the pattern recognition program: there is a search done for good hits by calculating the sum of the distance of closest approach for two adjacent drift chamber wires; there is a search for good X - view and Y-view tracks and a calculation of track qualities, and there is a search for the best vertex position using all possible three-dimensional tracks and a calculation of vertex qualities.

The first step of the pattern recognition program, calculating the sum of the distance of closest approach (DOCA) for adjacent drift chamber wires, is useful in removing accidental hits. The DOCA of each single wire hit is required to be between -0.0005 m and 0.006 m. Next there is a search for three adjacent hit wires which can occur when the track lies near a drift-cell boundary. The DOCA sum of the N th and $(N+2)$ th wire is required to be greater than 0.0042 m while the $(N+1)$ th DOCA is required to be less than 0.0018 m. If found, the three hits are stored as a single-hit pair. Then there is a search for good pairs of hits where it is required that the DOCA sum

for the two wires be within 2.5 sigma of the mean. In this case the orientation of the track to the wires is significant: if the smaller wire number of the pair is even, the DOCA sum will be less than the sum if the smaller wire is odd. This effect is accounted for in the program. The problem of tracks with missing hits must also be considered; in order to increase the reconstruction efficiency the program allows one missing hit per view per side (one miss in ten wires). Hence at this step a single wire hit, if there is one, is made into two imaginary good DOCA pair hits; there are two pairs because there is a left-right ambiguity for a single wire hit.

The next step in pattern recognition is the search for good X-view tracks. Because the two analyzing magnets have equal and opposite momentum kicks it is required that the track direction in the two most-upstream drift chambers (before the first magnet) be the same as in the two most-downstream drift chambers (after the second magnet). A cut of 0.070 rad is placed on the difference in X direction between the upstream and downstream track candidate. Next the expected hit position at the third drift chamber module (in between the magnets) is calculated from the upstream and downstream track candidates. The difference between the expected and actual hit positions is required to be less than 0.040 m

for tracks with ten hits or 0.080 m for tracks with nine hits. The search for good Y-view tracks is simpler because there is little or no magnetic deflection in this direction. In this case the four most-upstream hits and the four most-downstream hits are used to determine a single line. In the third drift chamber module it is required that a good DOCA pair lie within 2 mm of this line or that an imaginary pair lie within 4mm of the line. The difference in the front and back Y trajectory is required to be smaller than the focussing effect of the analyzing magnets.

After finding good X and Y-view tracks, corrections are made to the actual hit positions. If the DOCA pair resulted from three adjacent hits or a single hit, then the left-right ambiguity must be resolved. In the case of a normal two-wire hit the position is corrected if the track has a large opening angle since, for large opening angles, it is possible for the track to pass on the same side of the X and X' wire instead of between them so that the DOCA sum of the pair rather than the difference is a constant. Next a least squares fit to a straight line is performed for the X and Y track and the reduced χ^2 for each track is required to be less than 25, where the χ^2 is the sum of the front χ^2 (from the first two drift chamber modules), the middle χ^2 (from drift chamber module 3) and the back χ^2 (from drift chamber modules 4 and 5).

The final step in pattern recognition is to calculate the vertex position and vertex qualities. First, all three-dimensional tracks, which are formed from all combinations of X and Y view-tracks, are searched and the best vertex is chosen based on the DOCA between the two nearest tracks (see Fig. 19). Next the distance between the best vertex and each track is calculated, as well as other vertex information such as track momentum and reconstructed target position. Finally a loose cut of 80 mrad is placed on the collinearity θ_c of the vertex; that is, on the angular difference between the unit vector from the target to the vertex and the unit vector of the momentum sum of the two tracks.

IV.3 Track Fitting

At the next stage of the offline analysis a more rigorous fit is performed on the tracks found in pattern recognition. There are five steps to the fitting program: a calculation of the trajectory and momenta in the front and back spectrometer, a calculation of uncertainties and χ^2 values for all tracks, a more sophisticated study of the left-right ambiguity problem, a χ^2 calculation for the momentum match and trajectory match at the third drift chamber module, and a recalculation of the vertex position and vertex χ^2 .

In order to calculate the track momenta, the drift chamber wire hits are used to determine the upstream and downstream track position and trajectory. An initial estimate of the track momentum is taken from the pattern recognition results for the front spectrometer. Then using the full magnetic field map, each track is swum to the third drift chamber module while the momentum is varied until the actual and projected hit positions at the third drift chamber match. This procedure is repeated for the back spectrometer.

The next step is to calculate the uncertainties and χ^2 values for all tracks. There are three contributions to the track uncertainties: the intrinsic drift chamber

resolution, the angular uncertainty due to errors in position measurement in the first drift chamber, and uncertainty in the track trajectory due to scattering in the vacuum window and first drift chamber module. The two contributions to the X-view χ^2 are the momentum difference between the front and back spectrometer and the X trajectory difference between the front and back spectrometer (Fig. 20). The two contributions to the Y-view χ^2 are the difference in the Y position projected at the third drift chamber module from the front and back spectrometer and the Y trajectory difference between the front and back spectrometer.

Tracks with missing hits are optimized by checking the left-right assignment for single-wire hits. If there is a single-wire hit in the track, the left-right assignment will be switched and the contributions to the X and Y χ^2 checked. If these quality checks improve with the new assignment the track will be refit and errors will be recalculated with the new position assignment.

The last step in fitting is to find the best vertex from the reconstructed tracks using an algorithm similar to that used in pattern recognition. First, all three-dimensional tracks are searched and the vertex position is chosen from the tracks with the shortest DOCA (weighted by the uncertainty in the track trajectory). Then the distance from the vertex to the two tracks is calculated,

as well as the track trajectory from the vertex. The vertex χ^2 is calculated based on the DOCA of the two tracks.

IV.4 Production Analysis

In the first pass of offline analysis, pattern recognition is performed in order to select events with good tracks. To reduce CPU time a pre-cut was placed on the collinearity of the dilepton trigger events at 10 mrad as calculated by the Level 3 trigger (compared to the online cut of 20 mrad which existed for most of the run). This pre-cut was checked by studying its effect on a $K_L \rightarrow \pi\pi$ sample which was selected by using particle identification in the online trigger. The result was that $(98.7 \pm 0.4) \%$ of the $K_L \rightarrow \pi\pi$ events pass the cut while the CPU time was reduced by more than a factor of two. The $K_L \rightarrow \mu e$ triggers were required to have a Level 3 calculated K_L mass between 460 and 550 MeV which is the same as the online cut for most of the run. The minimum bias sample was not cut by collinearity or mass, but an additional prescale factor was added. The Level 1 prescale factor for minimum bias changed from 1,000 to 2,000 during the run; hence the additional software prescale was set to six or three such that the total prescale factor is always 6,000.

The first pass of the offline analysis began on April 11, 1988 and concluded on May 23, 1988. A total of 2,134 tapes was analyzed producing 229 data summary

tapes. The raw data and the derived hit information for all detectors were written out for all events passing pre-cuts. The pattern recognition information was written out for reconstructed events (events with one track on each side of the spectrometer). Unreconstructed events were saved with the hope that the pattern recognition program could be improved in the future.

Several quantities were monitored throughout the pass one production analysis to insure the stability of the data taking. The reconstruction efficiency averaged over the entire run was $(55.64 \pm 5.9) \%$ for dilepton triggers, $(44.03 \pm 4.6) \%$ for minimum bias triggers, and $(59.85 \pm 5.5) \%$ for two pion triggers. Of all reconstructed events, $(34.79 \pm 4.8) \%$ were good $K_L \rightarrow \pi \pi$ candidates from the two pion trigger data while $(0.68 \pm 0.26) \%$ of the minimum bias events were good candidates. A good candidate is defined as having a reconstructed K_L mass between 490 and 506 MeV and collinearity less than 2 mrad. Hence, within statistical errors, each tape contains the same number of $K_L \rightarrow \pi \pi$ events.

In the second stage of offline production analysis, cuts are performed on the results of pattern recognition and fitting is performed on events which pass these cuts. The cuts were chosen to reduce CPU time required to do the fitting, while retaining a sufficient sample of each trigger type. The $K_L \rightarrow \mu e$ trigger events were required to

have a K_L mass greater than 475 MeV, while the two pion and minimum bias trigger events were required to have mass greater than 460 MeV and 450 MeV respectively. All trigger types were required to have collinearity less than 3 mrad as calculated by pattern recognition. The track-fitting information was written out on data summary tapes for all events passing these cuts.

The second stage of production analysis was performed from April 21, 1988 through May 23, 1988 on all of the 229 pass one data summary tapes. This stage produced five tapes containing a total of 250,000 $K_L \rightarrow \mu e$ trigger events and two tapes containing 86,000 minimum bias events.

IV.5 Particle Identification

At the end of the second pass of offline production analysis there remained a large sample of $K_L \rightarrow \mu e$ trigger events for which the Level 1 trigger simply requires a Cerenkov counter hit on one side of the spectrometer and a muon hodoscope hit on the other. The next step in data reduction is to make further cuts on the particle identification of each track; this is done primarily by comparing each detector's expected response for various types of particles with the actual response. The offline program uses the track information from pattern recognition to swim the tracks through the entire detector just as was done in the Monte-Carlo program, except that the multiple scattering simulation is turned off. The swum tracks are used to predict the response of each detector and this prediction is compared to actual hit information.

The match between the expected and actual detector response is frequently given by a confidence level measurement. The confidence level is defined as the probability that, for a given particle identification hypothesis, the χ^2 would exceed the observed χ^2 value (found by integrating the χ^2 distribution from infinity to the observed χ^2 value). A correct hypothesis should

have a flat confidence level distribution between zero and one while an incorrect hypothesis should be peaked near zero. Thus, by cutting at a small confidence level value there should be a small fraction of good events which are cut, while a large fraction of misidentified events are cut.

The response of the Cerenkov counter is given as the confidence level of the time of the TDC hit. Reconstructed tracks from the pattern recognition program are projected to the mirrors of the Cerenkov counter and a confidence level is returned for the hit time of any mirrors lying on the expected light cone of the track. The confidence level is taken from a look-up table which consists of 12 time bins each 2.5 ns wide, and which is generated from time distributions of well identified electron tracks. The electron detection efficiency of the Cerenkov counter was tested by studying the response to electrons from $K_L \rightarrow \pi e \nu$ decays; this decay is selected by making appropriate kinematic, track quality, and particle identification cuts. The electron efficiency for each phototube was measured; a good hit was required to have a time confidence level greater than 1%. The overall electron efficiency for $K_L \rightarrow \mu e$ was determined by weighting each phototube efficiency by its illumination from Monte-Carlo simulated $K_L \rightarrow \mu e$ events.

It was discovered during the run that the Cerenkov

efficiency for $K_L \rightarrow \mu e$ could be improved by realigning the outer two mirrors. This adjustment was made following data run 3,181, at which time a misalignment in mirror ten was also discovered and corrected. The Cerenkov electron efficiency is $(88.7 \pm 0.3 \pm 1.0) \%$ for runs before the mirror adjustments and $(93.0 \pm 0.3 \pm 1.0) \%$ after the adjustments. The overall electron efficiency, determined by properly weighting these two numbers, is $(89.3 \pm 0.3 \pm 1.0) \%$. A 1% confidence level cut should be 99% efficient: the efficiency is lower due to the fact that some fraction of events will produce too few photoelectrons to trigger the TDC.

The probability of misidentifying a pion or muon with a time confidence level cut of 1% was determined by looking at the pion track in $K_L \rightarrow \pi e \nu$ decay as a function of track momentum and beam intensity, in which the pion track was required to be below the Cerenkov threshold of 8 GeV/c. The probability that the pion would pass the Cerenkov time confidence level cut of 1% is $(1.0 \pm 0.04 \pm 0.10) \%$.

The momentum dependence of the time cut was studied by measuring the individual phototube efficiencies for four momentum bins: 0-2 GeV/c, 2-4 GeV/c, 4-6 GeV/c and greater than 6 GeV/c. The only measurable momentum dependence is in the 0-2 GeV momentum bin for runs prior to the mirror adjustments due to the lower efficiency of

mirror ten. The time efficiency was also studied as a function of track angle and no angle dependence was found.

A confidence level table was also generated for the Cerenkov ADC pulse height. However, adding a pulse height confidence level cut of 1% excluded almost no events (0.04% for inbends and 0.0% for outbends) while the misidentification probability for this cut was higher than the time cut. Hence the pulse height cut was not used in electron particle identification.

The lead glass array can be used to discriminate electrons from pions and muons because electrons will deposit nearly all of their energy as they pass through. The offline program projects tracks to the front face of the converter block layer and the back block layer. Because the electron will cause an electromagnetic shower as it passes through, the energies deposited in the hit block and adjacent blocks are summed together. The ADC counts for each block are converted into energy using calibration constants for the appropriate block and time of the event (there are a total of seven sets of calibration constants for the entire run). There are two requirements for a track in the lead glass to be considered an electron: first the ratio E/p of the total energy deposited to the track momentum must be greater than 0.75 (Fig. 21). Second, the ratio of the energy deposited in the converter layer compared to the back

block layer is required to be greater than 0.045. The electron efficiency is measured for each of the seven sets of calibration constants by selecting electrons from the decay $K_L \rightarrow \pi e \nu$. The electron efficiency for $K_L \rightarrow \mu e$ is determined by properly weighting each set of calibration constants and weighting by the Monte-Carlo illumination. The final electron efficiency for the lead glass is $(94.2 \pm 0.3 \pm 0.1) \%$. The probability of misidentifying a pion as an electron, measured by counting how many well selected pions passed both of the lead glass cuts, was found to be $(3.3 \pm 0.2) \%$.

The particle identification for the muon hodoscope is contained in a confidence level measurement which is the convolution of three time and two space χ^2 measurements. Each track is projected onto the muon hodoscope and a confidence level is returned for the difference between the actual and projected hit positions for both the X and Y measuring planes. The confidence levels were calculated by studying well-selected muon tracks from $K_L \rightarrow \pi \mu \nu$ decays and requiring a good space match hit in the complementary muon hodoscope plane and well-timed hits in both planes. The confidence level table is two-dimensional, binned by space match and momentum. There are six momentum bins: below 1 GeV/c, 1-2 GeV/c, 2-3 GeV/c, 3-4 GeV/c, 4-5 GeV/c and greater than 5 GeV/c for which the space match distributions for lower

momenta are wider due to multiple scattering effects.

Time confidence levels are returned for the Y-measuring and both X-measuring phototubes from a two-dimensional look-up table with one ns time bins and six momentum bins. For both planes of the muon hodoscope the time and space confidence levels are combined by forming the individual χ^2 values (using the IMSL library routine MERFCI), and integrating the sum of the individual χ^2 distributions using the CERN library function PROB. The total confidence level for the muon hodoscope is determined by combining the X and Y plane confidence levels.

The requirement for a track to be considered a muon in the muon hodoscope is a total confidence level greater than 1%. This cut is $(97.6 \pm 0.5 \pm 0.3)$ % efficient as measured from well-selected muons from $K_L \rightarrow \pi\mu\nu$ decay. This efficiency is less than expected due to correlations between the five individual confidence level measurements which result in a non-flat total confidence level distribution.

The particle identification information from the muon rangefinder is given by comparing the expected track penetration depth to the actual penetration depth (Fig. 22). First each track is projected in a straight line through the entire rangefinder. Real hits are assigned a momentum-dependent space match confidence level based on

the distance between the expected and actual hit, for which the space bin width is one panel (approximately 19 cm) and the momentum bins are the same as those for the muon hodoscope. Rangefinder tracks are then constructed by placing a cut on the space match confidence level to determine whether each hit is associated with the track. In addition, each hit is required to be within one panel width of the previous module hit. The X and Y-view tracks are found independently and are considered to be stopped when there are two consecutive gaps without track-associated hits. The farthest downstream hit of the X or Y track determines the last gap hit. The last gap expected to be hit is calculated by taking the track momentum from pattern recognition and subtracting from that the most likely momentum loss of each gap (determined by a separate Monte-Carlo calculation). A muon track is required to be within three gaps of the expected penetration depth. This cut is $(98.71 \pm 0.07 \pm 0.08) \%$ efficient for identifying muons while the probability of misidentifying a pion is $(22.76 \pm 0.3 \pm 0.5) \%$. Making a tighter cut would reject more background but would reduce the muon efficiency due to the large uncertainty of energy loss at each gap.

IV.6 Track Quality Requirements

The last set of cuts applied to select good events is that which defines the fiducial volume of the apparatus and which checks the quality of each track. Minimum bias data are used to distinguish track characteristics, as calculated by the track fitting program, which have a high probability of being associated with background. The efficiency of each cut is generally given as the fraction of well-selected $K_L \rightarrow \pi\pi$ events which would pass the given cut.

The reconstructed vertex position of the kaon (Fig. 23) is required to be greater than 9.5 m downstream of the target position to insure that all charged daughter particles are created downstream of the second sweeping magnet, B5P2. A measurement of the fringe field using a Hall probe indicated that the field goes quickly to zero downstream of nine meters. However, if the actual vertex position is in a region of magnetic field the reconstructed vertex could be shifted downstream; hence the more conservative choice of 9.5 m was made. This cut was 94.4% efficient for 2π events chosen with mass between 0.493 and 0.503 GeV and collinearity less than 1 mrad.

In order to insure that the event is associated with

an interaction in the target and not the collimator system, a cut is placed on the absolute transverse position at the vertex (Fig. 24 and 25). It was required that $|X/Z|_{\text{ver}}$ be less than 0.0027 and $|Y/Z|_{\text{ver}}$ be less than 0.01. The efficiency of these two cuts was measured to be 99.6% and 99.7% respectively.

A cut was made to remove events which pass through the flange on the vacuum window assembly (Fig. 26). Tracks were projected to the vacuum window and cut if the absolute X position was less than 0.1003 m; this cut is 97.2% efficient. Cuts are also made to remove tracks which pass through the analyzing magnets and their mirror plates, and were found to be 99.7% efficient. In addition, the momentum of each track is required to be greater than 1.5 GeV/c since few muons below this will penetrate through the hadron filter steel. The efficiency of this cut is 98.2%.

Finally, cuts are placed on the χ^2 values calculated by the track fitting program as described in a previous section (Fig. 27-29). The X and Y view χ^2 for each track is required to be less than twenty and the vertex χ^2 is required to be less than ten. The vertex χ^2 cut is 95.6% efficient. Because there is some discrepancy in the track χ^2 distributions between data and Monte-Carlo, a more careful study was done to compare the cut efficiencies for various particle and track types, and the

results are listed in Table IV.1. Pions are selected by making mass and collinearity cuts on the minimum bias 2π sample. Electrons and muons are selected by making appropriate kinematic and particle identification cuts on $K_L \rightarrow \pi e \nu$ and $K_L \rightarrow \pi \mu \nu$ decays respectively. The electron and muon efficiency is found by adding the inbend and outbend efficiency, properly weighted by the inbend to outbend ratio from Monte-Carlo $K_L \rightarrow \mu e$ decay. The efficiency of the X and Y track χ^2 cuts are, respectively, 97.23% and 96.41%.

The individual efficiencies given above are for $K_L \rightarrow \pi\pi$ events which have mass and collinearity cuts but no track quality cuts. The total efficiency of all track quality cuts is 80.8% and is less than the product of the individual efficiencies because of correlations.

Table IV.1

Efficiency of Track χ^2 Cuts

	<u>X View</u>	<u>Y View</u>
<u>MC</u>		
π	98.96 \pm .06	98.84 \pm .06
e	99.76 \pm .08	99.94 \pm .08
μ	99.68 \pm .08	99.93 \pm .08
<u>Data</u>		
π	97.23 \pm .13	96.41 \pm .13
e	96.93 \pm .34	97.50 \pm .34
μ	97.34 \pm .25	97.38 \pm .25

IV.7 Corrections Required

Before calculating the final sensitivity of the experiment it is necessary to correct for physical effects and experimental properties which impact on the sensitivity. These corrections affect the number of $K_L \rightarrow \pi\pi$ events observed and the expected ratio of the $K_L \rightarrow \pi\pi$ and $K_L \rightarrow \mu e$ decay modes.

The Monte-Carlo program described previously is used to measure the acceptance of each decay mode. The acceptances of the 2π and μe decays differ because of respective kinematics and because of the identification criteria for pions, electrons and muons. The latter question requires a definition of each particle type which includes the effects of pion decay, pion interaction, and trigger requirements in a consistent way. The pions in minimum bias data are required only to fire the trigger counters; this is simulated in the Monte-Carlo by requiring the projected pion track to lie within the dimensions of the downstream trigger counter bank. A muon trigger requires a hit in the muon hodoscope; hence in Monte-Carlo the muon tracks must project onto the muon hodoscope. Electron triggers must fire the Cerenkov counter; however this is not a limiting aperture and thus is not required in the Monte-Carlo program. The

probability of pions decaying is also simulated in the Monte-Carlo and the track is accepted only if the daughter muon projects onto the downstream trigger counter plane. The acceptance for $K_L \rightarrow \pi\pi$ is 0.0254 ± 0.0002 while for $K_L \rightarrow \mu e$ it is 0.0173 ± 0.0001 .

A correction must be made for the inefficiency introduced in the μe channel due to trigger requirements. The Level 1 system uses a programmable logic unit to generate a trigger word based on detector hits, and sends this 16-bit word to the readout supervisor where it is eventually written to magnetic tape. The efficiency of generating each trigger bit was studied offline by using particle identification to predict the appropriate trigger bit and comparing this to the trigger word on tape. The μe bit was found to be 1.5% less efficient than the minimum bias bit.

A cut is placed on the Level 3 mass and collinearity calculation for the $K_L \rightarrow \mu e$ trigger events, both online and in the pass one production analysis, while the minimum bias data are always passed through. The efficiency of this cut was measured by checking the Level 3 quantities for minimum bias data which had passed pattern recognition and track fitting. The 2π events were selected using appropriate mass, collinearity, and track-quality quantities from the track-fitting program. Of the good 2π events selected, 79% satisfied the Level 3 mass and

collinearity cuts for $K_L \rightarrow \mu e$.

The number of $K_L \rightarrow \pi\pi$ events measured in the minimum bias data must be corrected for the probability of a pion interacting in the detector. The probability of a pion interacting upstream of drift chamber module five is the product of the total cross section⁵³ and the mass of all material upstream (listed in Table IV.2).

Table IV.2

Thickness of Detector Elements

<u>Element</u>	<u>Material</u>	<u>Thickness (cm)</u>
Vacuum Window	Mylar	0.0508
Drift Chamber	Mylar	0.00254
	Aluminum	0.00254
	Argon	6.84
	Ethane	6.84
Helium Bag	Mylar	0.04064
	Helium	855.0
Trigger Counters	Polystyrene	1.0
Cerenkov Counters	Al window	0.0794
	Helium	153.0
	Nitrogen	102.0
	Plexiglass	0.635
	Al support	0.178

The probability of a pion interacting between drift chamber module five and the Cerenkov counter is calculated using the inelastic cross section⁵⁴ (and accounting for the fact that some pions which interact may still hit the trigger counters). The total probability

of a pion interacting is 0.015.

Finally, the number of $K_L \rightarrow \pi\pi$ events must be corrected by the contamination from $K_S \rightarrow \pi\pi$ events. A Monte-Carlo calculation was used to give the number of $K_L \rightarrow \pi\pi$ events, binned by Z position and kaon momentum. Then a numerical calculation was made of the ratio of the number of K_S and interference terms to K_L for each position and momentum bin. The contamination from K_S and interference terms summed over the entire position and momentum distribution was found to be 2.1% of the minimum bias sample.

Chapter V

Conclusion

V.1 Final Sensitivity

After performing all of the track quality and particle identification cuts described previously, there are no $K_L \rightarrow \mu e$ candidates with mass between 0.493 and 0.503 GeV and collinearity less than 1 mrad. This mass region corresponds to a cut of $\pm 3.2 \sigma$ and the collinearity region is a cut of 3σ . The mass and collinearity distributions for the minimum bias data sample are shown in Fig. 30-32, and the corresponding distributions for the $K_L \rightarrow \mu e$ data are shown in Fig. 33-35.

The number of $K_L \rightarrow \pi\pi$ events is found by performing a background subtraction on the minimum bias events within the specified mass and collinearity regions. The shape of the background is simulated by generating Monte-Carlo minimum bias events. The amount of subtraction was determined by normalizing the Monte-Carlo sample such that the number of events in the tail of the mass peak was equal to the number of events in the same region in the data sample. There were 9,392 events within the mass and collinearity region before the subtraction and 8,398

events after the subtraction.

The systematic uncertainty introduced by the choice of mass window was checked by counting the number of $K_L \rightarrow \pi\pi$ candidates with collinearity less than 1 mrad, after background subtraction, for various choices of mass windows, and found to be 0.15%. The uncertainty introduced by the choice of collinearity was checked by counting the number of $K_L \rightarrow \pi\pi$ candidates for various collinearity cuts, and found to be 1.0%.

The particle identification efficiencies were verified by measuring the ratios $\Gamma(K_L \rightarrow \pi\pi)/\Gamma(K_L \rightarrow \pi\mu\nu)$ and $\Gamma(K_L \rightarrow \pi\pi)/\Gamma(K_L \rightarrow \pi e\nu)$. The number of $K_{\mu 3}$ and $K_{e 3}$ candidates in the minimum bias data sample was determined by applying the appropriate lepton identification and kinematic requirements. The measured values for the two ratios agreed with accepted values¹ within 2.5% and 5.7% respectively.

The single event sensitivity for $K_L \rightarrow \mu e$ is given by

$$\frac{BR(K \rightarrow \pi\pi)}{N_{\pi\pi}} * \frac{A_{\pi\pi}}{A_{\mu e}} * \frac{\epsilon_{\pi\pi}}{\epsilon_{\mu e}} * \frac{\beta_{\pi\pi}}{\beta_{\mu e}} \quad (5.1)$$

where A , ϵ , and β are the acceptance, particle identification efficiency, and trigger efficiency respectively. $N_{\pi\pi}$ is the number of observed $K_L \rightarrow \pi\pi$ events observed multiplied by the prescale factor and pion interaction correction: $8398 * 6000 * (1+0.015-0.021) =$

5.01×10^7 . Substituting all the relevant numbers into the equation above gives the single event sensitivity for $K_L \rightarrow \mu e$:

$$\frac{0.00204}{5.01 \times 10^7} * \frac{0.0254}{0.0173} * \frac{1}{0.810} * \frac{1}{0.778} = 9.48 \times 10^{-11}$$

(5.2)

The single-event sensitivity is the branching ratio at which one event is expected to be observed. The 90% confidence level limit of the branching ratio is the value for which there is a 90% probability that the "true" branching ratio value is not greater than the observed value. From Poisson statistics, the confidence level CL associated with an upper limit N and zero observed events¹ is: $CL = 1 - e^{-N}$ so that a 90% confidence level ($CL = 0.90$) implies an upper limit of $N = 2.3$ events. Thus, 2.3 times the single-event sensitivity, or 2.2×10^{-10} , is the 90% confidence level limit for observing zero events.

V.2 Future

The experimental apparatus described here will be used for future data taking in order to lower the upper limit for $K_L \rightarrow \mu e$. Improvements made since the 1988 running period include better targetting conditions, new electronics (such as flash TDC's and more meantimers which will improve timing information), better resolving time for the Level 1 trigger decision (which will reduce the accidental trigger rate), and a new magnetic-field map which will improve the mass resolution both in the online trigger and in the offline analysis. However, it appears that reaching the sensitivity of 10^{-12} - 10^{-13} will require a new "next generation" experiment.

Appendix A
Performance of the Muon Rangefinder

The muon rangefinder^{55,56,57} is used to identify potential muon tracks by comparing the expected range to the measured range. The algorithm which determines the track's range is composed of two parts: in the first stage the tracks from the pattern recognition program are projected through the rangefinder and the simulated hit counters for each module are determined. Then real hits are compared to the simulated hits and assigned a momentum-dependent confidence level for being associated with the track. (The hit distributions and space-match distributions are shown in Fig. 36-43). The confidence level is taken from a look-up table which has six momentum bins: less than 1 GeV/c, 1-2 GeV/c, 2-3 GeV/c, 3-4 GeV/c, 4-5 GeV/c, and greater than 5 GeV/c. In the second stage of the algorithm, the hit information is used to construct rangefinder tracks. There are two requirements for a hit to be associated with a track: first a cut is placed on the space match probability between the simulated and real hit. This determines the "road" the hit must lie within, with widening towards the back of the rangefinder due to

multiple scattering effects. In addition, each hit is required to fall within one panel width of the previous module hit. This requirement helps to prevent a stray track from being picked up.

The efficiency of each rangefinder module was measured using minimum bias data for tracks which reach at least the fifth gap of the rangefinder. A module was considered efficient if it had a hit which satisfied both of the requirements described above. Table A.1 lists the efficiencies for all modules. (No efficiency is listed for modules in the last gap since there is no way to know whether they should have been hit).

The X and Y-view tracks are found independently and are considered to be stopped when there are two consecutive gaps without a hit. The last gap considered to be hit is nominally taken as the maximum of the X and Y-view. The average energy loss per gap was determined in a Monte-Carlo calculation, so the expected range of the track can be calculated by using the track momentum from the pattern recognition program. Hence a muon track can be identified by comparing the range measured by the rangefinder to the expected range (Last gap hit - Last gap expected to be hit). The efficiency for detecting muons is calculated using well identified muon tracks from the minimum bias data sample. The efficiency for muons from $K_L \rightarrow \mu e$ is lower due to the difference in the momentum

Table A.1
Efficiencies for Rangefinder Modules in %

Module	XL	XR	YL	YR	Statistical Error
1	91.0	91.0	92.9	89.7	0.2
2	95.6	96.2	94.0	95.7	0.2
3	95.6	95.8	94.8	95.7	0.2
4	96.3	94.2	96.0	95.3	0.2
5	96.3	95.3	93.2	94.3	0.2
6	95.1	93.6	94.2	92.9	0.2
7	93.1	92.9	92.8	93.9	0.3
8	93.2	90.6	91.2	91.9	0.4
9	90.8	90.9	90.0	89.2	0.5
10	87.6	88.7	87.2	88.3	0.6
11	84.3	83.3	83.1	83.1	1.0
12	95.7	78.1	96.0	73.6	2.4

spectrum (this correction was determined from the Monte-Carlo calculation of the muon momentum spectrum for $K_L \rightarrow \mu e$). Table A.2 gives the efficiency for detecting muon tracks for two choices of cuts and three different criteria for the "last gap hit".

The first criterion, "MAX (X,Y)", is that the last gap hit is the farthest downstream of the X and Y-view. If the projected track exits the rangefinder, the last expected gap is taken to be the exit point. However, it is possible for the actual track to exit the rangefinder

Table A.2

Muon Identification Efficiency of Rangefinder in %

<u>Criteria</u>	cut $n \leq -4$	cut $n \leq -2$
MAX (X,Y)	98.71 \pm 0.07	95.42 \pm 0.38
MAX (X,Y) PASS EDGE HITS	99.01 \pm 0.07	96.51 \pm 0.18
MIN (X,Y)	94.22 \pm 0.22	84.05 \pm 0.33

farther upstream due to multiple scattering; thus the muon identification efficiency can be increased by passing events for which the last hit is on an edge panel. (This is the second criterion, "MAX (X,Y), PASS EDGE HITS"). However, this criterion reduces the pion rejection efficiency of the rangefinder.

Accidental hits can cause the rangefinder track to extend too far; thus the pion rejection efficiency can be improved by cutting on the minimum last gap hit of the X and Y view. (This is the third criterion, "MIN (X,Y)"). However, this criterion also reduces the muon efficiency of the rangefinder. For the offline analysis, the stop-gap criterion was the maximum of the X and Y view, and the cut of $n \leq -4$ was chosen.

REFERENCES

1. Particle Data Group, Phys. Lett. 170 B (1986).
2. A.R. Clark, et al., Phys. Rev. Lett. 26, 1667 (1971).
3. R.D. Cousins, et al., Phys. Rev. D38 Rapid Communications, 2914 (1988).
4. H.B. Greenlee, et al., Phys. Rev. Lett. 60, 893 (1988).
5. S.F. Schaffaer, Phys. Rev. D39, 990 (1989).
6. T. Inagaki, KEK Preprint 89-12 (1989).
7. S.L. Glashow, Nucl. Phys. 22, 579 (1961).
8. A. Salam and J.C. Ward, Phys. Lett. 13, 168 (1964).
9. S. Weinberg, Phys. Rev. Lett. 19, 1264 (1967).
10. A. Barroso, et al., Phys. Lett. 134B, 123 (1984).
11. R.D. Bolton, et al., Phys. Rev. Lett. 56, 2461 (1986).
12. B.W. Lee and R.E. Shrock, Phys. Rev. D16, 1444 (1977).
13. P. Sikivie, Phys. Lett. 65B, 141 (1976).
14. A.B. Lahanas and C.E. Vayonakis, Phys. Rev. D19, 2158 (1979).
15. R.N. Cahn and H. Harari, Nucl. Phys. B176, 135 (1980).
16. U. Bellgardt, et al., Nucl. Phys. B299, 1 (1988).
17. P. Rehak, BNL Workshop on Rare K Decays and CP Violation, August 25-27, 1988.
18. S. Ahmad, et al., Phys. Rev. Lett. 59, 970 (1987).
19. O. Shanker, Phys. Rev. D20, 1608 (1979).

20. L. Susskind, Phys. Rev. D20, 2619 (1979).
21. S. Dimopoulos and L. Susskind, Nucl. Phys. B155, 237 (1979).
22. A. Masiero, et al., Phys. Lett. 115B, 229 (1982).
23. J. Ellis, et al., Nucl. Phys. B182, 529 (1981).
24. M.A.B. Beg, Phys. Lett. 124B, 403 (1983).
25. S. Dimopoulos and J. Ellis, Nucl. Phys. B182, 505 (1981).
26. O. Shanker, Nucl. Phys. B206, 253 (1982).
27. R.E. Marshak and R.N. Mohapatra, Phys. Lett. 91B, 222 (1980).
28. R.N. Mohapatra and J.C. Pati, Phys. Rev. D11, 566 (1975).
29. G. Beall, et al., Phys. Rev. Lett. 48, 848 (1982).
30. W. Hou and A. Soni, Phys. Rev. Lett. 54, 2083 (1985).
31. J.C. Pati and A. Salam, Phys. Rev. D8, 1240 (1973).
32. J.C. Pati and A. Salam, Phys. Rev. D10, 275 (1974).
33. S. Dimopoulos, et al., Nucl. Phys. B182, 77 (1981).
34. N.G. Deshpande and R.J. Johnson, Phys. Rev. D27, 1193 (1983).
35. R. Barbieri, et al., Phys. Lett. 96B, 63 (1980).
36. S.J. Brodsky, et al., Phys. Rev. D22, 2236 (1980).
37. J.C. Pati, et al., Phys. Lett. 59B, 265 (1975).
38. J.C. Pati, Phys. Rev. D30, 1144 (1984).
39. O.W. Greenberg, et al., Phys. Lett. 148B, 465 (1984).
40. J.C. Pati, Phys. Lett. B144, 375 (1984).

41. J.C. Pati and H. Stremnitzer, Phys. Lett. B172, 441 (1986).
42. J. Ellis and D.V. Nanopoulos, Phys. Lett. 110B, 44 (1982).
43. J.C. Romao, et al., Nucl. Phys. B250, 295 (1985).
44. E. Witten, Nucl. Phys. B258, 75 (1985).
45. B.A. Cambell, et al., Int. Jour. of Mod. Phys. A2, 831 (1987).
46. P. Skubic, et al., Phys. Rev. D18, 3115 (1978).
47. R.T. Edwards, et al., Phys. Rev. D18, 76 (1978).
48. Y. Tsai, Rev. of Mod. Phys. 46, 4 (1974).
49. Y. Hoshi, et al., Nucl. Inst. and Meth. A236, 82 (1985).
50. R.D. Cousins, et al., SLAC-PUB-4763 (1988).
51. K.A. Biery, et al., SLAC-PUB-4780 (1988).
52. P.F. Kunz, et al., SLAC-PUB-3332 (1984).
53. T. Shibata, Nucl. Phys. A408, 525 (1983).
54. A. Carroll, Phys. Lett. 80B, 319 (1979).
55. J. Frank, et al., IEEE Trans. Nucl. Sci. 36, 79 (1989).
56. C. J. Kenney, et al., IEEE Trans. Nucl. Sci. 36, 74 (1989).
57. D.M. Lee, et al., Nucl. Instr. and Meth. in Phys. Res. A256, 329 (1987).

FIGURE CAPTIONS

- Fig. 1 Diagram responsible for $K^0-\bar{K}^0$ mixing in the Standard Model.
- Fig. 2 Diagram mediating $K_L \rightarrow \mu e$ in a model with a massive neutral lepton L_0 .
- Fig. 3 Contribution to $K^0-\bar{K}^0$ mixing, via a new boson H , in a horizontal symmetry model.
- Fig. 4 Contribution to $K_L \rightarrow \mu e$, via a new boson H , in a horizontal symmetry model.
- Fig. 5 Diagram mediating $K_L \rightarrow \mu e$ via an ETC gauge boson E in a technicolor model.
- Fig. 6 Diagram mediating $K_L \rightarrow \mu e$ via a pseudo-goldstone boson P in an ETC model.
- Fig. 7 Diagram mediating $K_L \rightarrow \mu e$ via a pseudo-scaler leptoquark P in an ETC model.
- Fig. 8 Diagram mediating $K_L \rightarrow \mu e$ via a right-handed gauge boson W_R in a left-right symmetry model.
- Fig. 9 Diagram mediating $K_L \rightarrow \mu e$ via a $SU_C(4)$ Pati-Salam boson P .
- Fig. 10 Diagram mediating $K_L \rightarrow \mu e$ via flavon and chromon transitions in a composite model.
- Fig. 11 Diagram mediating $K_L \rightarrow \mu e$ via supersymmetric particles in a supersymmetry model.
- Fig. 12 Experimental apparatus in the AGS B5 beam line.
- Fig. 13 Drift chamber wire geometry.
- Fig. 14 Online data acquisition program block diagram.
- Fig. 15 Level 1 trigger block diagram for beam left side.

- Fig. 16 Kaon momentum spectrum for data and Monte-Carlo (in GeV/c).
- Fig. 17 Charge-track momentum spectrum for data and Monte-Carlo (in GeV/c).
- Fig. 18 Momentum balance of tracks for data and Monte-Carlo.
- Fig. 19 Distance of closest approach (DOCA) of tracks at vertex ($\times 10^{-3}$ meters).
- Fig. 20 Difference in track momentum between upstream and downstream spectrometer.
- Fig. 21 Energy E deposited in lead glass divided by track momentum p for well identified pions and electrons.
- Fig. 22 Difference between last rangefinder gap with a track associated hit and the expected last gap to be hit for well identified pions and muons.
- Fig. 23 Z position of reconstructed vertex for data and Monte-Carlo (in meters).
- Fig. 24 X position divided by Z position at the vertex for data and Monte-Carlo.
- Fig. 25 Y position divided by Z position at the vertex for data and Monte-Carlo.
- Fig. 26 X position of track at the vacuum window for data and Monte-Carlo (in meters).
- Fig. 27 Vertex χ^2 distribution for data and Monte-Carlo.
- Fig. 28 X-view track χ^2 distribution for data and Monte-Carlo.
- Fig. 29 Y-view track χ^2 distribution for data and Monte-Carlo.
- Fig. 30 Invariant mass calculation vs. the square of the collinearity angle for minimum bias data calculated with $\pi \pi$ mass.

- Fig. 31 Square of the collinearity angle for the minimum bias data.
- Fig. 32 Invariant mass calculation for minimum bias data calculated with $\pi\pi$ mass (and collinearity less than 1 mrad).
- Fig. 33 Invariant mass calculation vs. the square of the collinearity angle for μe data calculated with the μe mass.
- Fig. 34 Square of the collinearity angle for μe data.
- Fig. 35 Invariant mass calculation for μe data calculated with the μe mass (and collinearity less than 1 mrad).
- Fig. 36 Rangefinder hit distribution, binned by individual panels, for module 3LX.
- Fig. 37 Rangefinder hit distribution, binned by individual panels, for module 9LX. Neutral beam interactions cause an enhancement in the first bin (beam edge) relative to Fig. 36.
- Fig. 38 Rangefinder hit distributions, binned by individual panels, for module 3LY.
- Fig. 39 Rangefinder hit distributions, binned by individual panels, for module 9LY.
- Fig. 40 Difference between projected and actual hit positions, binned by individual panels, for module 3LX.
- Fig. 41 Difference between projected and actual hit positions, binned by individual panels, for module 9LX. The broadening (relative to Fig. 40) is due to multiple-scattering effects.
- Fig. 42 Difference between projected and actual hit positions, binned by individual panels, for module 3LY.
- Fig. 43 Difference between projected and actual hit positions, binned by individual panels, for module 9LY. The broadening (relative to Fig. 42) is due to multiple-scattering effects.

Figure 1

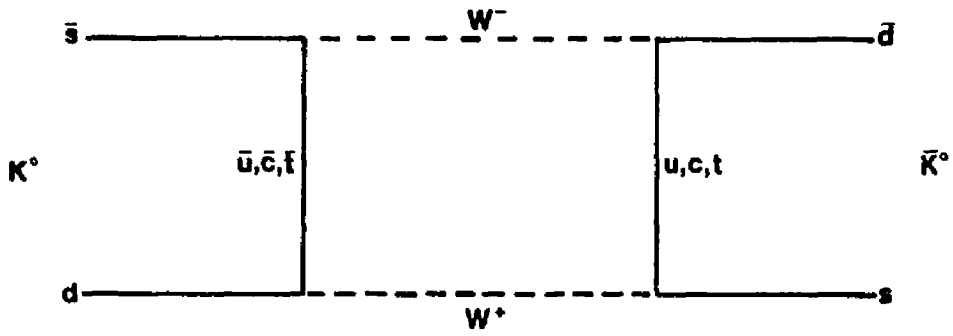


Figure 2

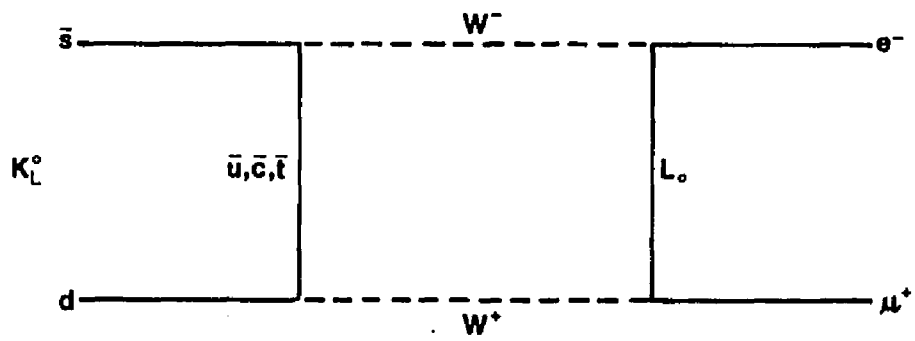


Figure 3

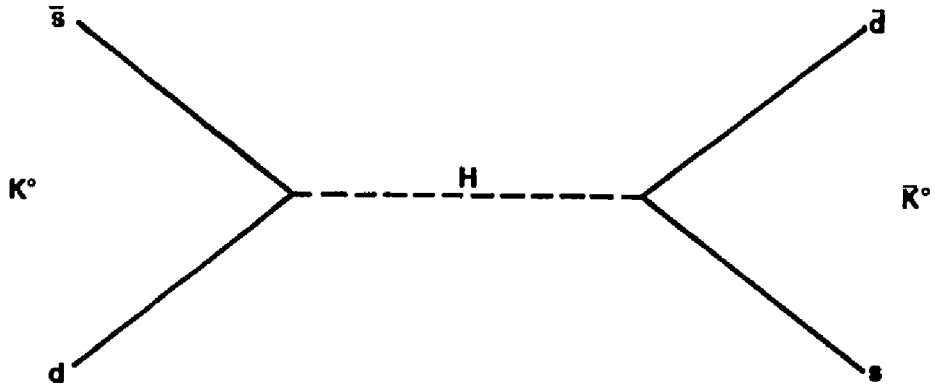


Figure 4

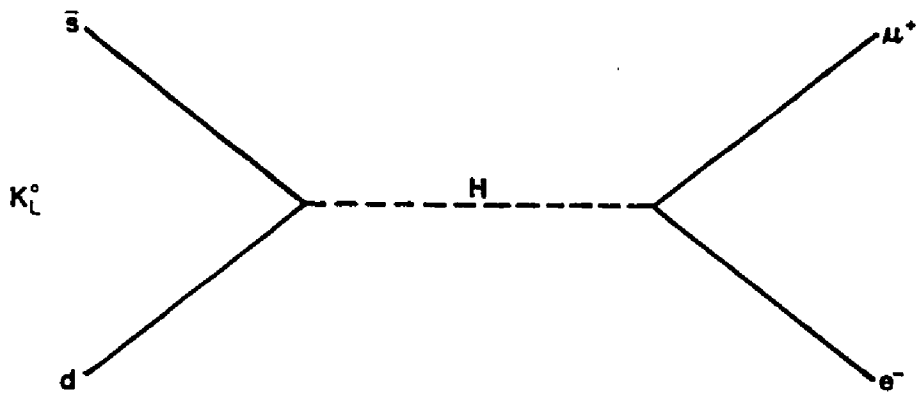


Figure 5

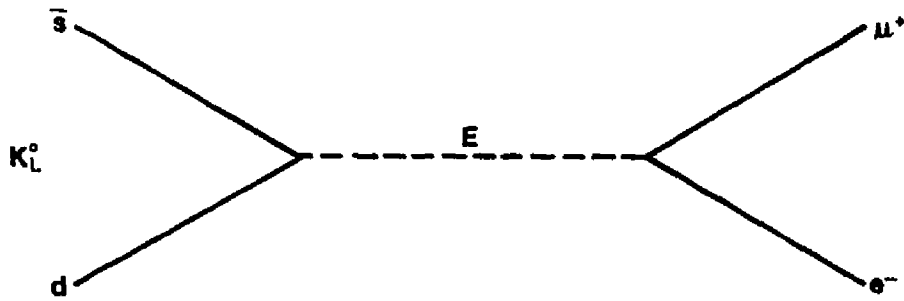


Figure 6

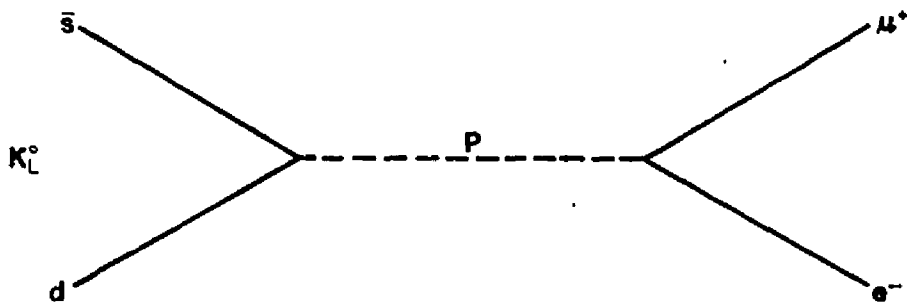


Figure 7

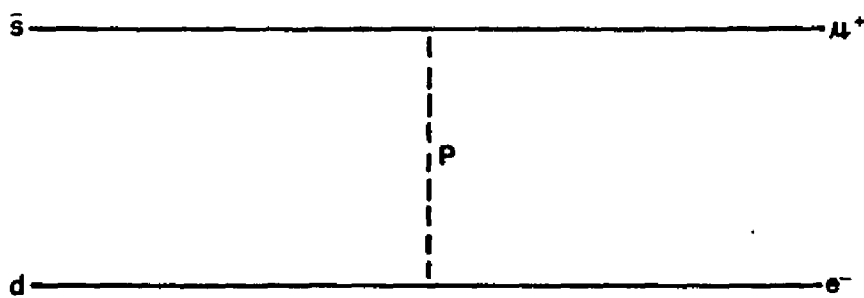


Figure 8

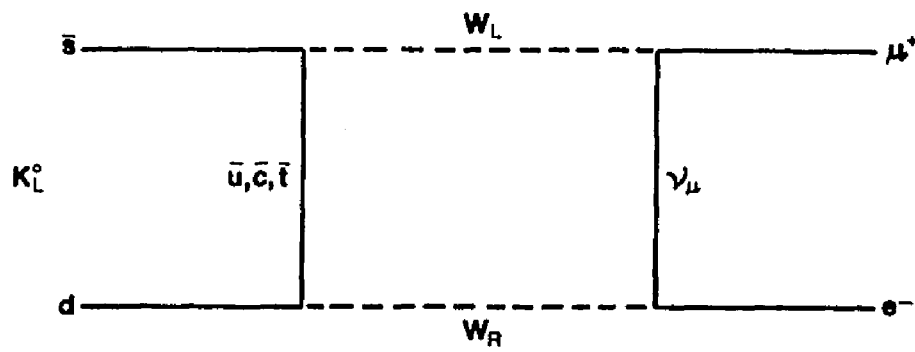


Figure 9

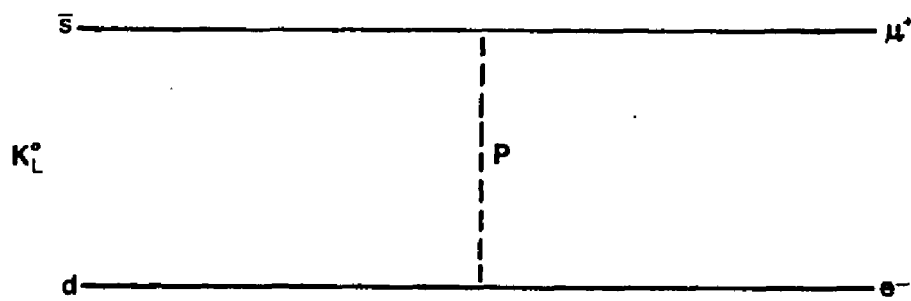


Figure 10

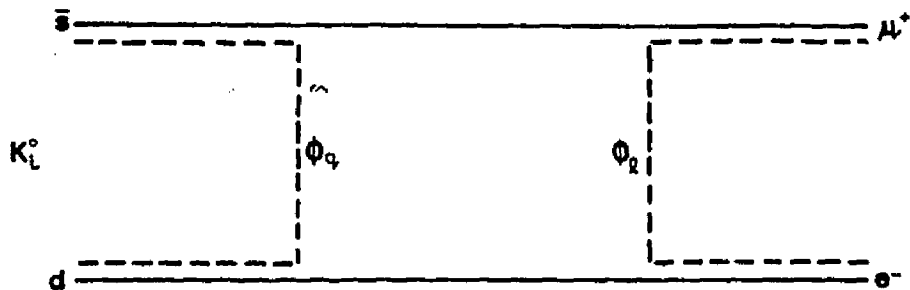


Figure 11

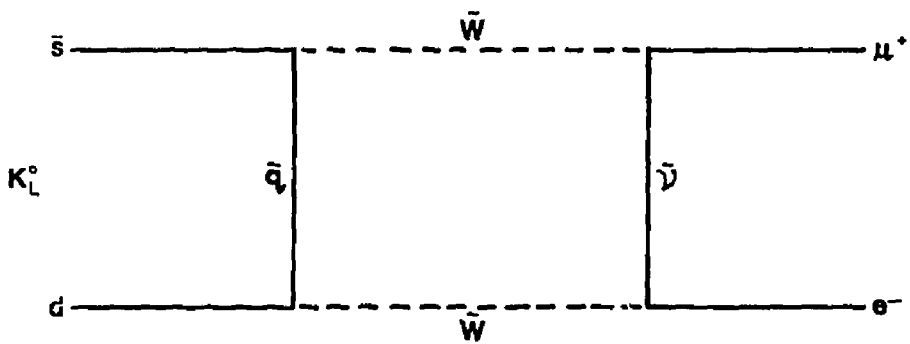


Figure 12

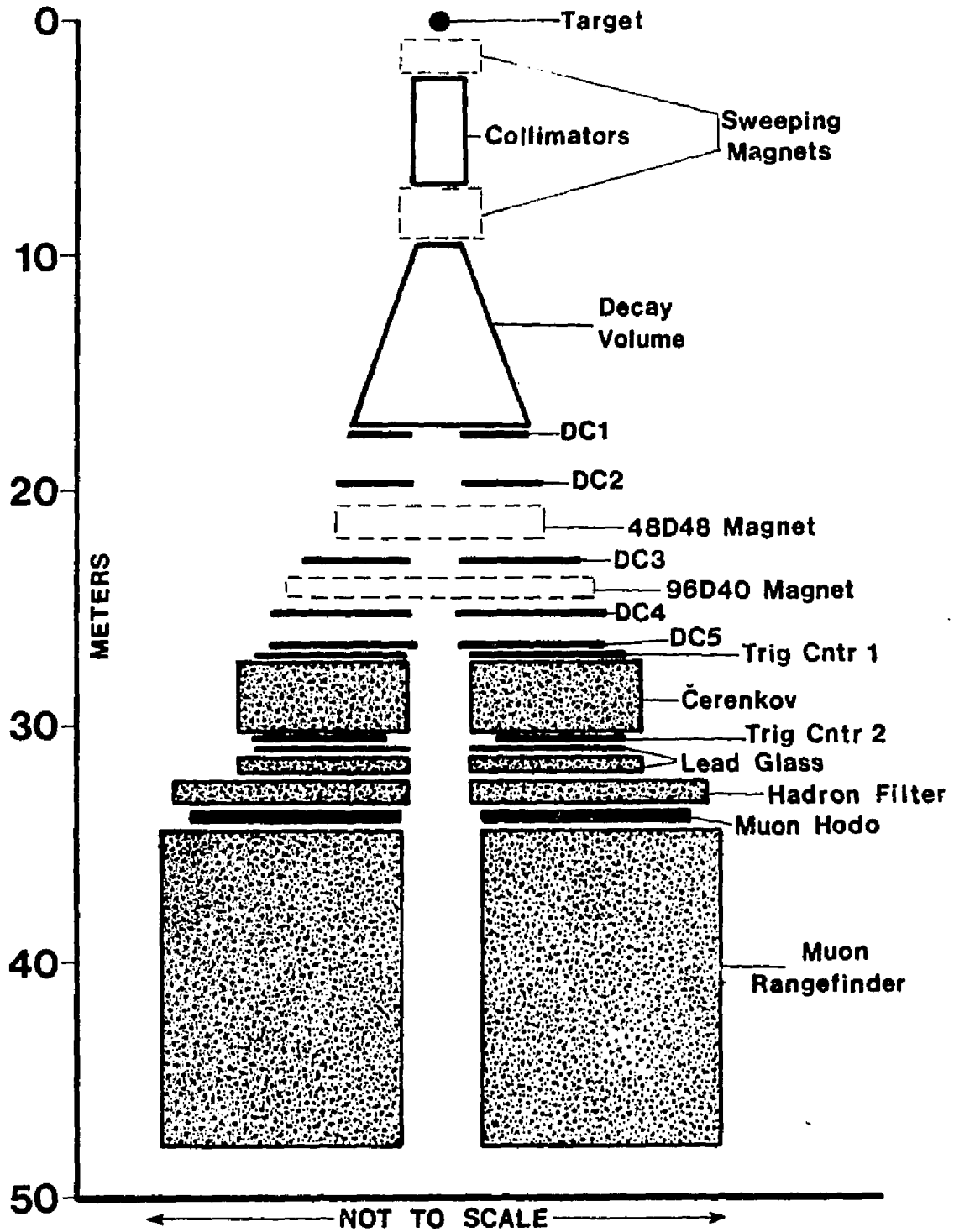
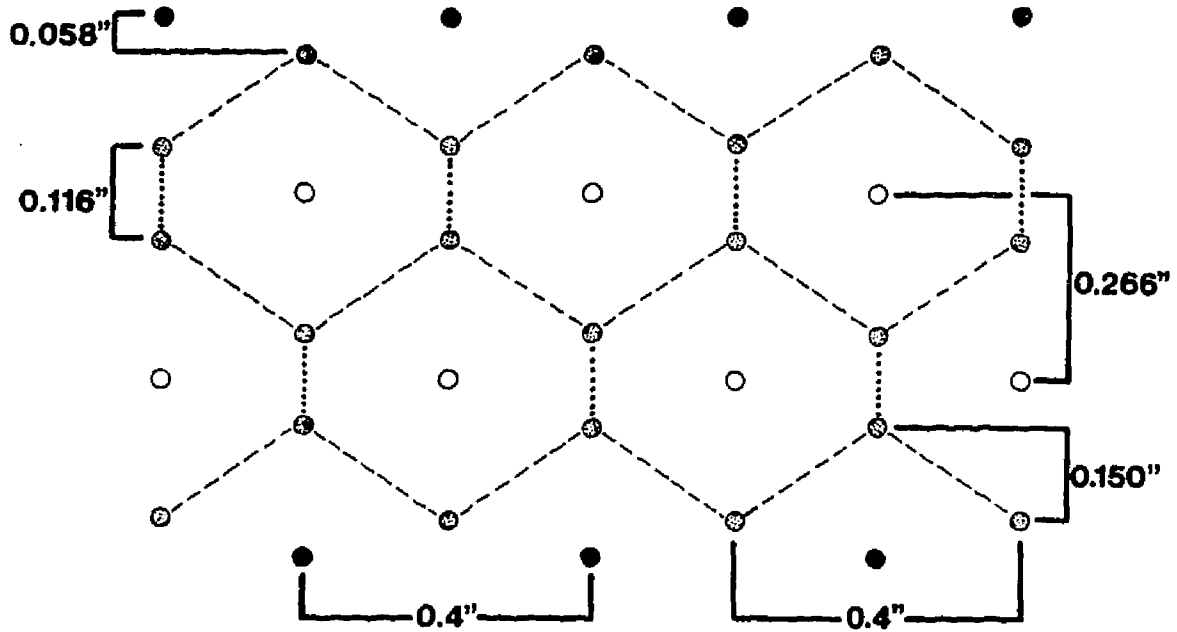


Figure 13



● **GUARD WIRE**

● **FIELD WIRE**

○ **SENSE WIRE**

Figure 14

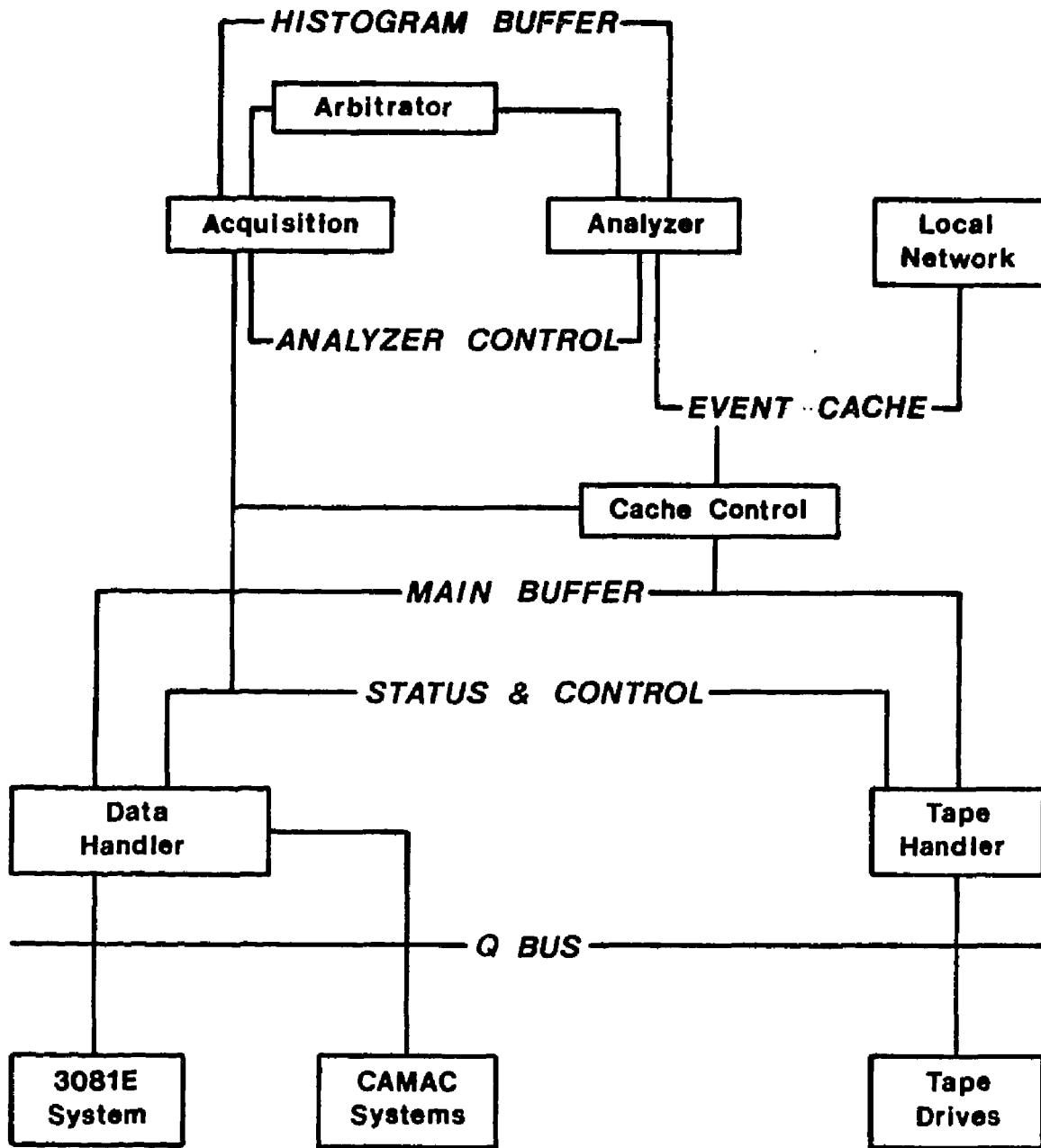


Figure 15

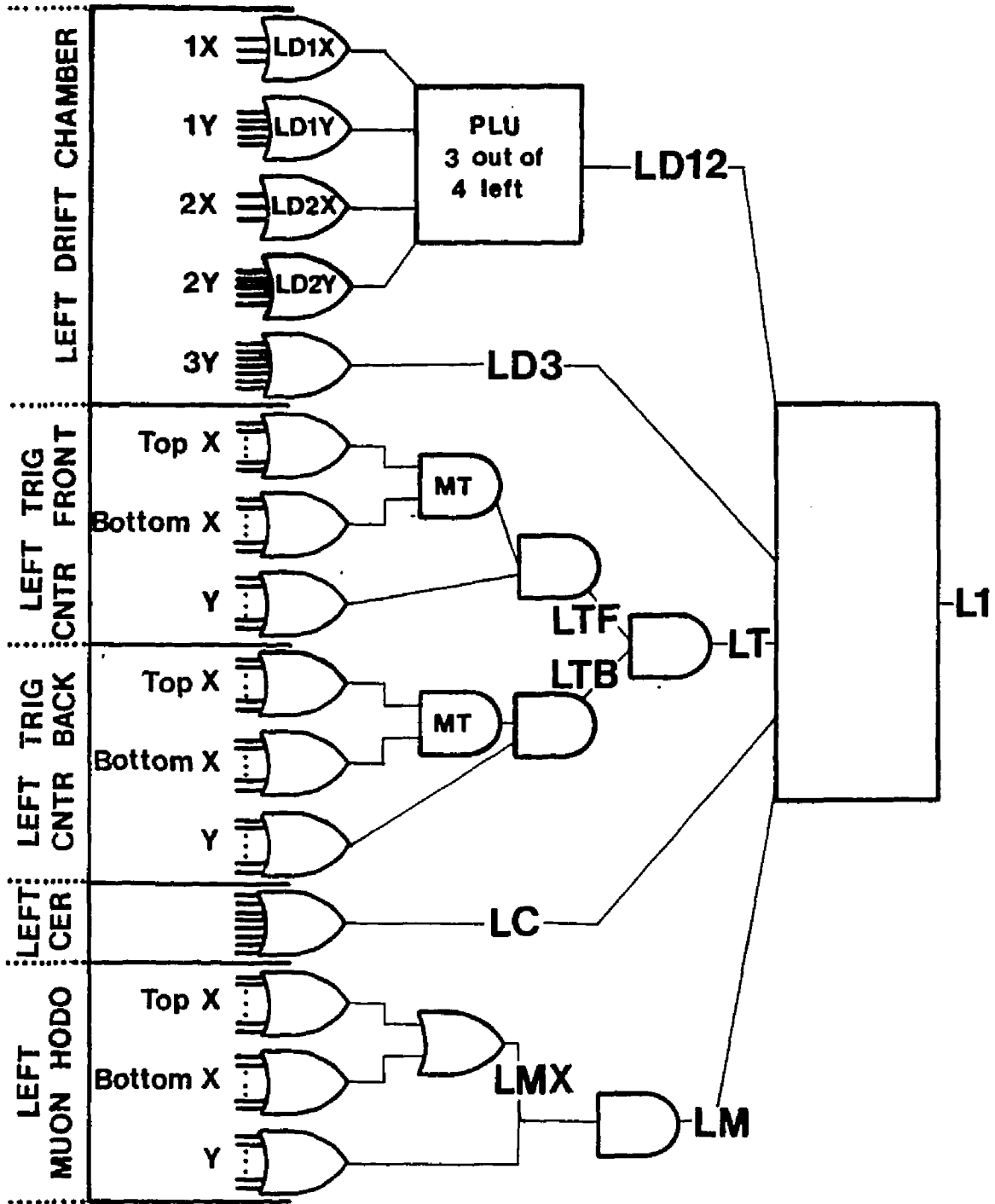


Figure 16

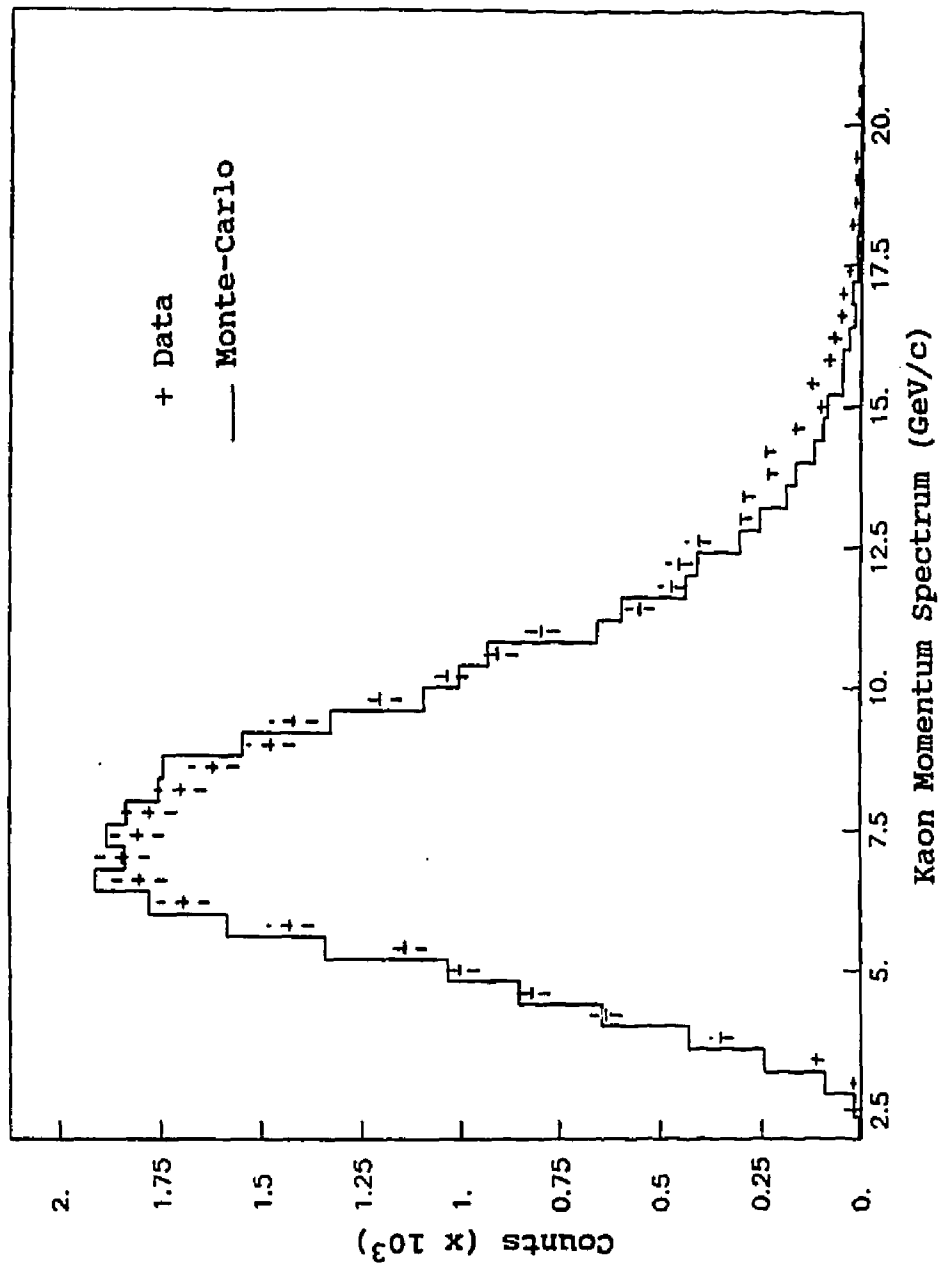


Figure 17

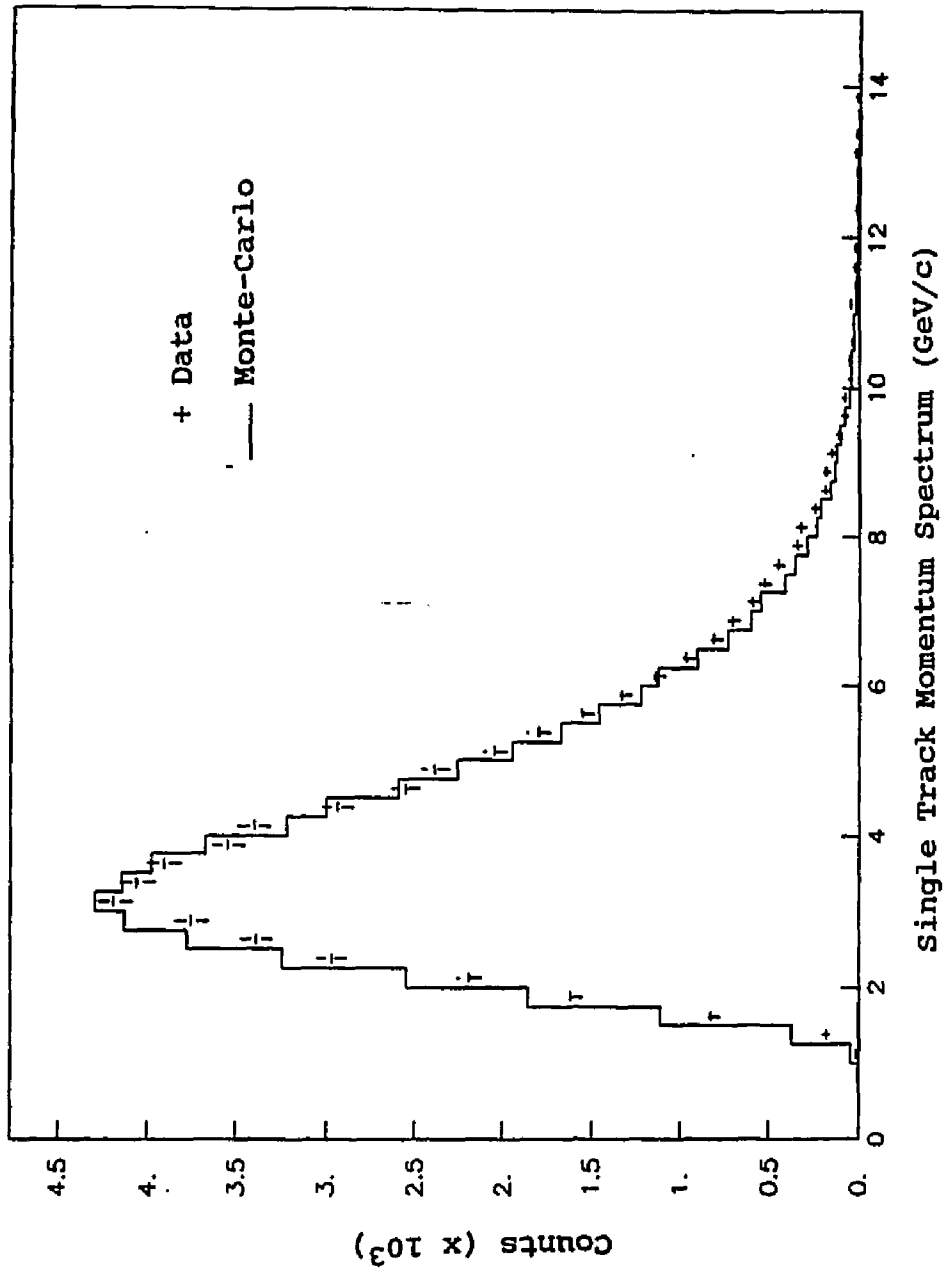


Figure 18

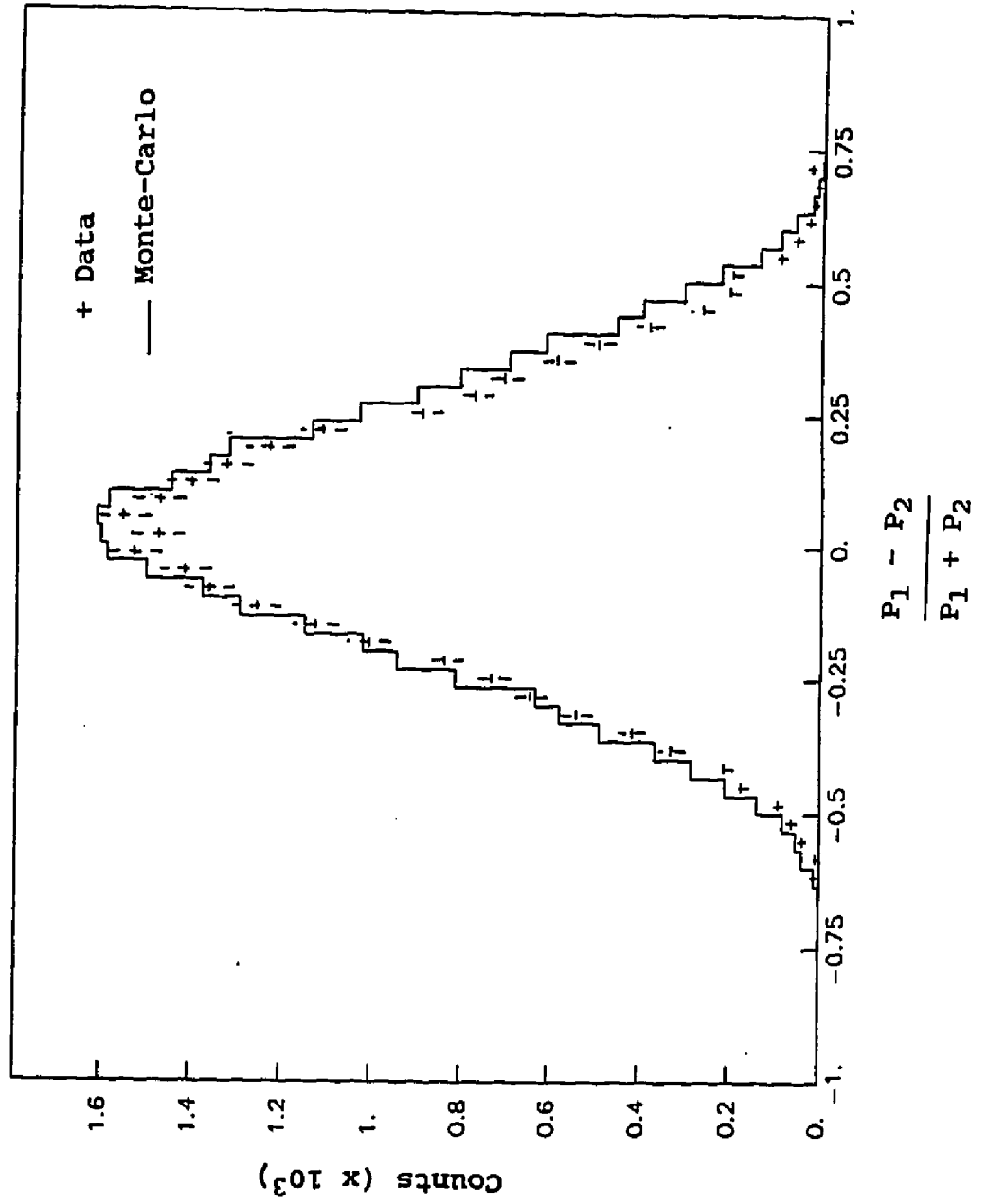


Figure 19

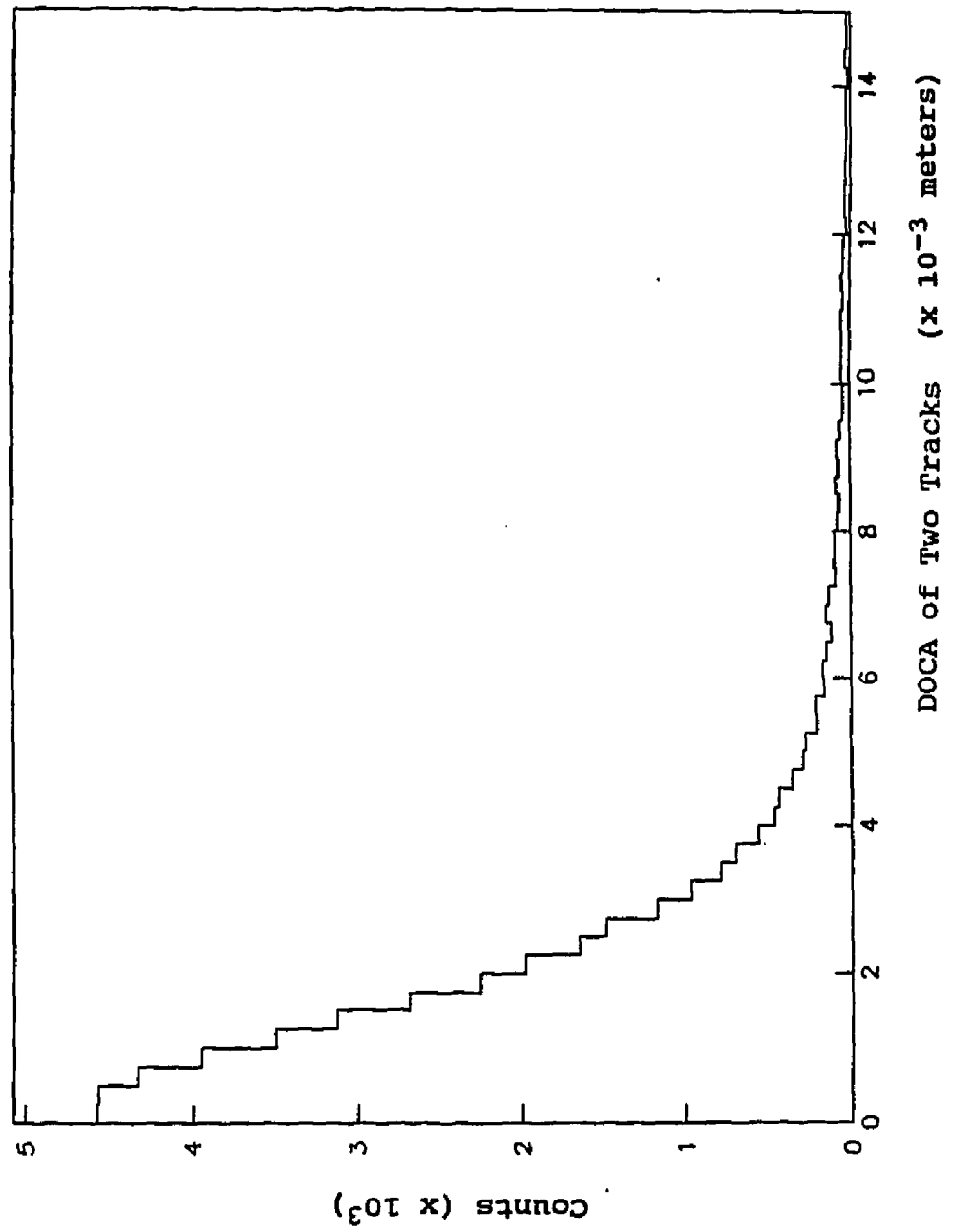


Figure 20

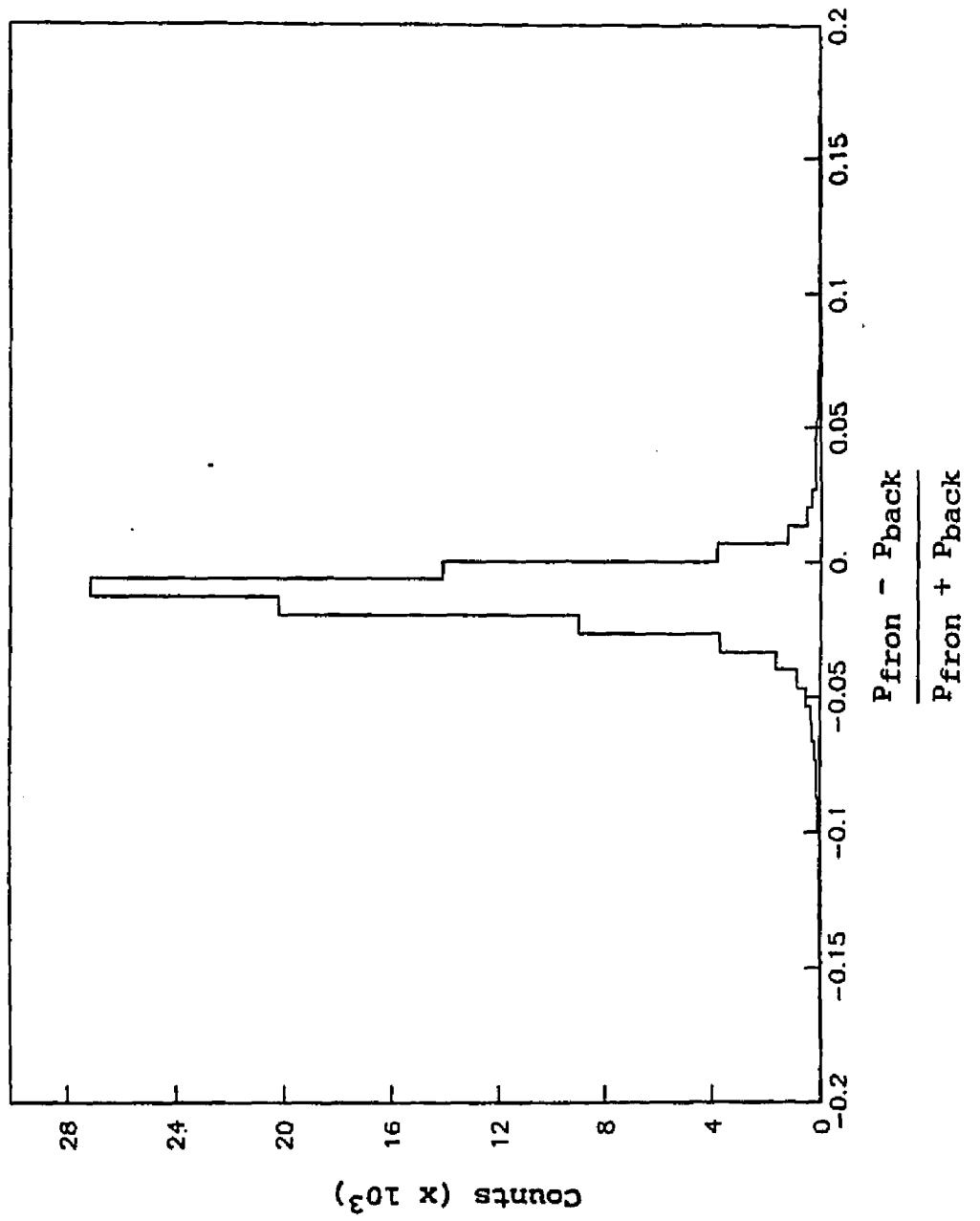


Figure 21

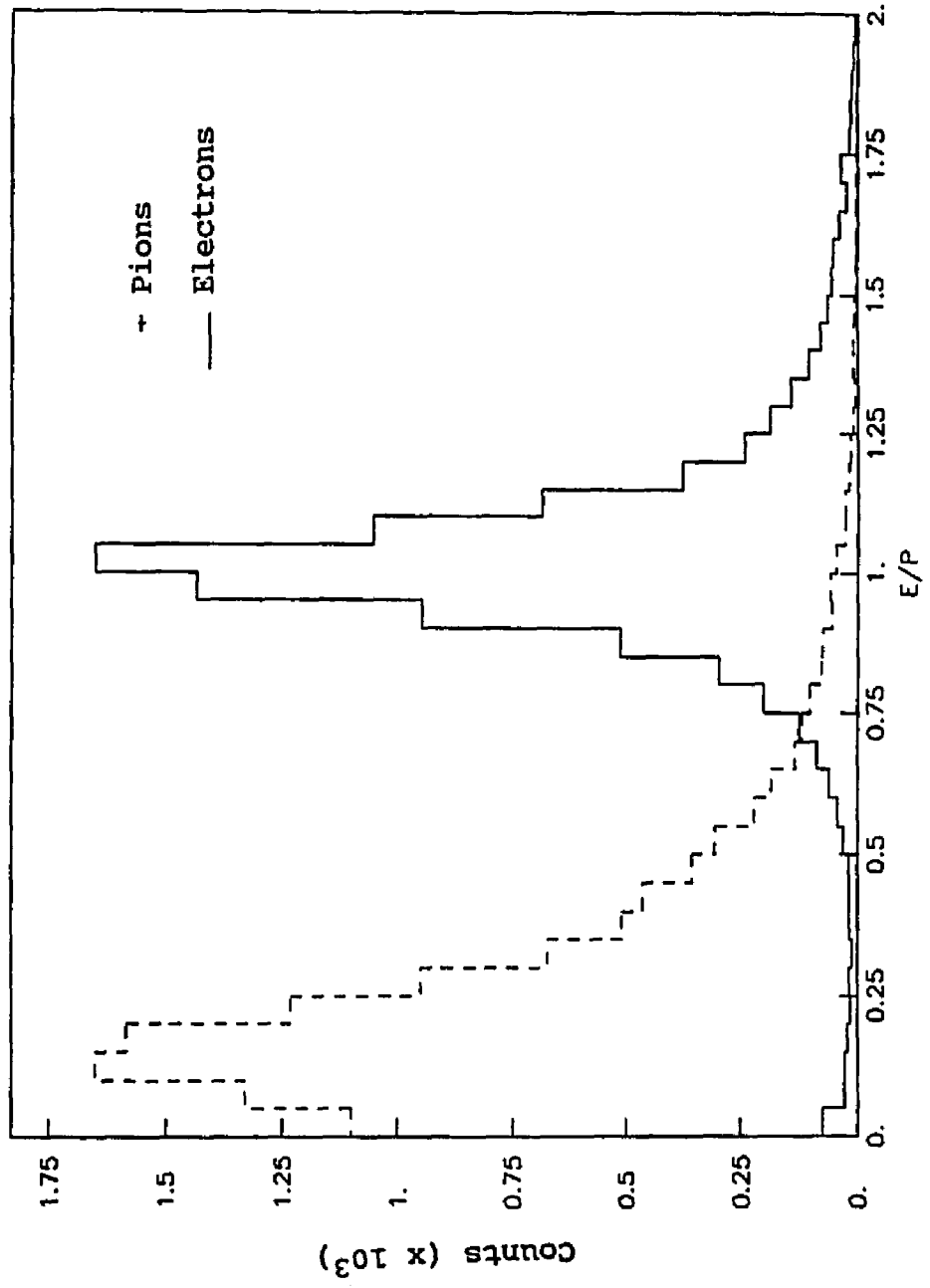


Figure 22

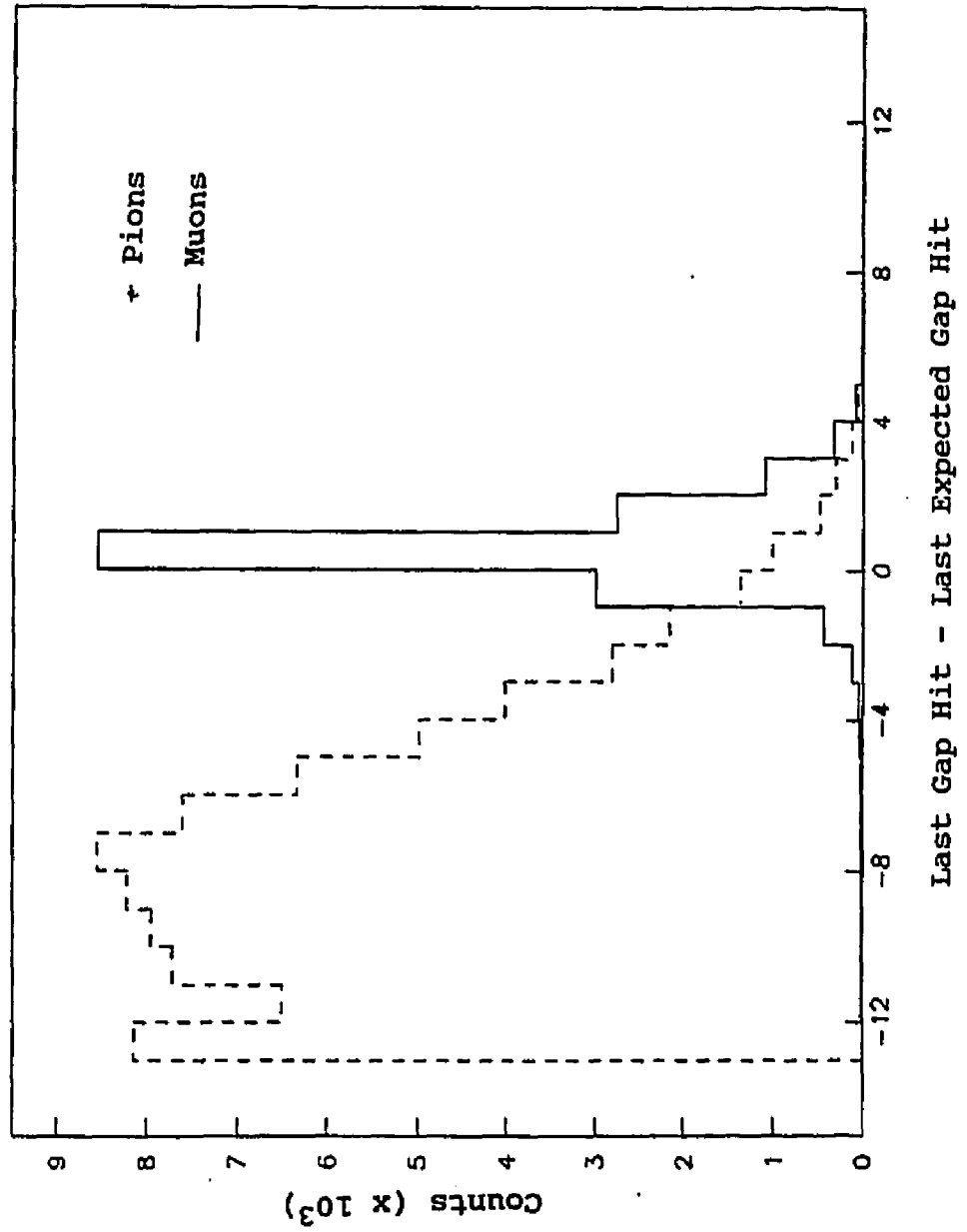


Figure 23

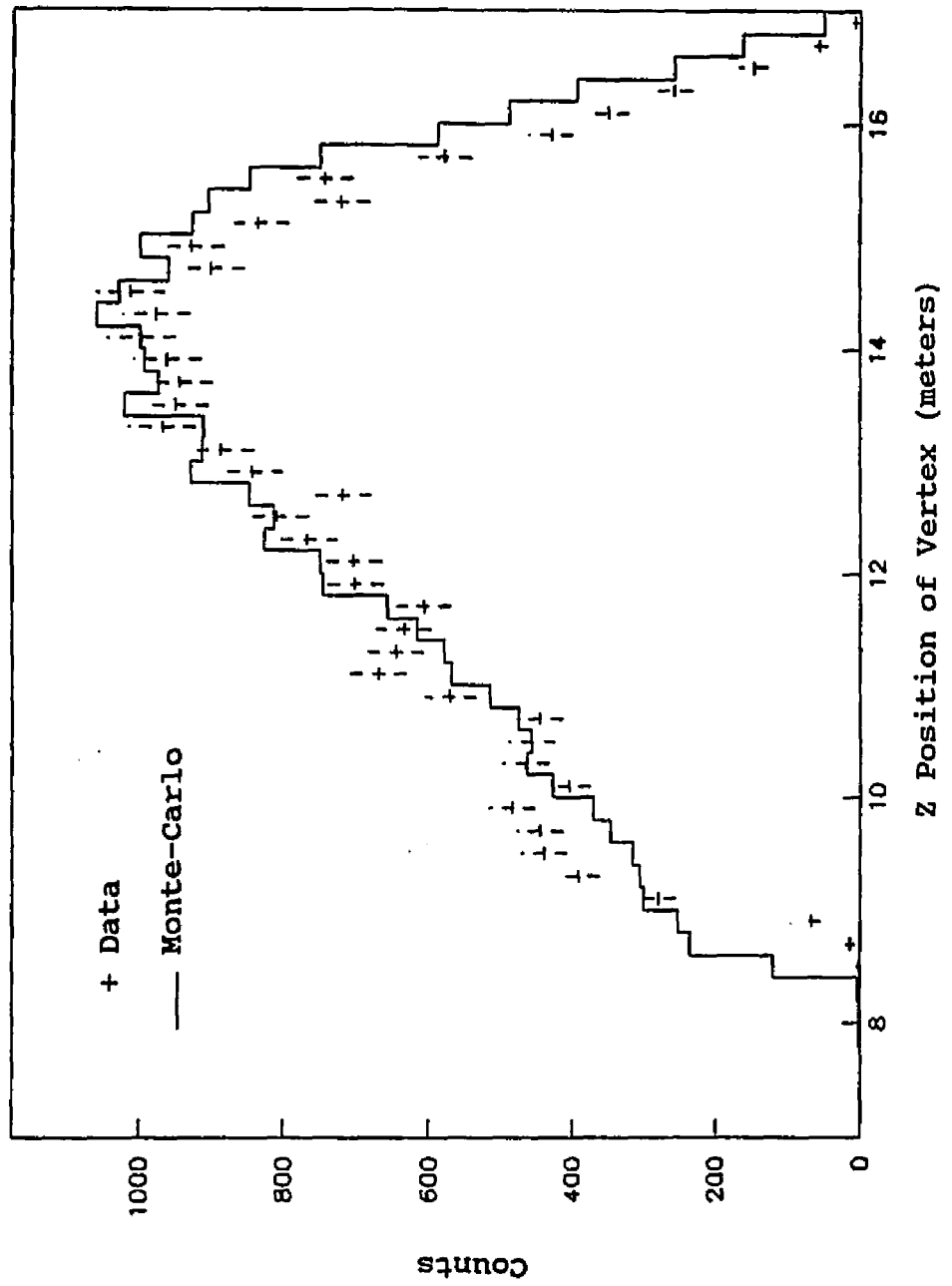


Figure 24

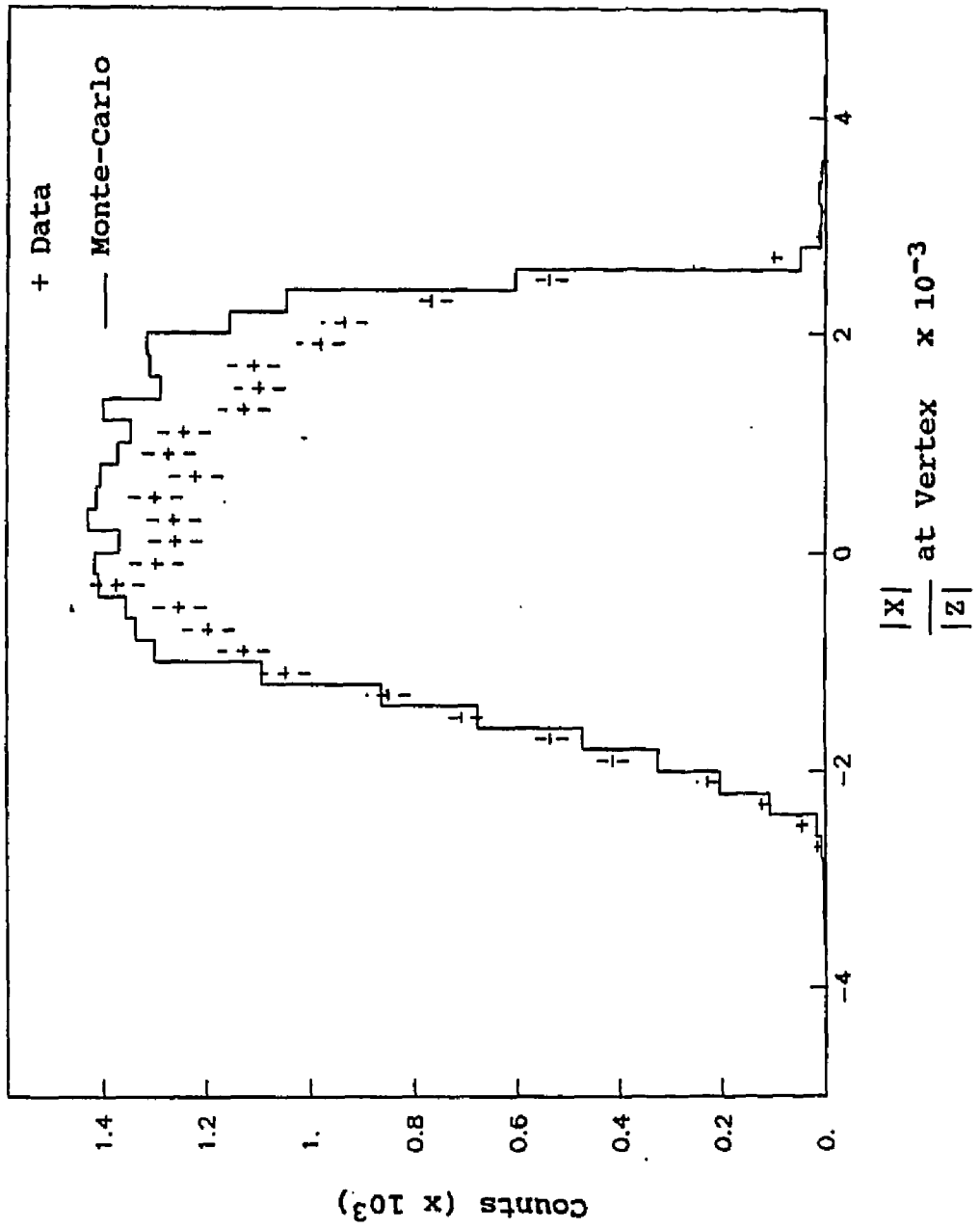


Figure 25

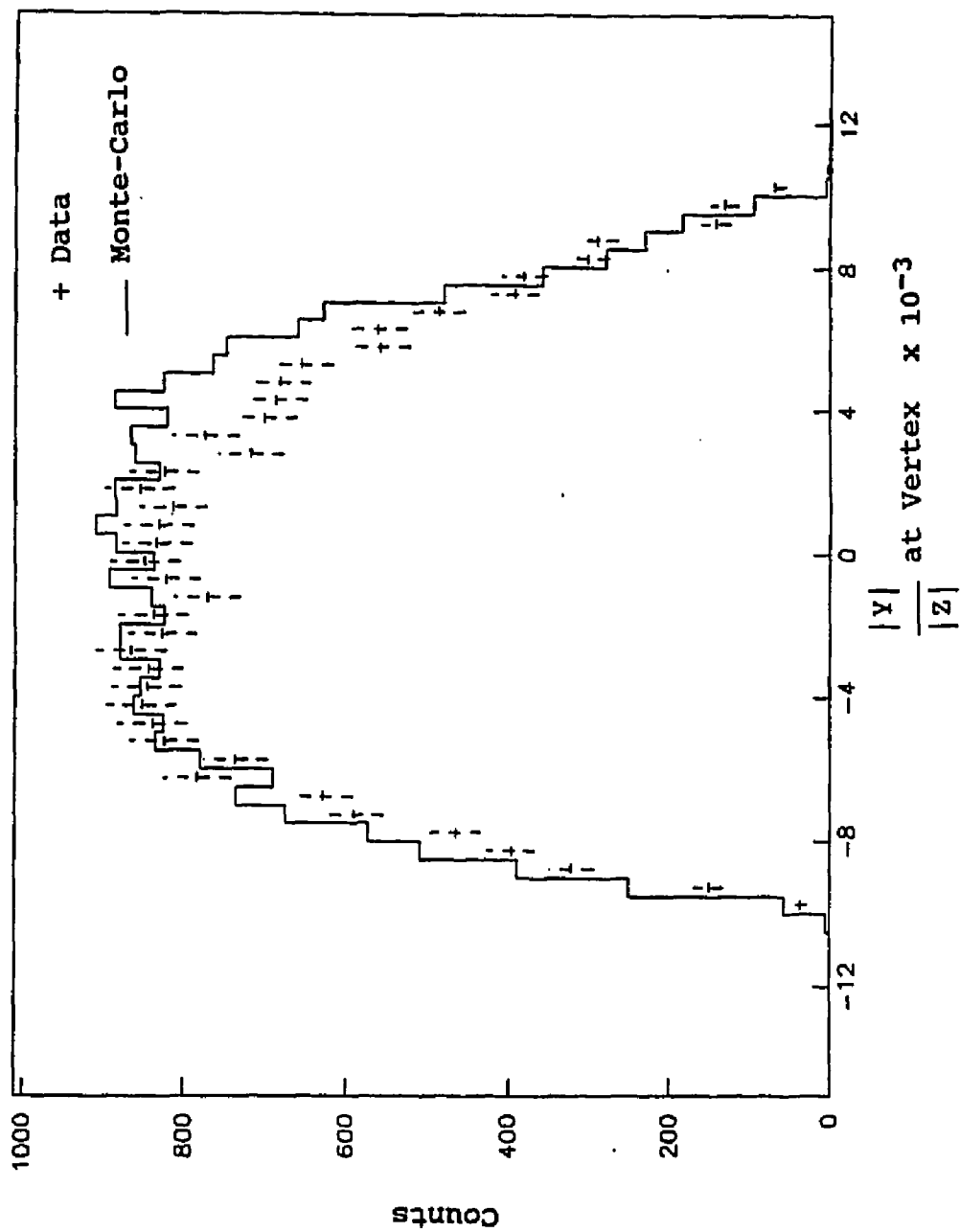


Figure 26

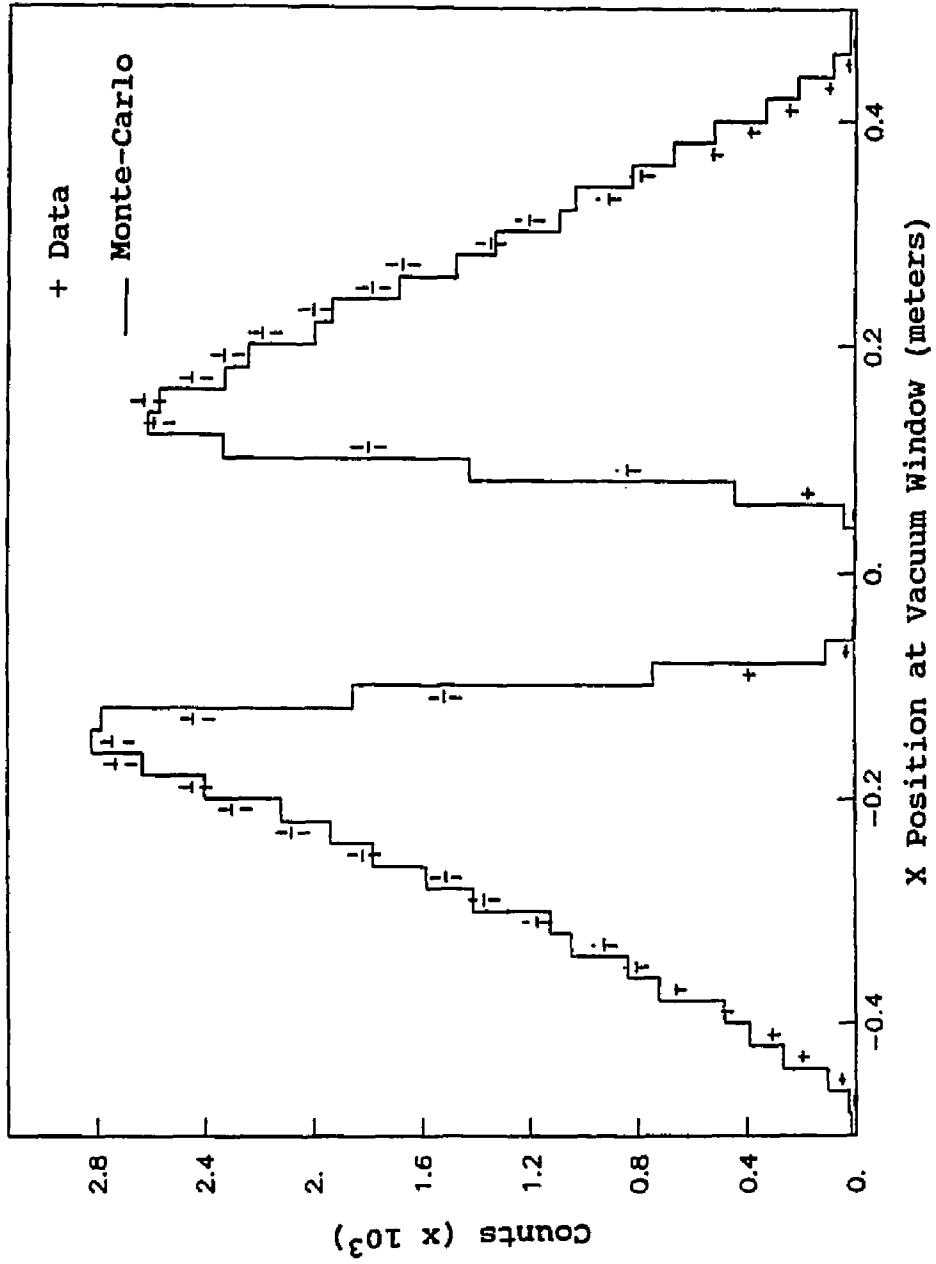


Figure 27

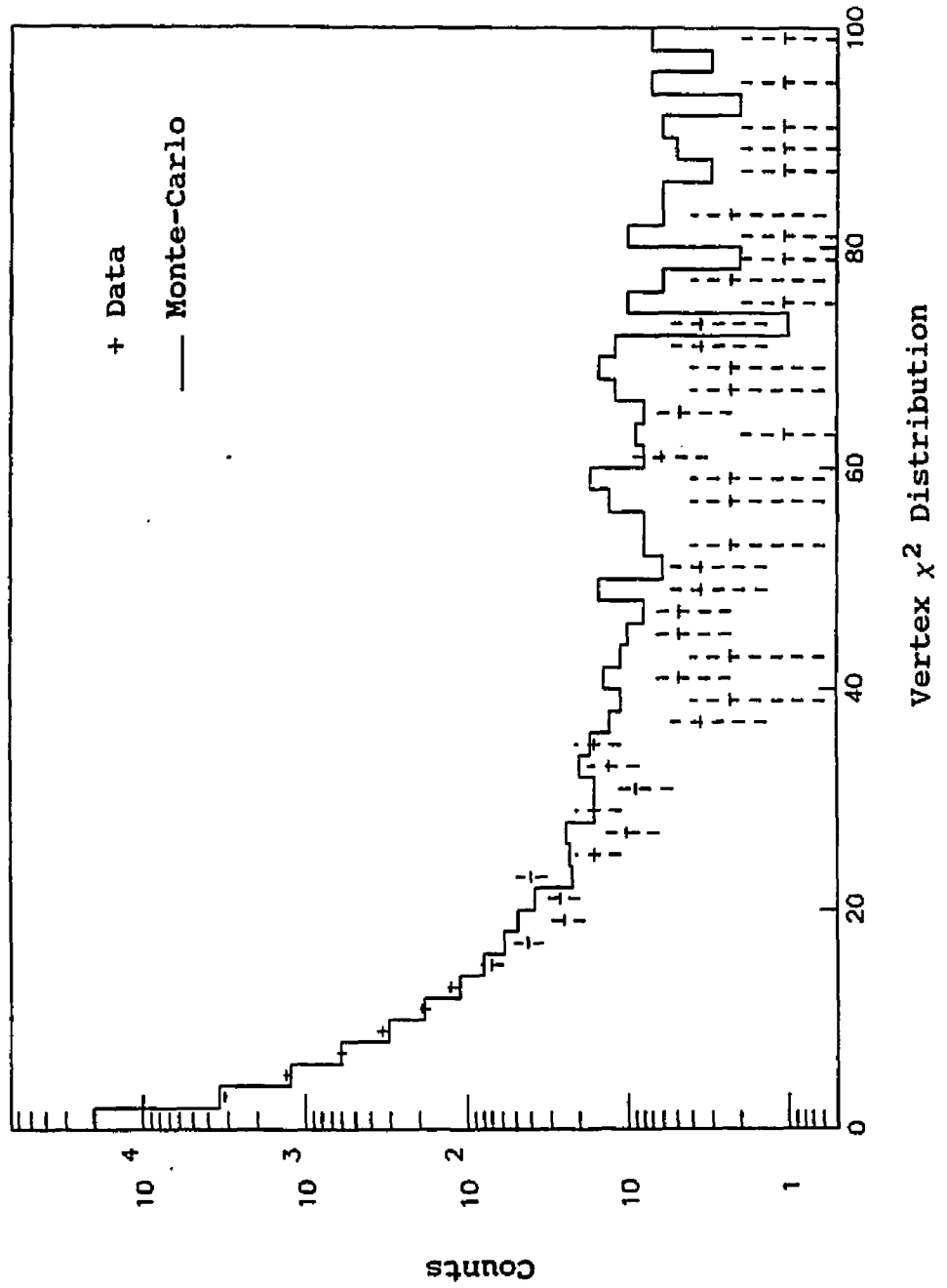


Figure 28

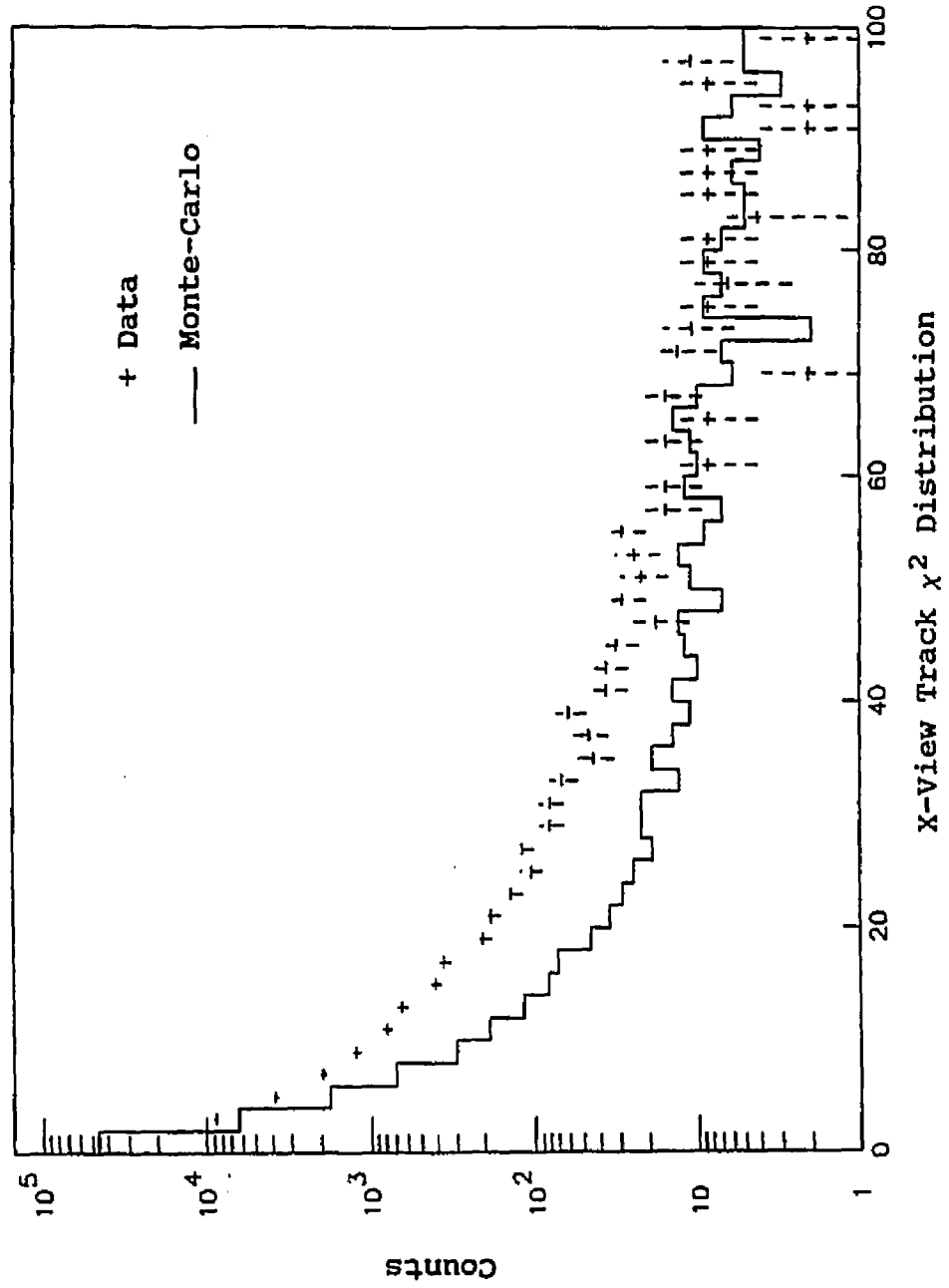


Figure 29

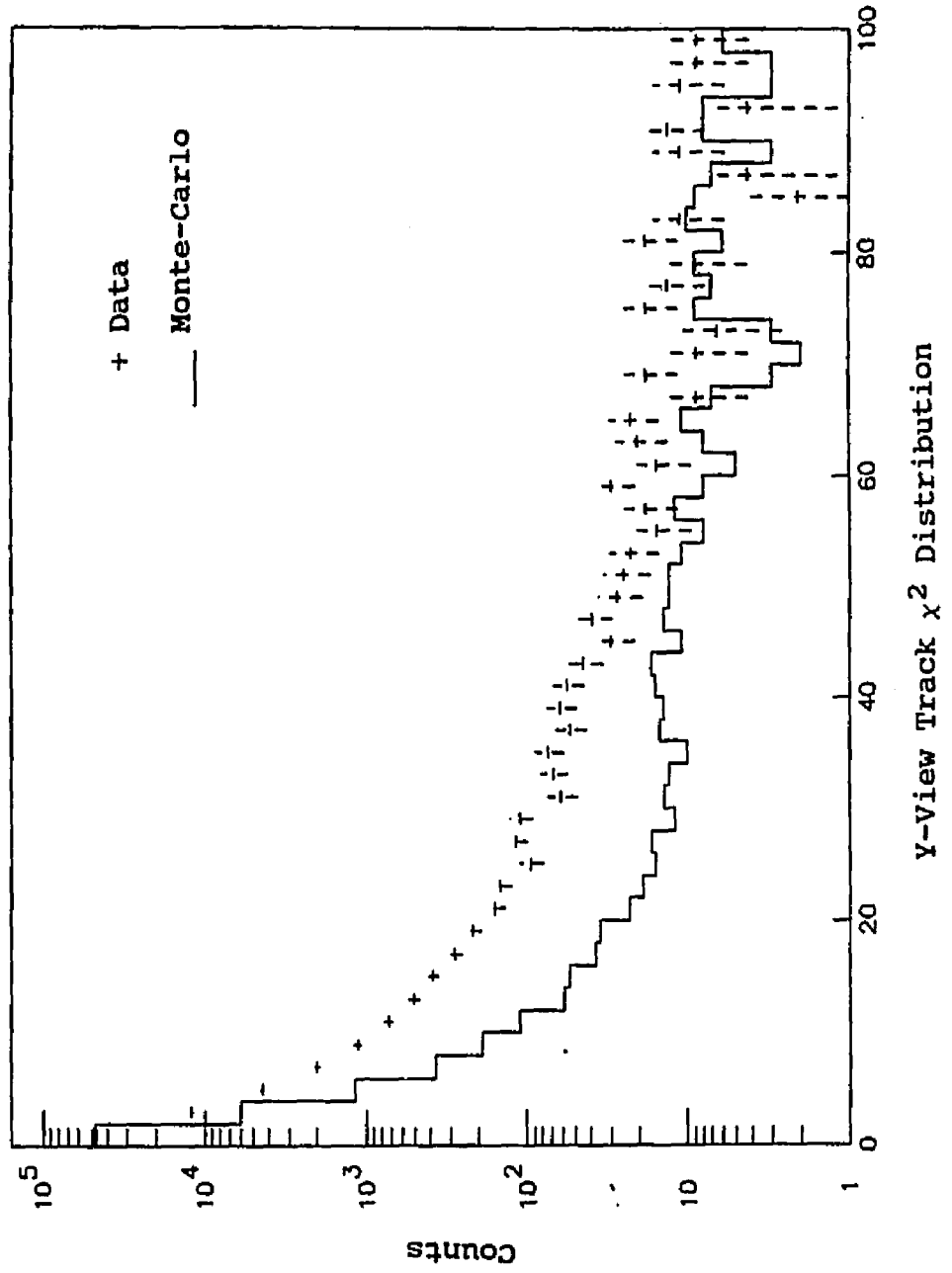


Figure 30

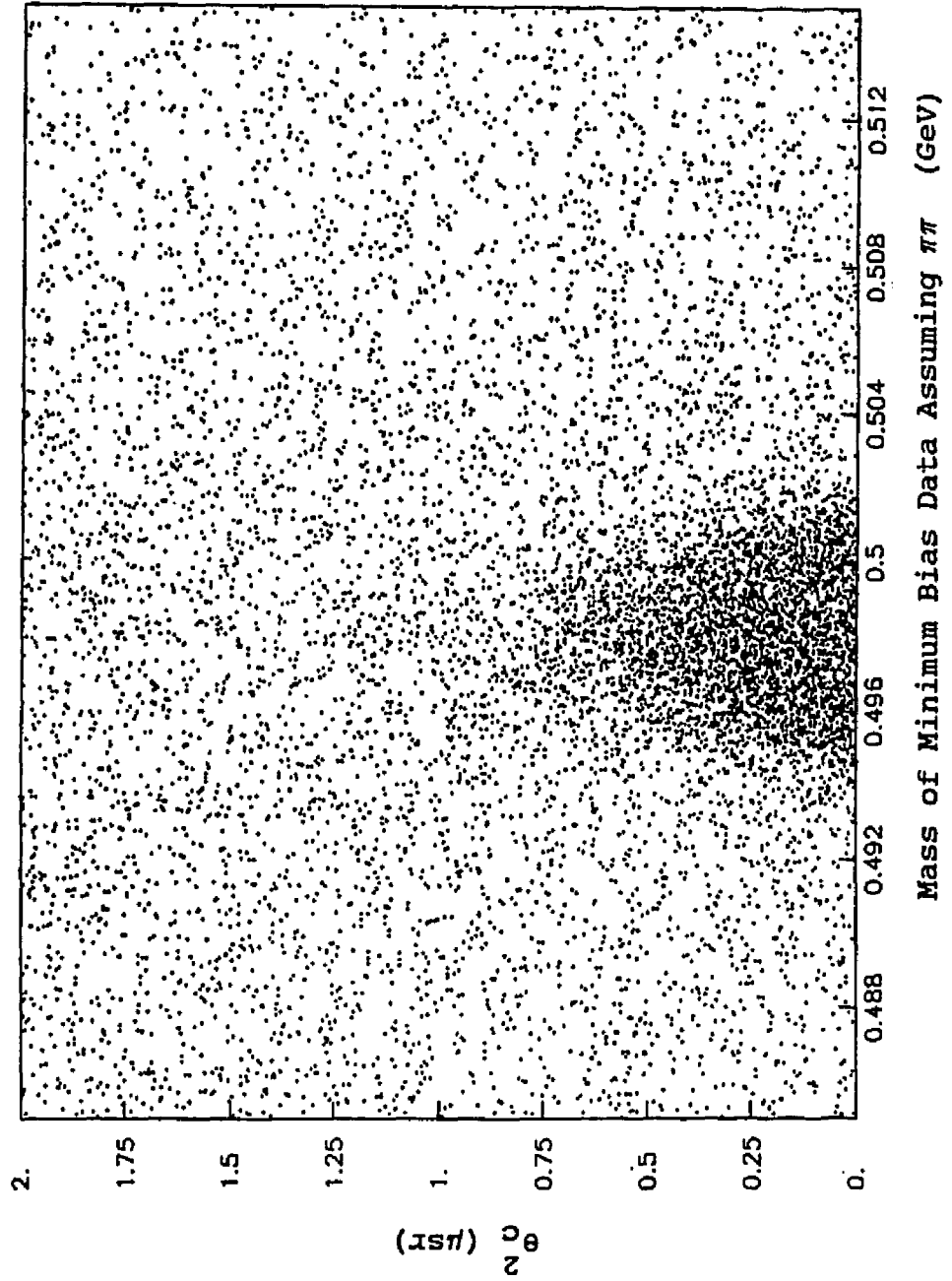


Figure 31

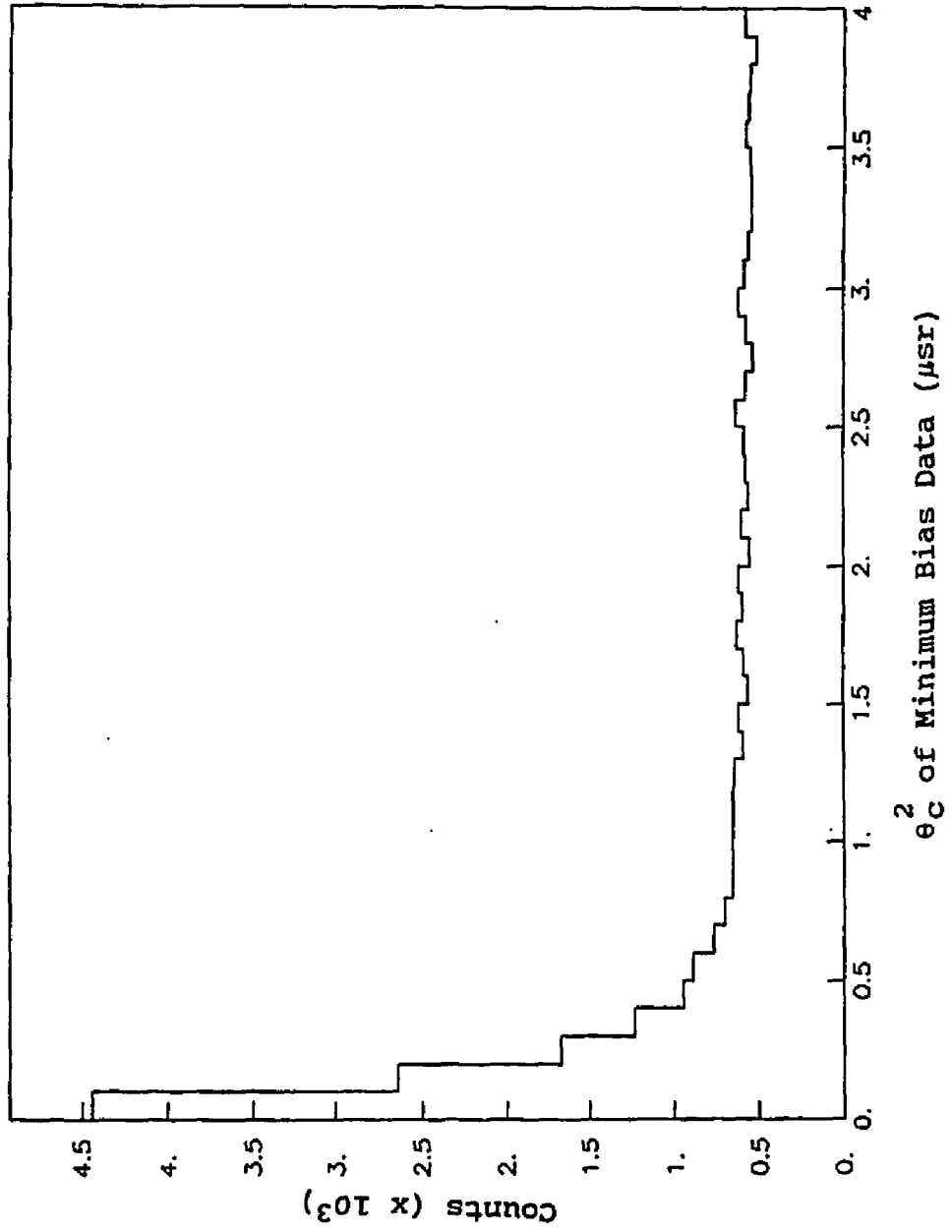


Figure 32

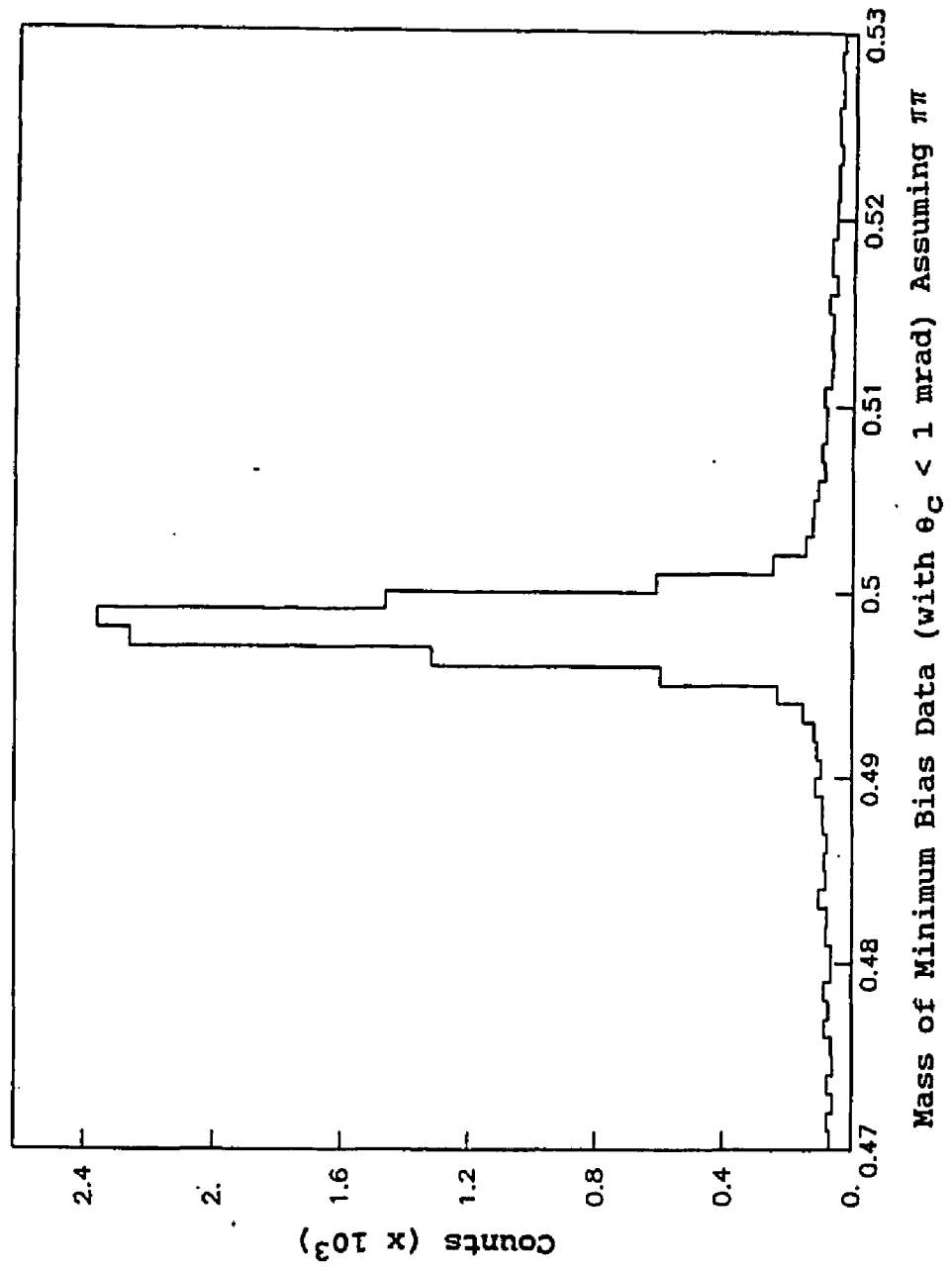


Figure 33

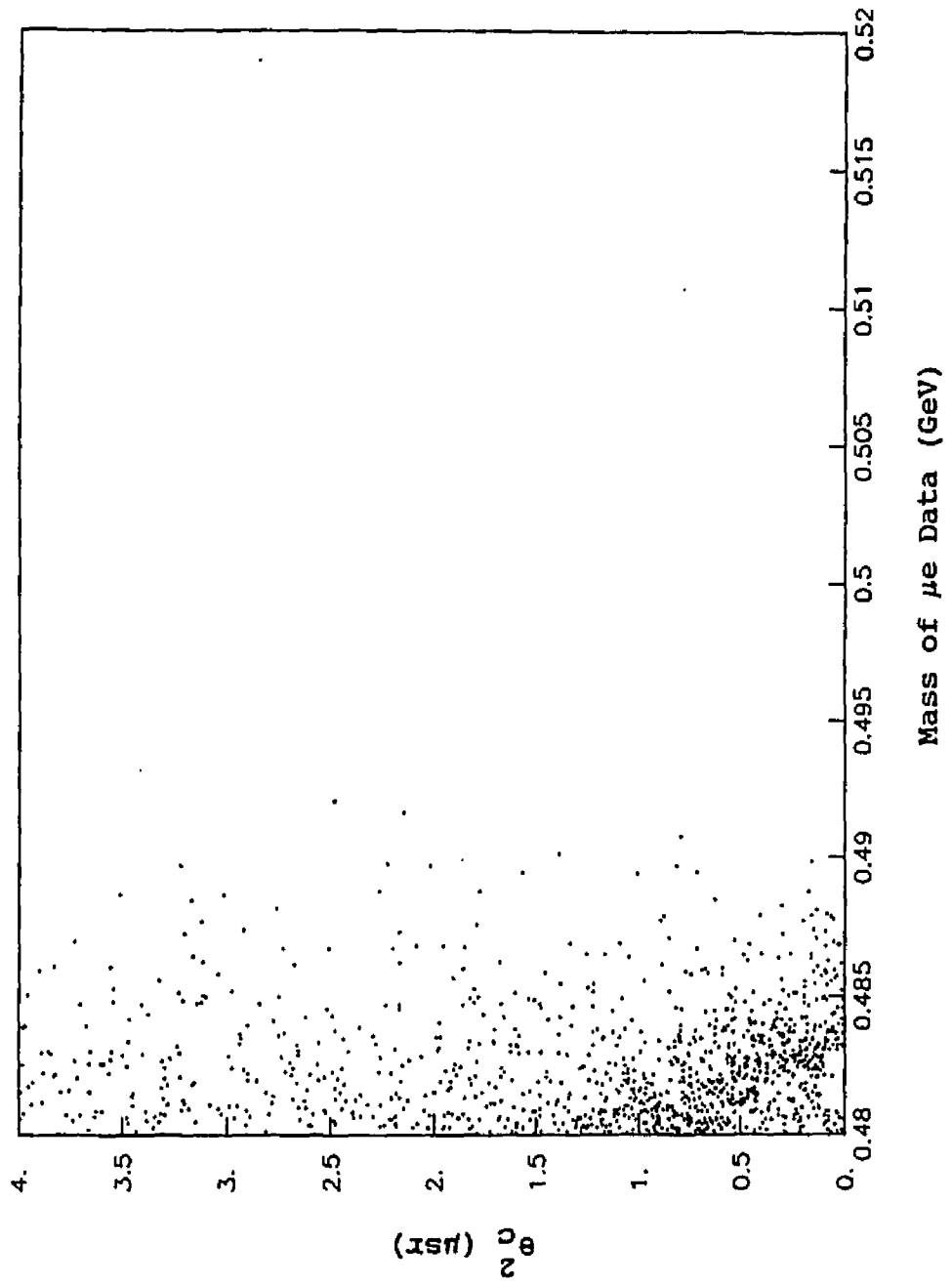


Figure 34

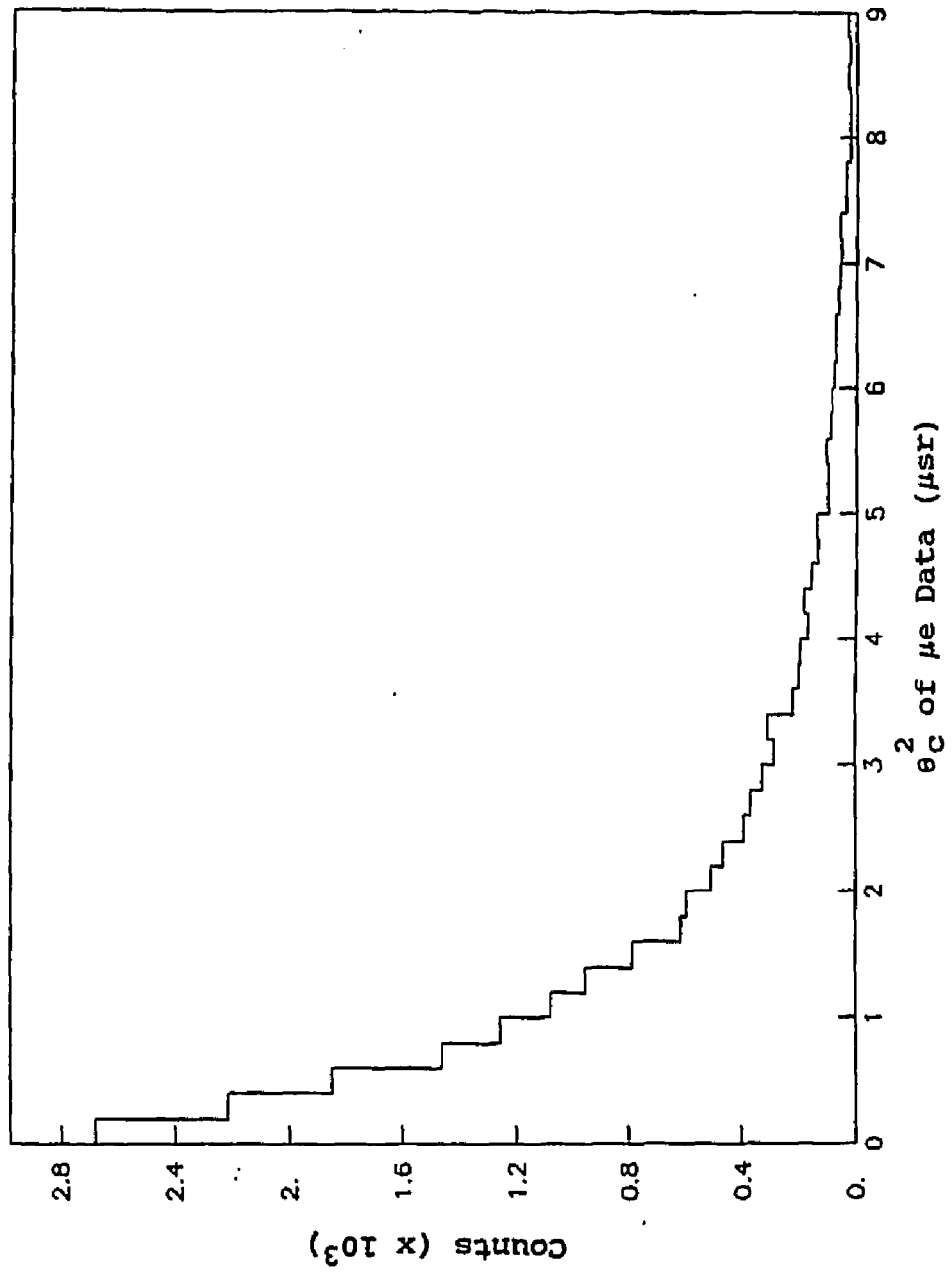
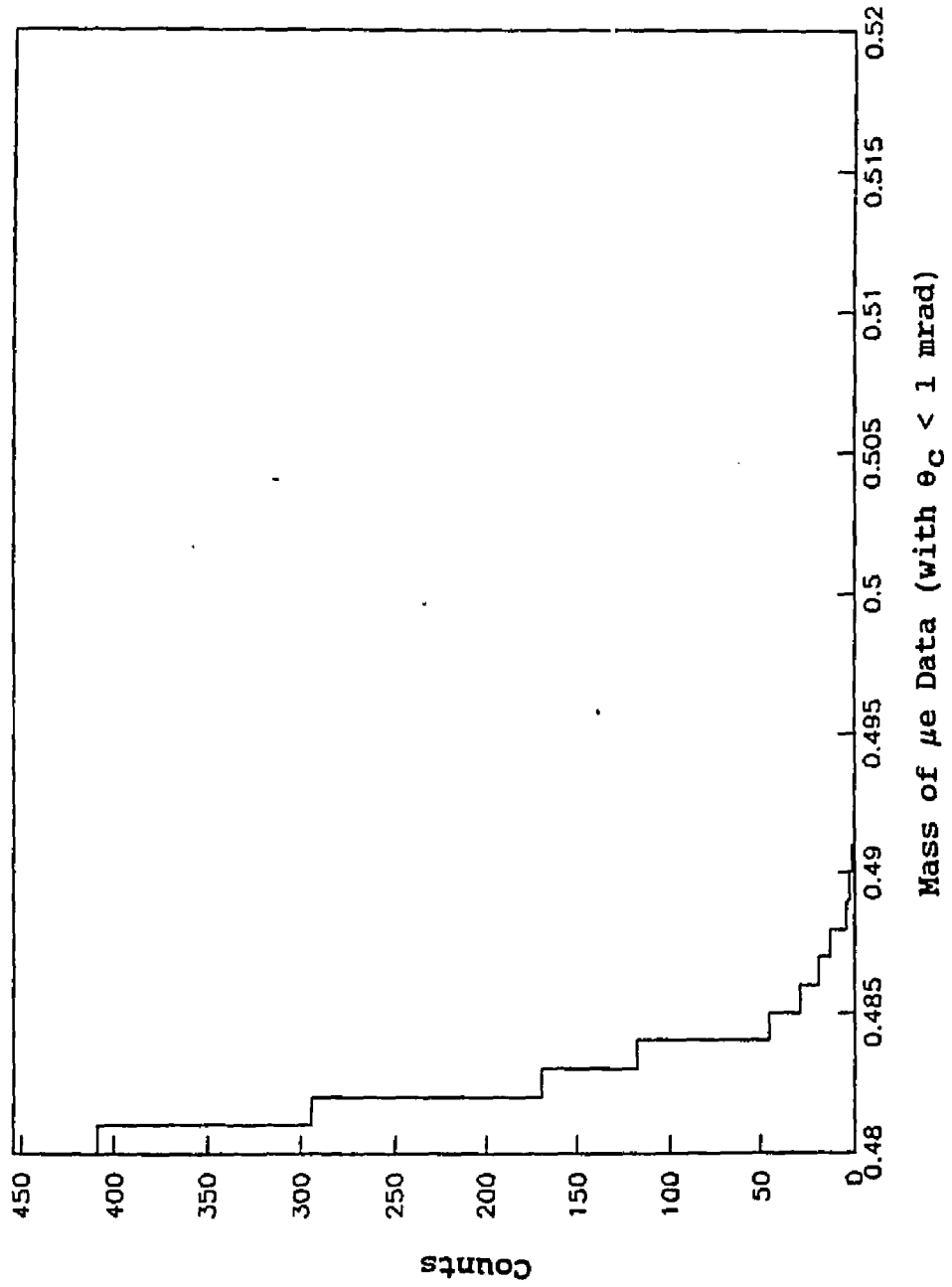


Figure 35



Rangefinder Hit Distribution

Figure 36 Module 3LX

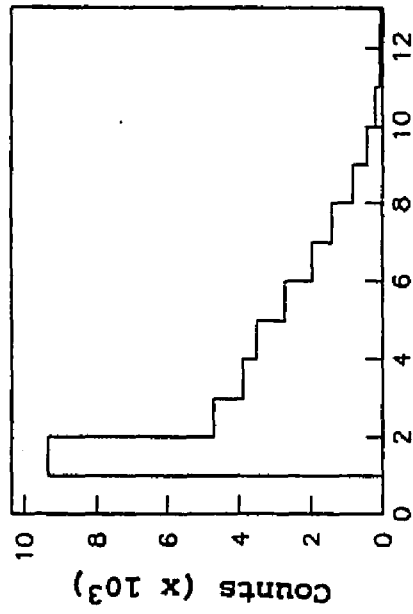


Figure 38 Module 3LY

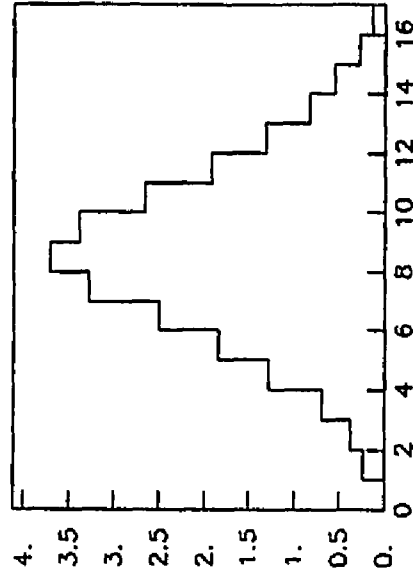


Figure 37 Module 9LX

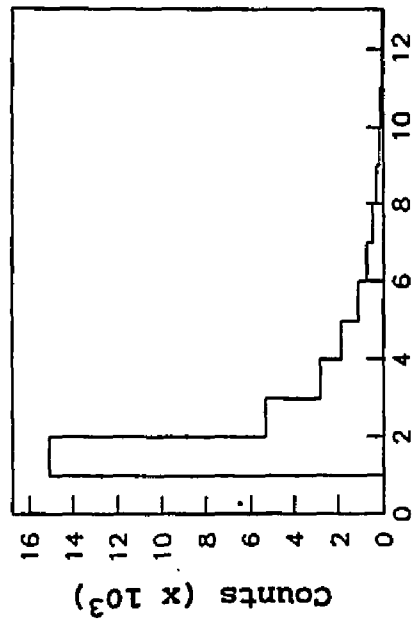
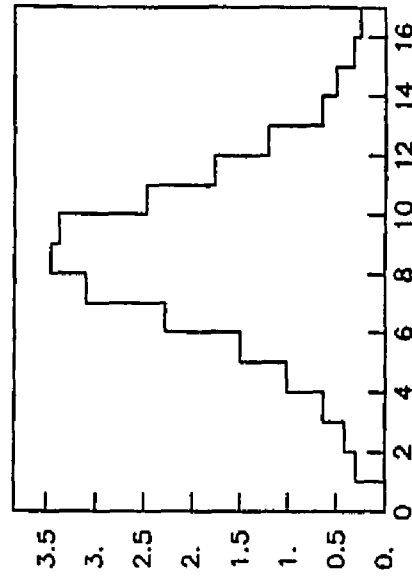


Figure 39 Module 9LY



Projected Hit Position - Actual Hit Position

Figure 40 Module 3LX

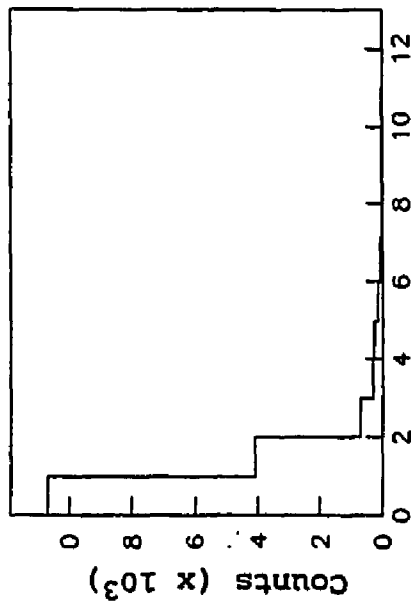


Figure 42 Module 3LY

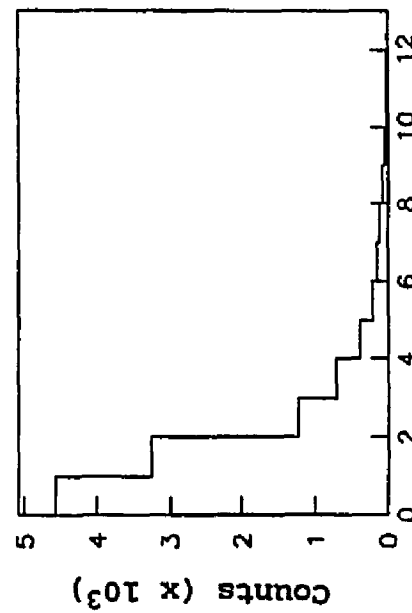
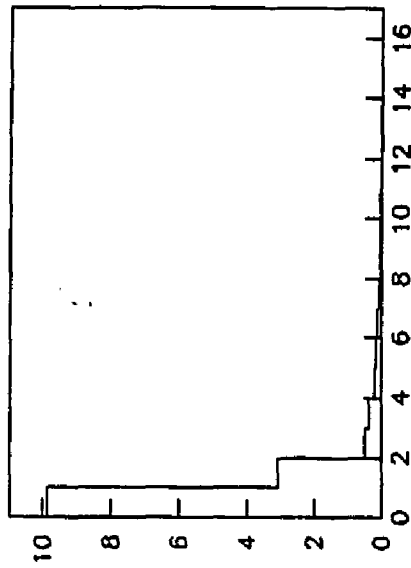


Figure 41 Module 9LX

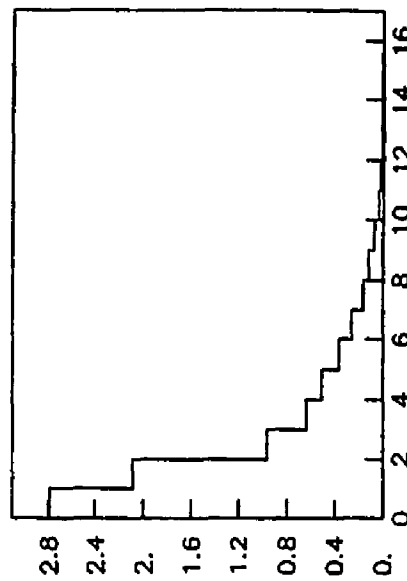


Figure 43 Module 9LY

VITA

John Fred Ginkel

Born in Creston, Iowa, May 6, 1961. Graduated from Valley High School in Des Moines, Iowa in June, 1979, B.S., University of Iowa, 1983, M.S., College of William and Mary, December, 1984, Ph.D., College of William and Mary, August, 1989, with a concentration in Physics.